Chemie der Erde 74 (2014) 3–48

Contents lists available at ScienceDirect

Chemie der Erde

journal homepage: www.elsevier.de/chemer

Invited Review

Silicate-bearing iron meteorites and their implications for the evolution of asteroidal parent bodies

Alex Ruzicka*

Cascadia Meteorite Laboratory, Portland State University, 17 Cramer Hall, 1721 SW Broadway, Portland, OR 97207-0751, United States

ARTICLE INFO

Article history:
Received 17 July 2013
Accepted 15 October 2013
Editorial handling - Prof. Dr. K. Heide

Keywords:
Asteroid differentiation
Iron meteorites
Silicate inclusions
Collisions

ABSTRACT

Silicate-bearing iron meteorites differ from other iron meteorites in containing variable amounts of silicates, ranging from minor to stony-iron proportions (~50%). These irons provide important constraints on the evolution of planetesimals and asteroids, especially with regard to the nature of metal–silicate separation and mixing. I present a review and synthesis of available data, including a compilation and interpretation of host metal trace-element compositions, oxygen-isotope compositions, textures, mineralogy, phase chemistries, and bulk compositions of silicate portions, ages of silicate and metal portions, and thermal histories. Case studies for the petrogeneses of igneous silicate lithologies from different groups are provided. Silicate-bearing irons were formed on multiple parent bodies under different conditions. The IAB/IIICD irons have silicates that are mainly chondritic in composition, but include some igneous lithologies, and were derived from a volatile-rich asteroid that underwent small amounts of silicate partial melting but larger amounts of metallic melting. A large proportion of IIE irons contain fractionated alkali-silica-rich inclusions formed as partial melts of chondrite, although other IIE irons have silicates of chondritic composition. The IIEs were derived from an H-chondrite-like asteroid that experienced more significant melting than the IAB asteroid. The two stony-iron IVAs were derived from an extensively melted and apparently chemically processed L or LL-like asteroid that also produced a metallic core. Ungrouped silicate-bearing irons were derived from seven additional asteroids. Hf–W age data imply that metal–silicate separation occurred within 0–10 Ma of CAI formation for these irons, suggesting internal heating by ^{26}Al. Chronometers were partly re-set at later times, mainly earlier for the IABs and later for the IIEs, including one late (3.60 ± 0.15 Ga) strong impact that affected the "young silicate" IIEs Watson (unfractionated silicate, and probable impact melt), Netschaëvo (unfractionated, and metamorphosed), and Kodaikanal (fractionated). Kodaikanal probably did not undergo differentiation in this late impact, but the similar ages of the "young silicate" IIEs imply that relatively undifferentiated and differentiated materials co-existed on the same asteroid. The thermal histories and petrogeneses of fractionated IIE irons and IVA stony irons are best accommodated by a model of disruption and reassembly of partly molten asteroids.

Contents

* Tel.: +1 503 725 3372.
E-mail address: ruzickaa@pdx.edu

0009-2819/$ – see front matter © 2013 Elsevier GmbH. All rights reserved.
http://dx.doi.org/10.1016/j.chemer.2013.10.001

1. Introduction

Silicate-bearing irons contain more or less silicates, often in the form of inclusions. Their existence is a bit of a conundrum, because most irons are widely accepted to have formed by the crystallization of metallic melt during differentiation in asteroidal parent bodies, a process that would be expected to separate buoyant silicate from dense metal. Iron meteorites come in two varieties, those that show good chemical evidence for fractional crystallization of metal from a large molten reservoir, and those that do not. Both can contain silicates (Table 1), although silicates are more prevalent in the non-fractional variety. The fractional irons are thought to have formed as cores in at least eleven different asteroid parent bodies (e.g., Scott and Wasson, 1975; Wasson, 1985; Haack and McCoy, 2005; Chabot and Haack, 2006; Goldstein et al., 2009). In contrast, the origin of the non-fractional irons is far less certain. Do they represent partial or incomplete differentiation? Did they form by impact processes, which possibly mixed core with mantle or crustal materials? Did they form by localized impact melting in an asteroidal megaregolith? Was a combination of these (or other) processes involved?

The IAB/IIICD and IIE groups are the main silicate-bearing iron meteorite groups. They show relatively little evidence for fractional crystallization of metal, and contain from a couple to tens of percent of silicates, mainly as millimeter to centimeter-sized inclusions (e.g., Scott and Wasson, 1975; Wasson and Wang, 1986; Choi et al., 1995; Wasson and Kallemeyn, 2002; Mittlefehldt et al., 1998; Benedix et al., 2000). Although they have been called "non-magmatic irons" (Wasson, 1985; Wasson and Wang, 1986), this is misleading as the metallic host was at least partly molten (Haack and McCoy, 2005; Chabot and Haack, 2006; Goldstein et al., 2009). In many IABs and some IIEs, silicates have "ultrametamorphosed chondrite" to "igneous" (or achondrite) assemblages. In some IAB, IIE, and ungrouped irons, the silicates are felsic, and apparently differentiated to basaltic or more evolved andesitic to rhyolitic igneous rocks (Prinz et al., 1983b; Armstrong et al., 1990; Ruzicka et al., 1999, 2006; Takeda et al., 2000, 2003a; Ruzicka and Hutson, 2010). It is not clear how such extensive silicate differentiation could have occurred in asteroidal bodies, especially in those that did not also experience extensive metal differentiation.

The IVA group is in some ways even more puzzling. Although IVA meteorites are mostly devoid of silicate and are generally agreed to have formed by fractional crystallization in a core setting (e.g., Ulff-Møller et al., 1995; Scott et al., 1996; Wasson and Richardson, 2001; Wasson et al., 2006), two members – Steinbach and São João Nepomeceno – paradoxically contain so much silicate (roughly 50%) that they are properly termed stony iron meteorites (e.g., Scott et al., 1996; Haack et al., 1996; Ruzicka and Hutson, 2006). They contain a silicate assemblage unlike those in other irons.

Silicate-bearing irons are important because they challenge our understanding of the early evolutionary processes that affected planetesimals and asteroids, and because they may offer unique insights about relationships between different meteorite groups. They may have something to tell us about the nature of core formation processes in asteroids, the processes involved in melting chondritic planetesimals to make metal-dominated or silicate-dominated asteroidal igneous rocks, and the origin of stony iron meteorites. More specifically, there are several important questions that potentially can be answered from the study of silicate-bearing irons. (1) Did they form in a fundamentally different way than other irons, i.e., in some way other than core formation? (2) To what extent and under what conditions were these meteorites heated, and how did silicates and metal avoid separation during melting? (3) What was the nature of the process by which silicate became enclosed in a metal-rich matrix? (4) What petrogenesis was involved in creating evolved (non-chondritic) silicate mineralogies and rock types in some irons? (5) How does one interpret radiometric ages, including young or discrepant ages, and can one devise an evolutionary framework for irons? (6) What implications do they have for the origin and evolution of asteroidal parent bodies

Table 1
Listing and key properties of silicate-bearing irons by group.[a]

Group	Meteorite name	Metal chemical trend	Bulk silicate, low-Ca pyroxene composition	$\Delta^{17}O$ silicate (‰)	Ages silicate (Ma)	Cooling rate
IAB[b]	ALH 77255, Caddo County, Campo del Cielo, Canyon Diablo, EET 83333, EET 84300, EET 87504/5/6, Four Corners, Jenny's Creek, Kendall County, Landes, Leeds, Linwood, Lueders, Mertzon, Mundrabilla, NWA 6369, Ocotillo, Odessa (iron), Persimmon Creek, Pine River, Pitts, San Cristobal, Thiel Mountains, TIL 91725, Toluca/Tacubaya, Udei Station, Woodbine, Youngdegin, Zagora	Non-fractional	Mostly unfractionated, magnesian (Fs_{1-8})	−0.3 to −0.7	4313–4610	~1–450 °C/Ma (<780 °C)
IIICD[b]	Carlton, Dayton, Maltahöhe	Non-fractional	Mostly unfractionated, magnesian (Fs_{7-12})	−0.4 to −0.5	–	~3–480 °C/Ma (<780 °C)
IIE unfractionated	Netschaëvo, Techado, Watson 001	Non-fractional	Unfractionated, ferroan (Fs_{15-17})	+0.4 to +0.6	4489–4600, 3040–3790	~3–100 °C/Ma (<800 °C)
IIE fractionated	Colomera, Elga, Kodaikanal, Miles, NWA 5608, Taramuhara, Weekeroo Station	Non-fractional	Fractionated, ferroan (Fs_{15-26})	+0.4 to +0.7	4270–4554, 3350–3740	≥2.5 °C/h (~850–1000 °C), ~1–400 °C/Ma (<800 °C)
IVA	Bishop Canyon, Gibeon, São João Nepomeceno, Steinbach	Fractional	Fractionated, ferroan (Fs_{14-16})	+1.1 to +1.3	–	>100 °C/h (~1200 °C), ~20–900 °C/Ma (<800 °C)
Ungrouped	Bocaiuva, Enon, Guin, Mbosi, NWA 176, NWA 468, Sombrerete, Tucson	Indeterminate	Both unfractionated and fractionated, variable FeO (Fs_{0-28})	−5.2 to +1.1	4541, 4590	–

[a] Data sources given in the text. Rare silicate has also been reported for the fractional irons Puente del Zacate (IIIAB), Santa Clara (IVB), Sikhote-Alin (IIAB), Coahuila (IIAB), and Hex River Mountains (IIAB).
[b] Meteorites with the most prominent, coarsest silicates. Fine silicates (<2 mm across) are widely distributed in meteorites of these groups.

and planetesimals? This review presents a summary of petrologic data for these meteorites in an attempt to answer these and other questions. For more on fractionally crystallized iron meteorites, see the review papers of Haack and McCoy (2005), Chabot and Haack (2006), and Goldstein et al. (2009).

2. Setting the stage: prevalence, associations, and formation of host metal

Table 1 lists silicate-bearing irons sorted by group and summarizes their key properties. Iron meteorites are grouped primarily by trace-element compositions of their metal and the O-isotopic composition of their silicates. The IAB and the IIICD groups, often associated with one another, constitute the largest group (217 meteorites), 24.8% of all irons (Chabot and Haack, 2006). Silicates are widely present in the IAB and IIICD groups (Wasson and Kallemeyn, 2002), though a relatively small number have coarse (>2 mm) grains or accumulations of silicates. The IIEs are a small group (17 meteorites), 2.5% of all irons, but over half of them contain silicates of different types (unfractionated or fractionated). The IVAs are a relatively large group (59 meteorites), 8.6% of all irons, and uncommonly (only 4 of 59, or ~7%) have silicates. Ungrouped irons (83 meteorites) represent 12.1% of all irons and ~10% (8 of 83) have silicates. Rare silicates are present in the fractionally crystallized IIIAB Puente del Zacate (Olsen et al., 1996b), IVB Santa Clara (Teshima and Larimer, 1983), and IIABs Sikhote-Alin (Buchwald, 1975), Coahuila, and Hex River Mountains (Frondel and Klein, 1965).

2.1. Oxygen isotope compositions

Fig. 1 shows the O-isotopic compositions of silicates in irons compared to some possibly related materials. The data are shown on a $\delta^{18}O$ vs. $\Delta^{17}O$ plot, in which any mass fractionation process (i.e., igneous fractionation) will cause a shift on a horizontal trend, parallel to the terrestrial fractionation (TF) line. Nebular processes involving ^{16}O addition or removal will cause a shift along a trend roughly parallel to the carbonaceous chondrite anhydrous materials (CCAM) line.

The data for silicate bearing irons can be split into two populations: Above the TF line, silicates in IIEs largely overlap the composition for H chondrites (Clayton et al., 1983; Olsen et al., 1994; McDermott et al., 2011), whereas those in IVA irons (Steinbach, São João Nepomeceno – SjN hereafter, Gibeon, Bishop Canyon) largely overlap the fields for L or LL chondrites (Clayton et al., 1983; Wang et al., 2004) (Fig. 1). The ungrouped iron Guin also resembles L/LL chondrites, but has metal more reminiscent of IAB-IIICD irons (Rubin et al., 1986).

The high precision data for the Steinbach and SjN trend primarily along a mass fractionation line (Fig. 1). This suggests formation in a single reservoir similar to LL chondrites, although nearby clusters of tridymite and bronzite crystals in Steinbach and SjN have significant differences in $\delta^{18}O$ that could reflect incomplete equilibration during cooling (Wang et al., 2004). High precision data for the IIEs (not shown in Fig. 1) confirm scatter in $\Delta^{17}O$, implying one or more heterogeneous sources for the IIEs generally similar to H chondrites (McDermott et al., 2011).

The O-isotopic compositions for all other silicate-bearing irons lie below the TF line, broadly in the C chondrite range. The data show considerable scatter and overlap between the silicates in IABs and those in winonaites (Fig. 1). High precision O-isotope data for the winonaites have reduced the spread in $\Delta^{17}O$ for them but strengthen the link to IABs (Greenwood et al., 2012). Winonaites are primitive achondrites with generally chondritic mineralogy similar to that in many IABs, which has led to wide acceptance of a genetic relationship between IABs and winonaites, and suggestions they

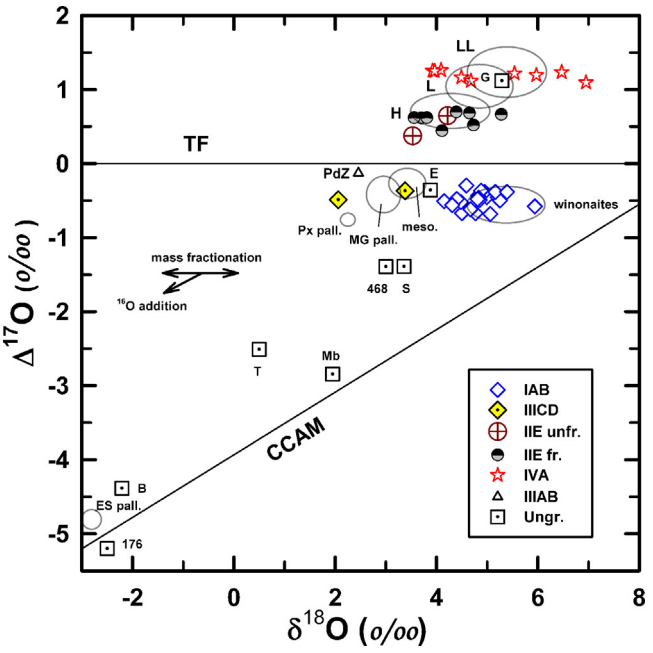

Fig. 1. Oxygen isotope compositions of silicate-bearing irons. $\Delta^{17}O = \delta^{17}O - 0.52\ \delta^{18}O$. Data sources and abbreviations: TF = terrestrial fractionation line, CCAM = carbonaceous chondrite anhydrous materials mixing line, *IABs and IIICDs* – Clayton et al. (1983), Clayton and Mayeda (1996), MBD (2013); *IIE fractionated (IIE fr.)* and *IIE unfractionated (IIE unfr.)* – Clayton et al. (1983), Olsen et al. (1994); *IVAs* – Clayton et al. (1983), Wang et al. (2004); *PdZ (Puente del Zacate)* – Olsen et al. (1996b); ungrouped irons (Ungr.) include *Guin (G)* – Rubin et al. (1986); *Enon (E)* – Clayton et al. (1983); *NWA 468 (468)* – Rubin et al. (2002); *Sombrerete (S)* – Clayton and Mayeda (1996); *Tucson (T)* – Clayton and Mayeda (1996); *Mbosi (Mb)* – Olsen et al. (1996a); *Bocaiuva (B)* – Malvin et al. (1985); *NWA 176 (176)* – Liu et al. (2001). Other meteorites include *H, L and LL chondrite falls and finds* – Clayton et al. (1991); *winonaites* – Clayton and Mayeda (1978); *mesosiderites (meso), main group pallasites (MG pall)* and *Eagle Station pallasites (ES pall)* – Clayton and Mayeda (1978, 1996); *pyroxene pallasites (px pall)* – Boesenberg et al. (2000).

originated in the same asteroid (Bild, 1977; Clayton and Mayeda, 1978, 1996; Clayton et al., 1983; Prinz et al., 1983a; Kallemeyn and Wasson, 1985; Mittlefehldt et al., 1998; Benedix et al., 1998, 2000).

Two analyses for IIICD silicates lie roughly along the same mass fractionation trend to IAB but at lower $\delta^{18}O$ (Fig. 1), together with Main Group pallasites and the ungrouped silicate-bearing iron Enon. However, the latter meteorites probably are not genetically related to IAB/IIICD irons, owing to differences in siderophile element compositions that more closely resemble IIIABs (Kallemeyn and Wasson, 1985; Mittlefehldt et al., 1998).

Most ungrouped irons and Puente del Zacate (IIIAB) have $\Delta^{17}O < 0$ with a large range of $\Delta^{17}O$ values (Fig. 1). This suggests derivation from various parent bodies. Nearly identical in $\Delta^{17}O$ are Sombrerete (Clayton et al., 1983) and NWA 468 (Rubin et al., 2002), which could have been derived from the same body (Franchi, 2008), possibly a CR chondrite-like precursor (Rubin et al., 2002). Tucson and Mbosi are enriched in ^{16}O (Clayton and Mayeda, 1996; Olsen et al., 1996a) and have compositions that indicate derivation from two additional parent bodies (Franchi, 2008). Bocaiuva and NWA 176 have the most ^{16}O-rich compositions (Malvin et al., 1985; Liu et al., 2001), close to the Eagle Station pallasites and the CCAM line (Fig. 1). A relationship to Eagle Station pallasites is also suggested by a high Ge/Ga ratio in Bocaiuva metal (Malvin et al., 1985). Bocaiuva and NWA 176 were probably derived from two additional parent bodies (Franchi, 2008), possibly CO or CV chondrite-like protoliths (Malvin et al., 1985).

2.2. Host metal compositions

IAB metal is relatively rich in volatile elements (high Ga and Ge) but otherwise is generally chondritic (Table 2). IAB irons also have elevated C (~4–5 mg/g), S (~4–97 mg/g), and P (~1.6–3.0 mg/g) (Wasson and Kallemeyn, 2002), suggesting that they could have formed by melting of a volatile-rich chondritic precursor, such as a C chondrite (Choi et al., 1995). Iridium varies by a factor of ~100×, similar to that in fractionally crystallized IVA irons, with a similar coefficient of variation (=100 × s.d./mean where s.d. = standard deviation) in the two groups (~53% and ~59%, respectively). This implies that IABs had some solid metal–liquid metal fractionation (Goldstein et al., 2009), or that precursor materials had variable compositions, or both. There is no compositional hiatus between IABs and IIICDs (Choi et al., 1995; Wasson, 1985; Wasson and Kallemeyn, 2002), but compared to IABs, IIICD metal is more fractionated relative to a chondrite composition and has higher Ni and lower Ir and Ga (Table 2).

Metal in IABs and IIICDs is variable in Ni, Ga, and Ge contents. Coefficients of variation for Ni, Ga, and Ge in these irons are ~25–30%, ~35–78%, and 44–124%, respectively, which are ~2–5×, ~4–9×, and ~7–21× higher than other groups in Table 2. The reason for this is poorly understood (e.g., Kelly and Larimer, 1977), but it probably cannot be attributed to solid–liquid metal separation, given partition coefficients that are not far from unity. Regardless, the variability of these elements is one reason to associate these groups and to distinguish them from other irons.

IAB and IIICD irons may have formed on the same or similar parent bodies (Wasson et al., 1980a,b; Kracher, 1982, 1983, 1985; Choi et al., 1995), but evidence for a single parent body is equivocal (McCoy et al., 1993; Benedix et al., 2000). Although some W isotope evidence suggests earlier formation of IIICDs compared to IABs (Markowski et al., 2006), this is unclear given uncertainties in Hf–W ages, and confusion about which meteorites are IAB and which IIICD. All of the IIICD irons studied by Markowski et al. (2006) are listed as IAB by Wasson and Kallemeyn (2002).

Wasson and Kallemeyn (2002) went further in making associations for the IAB group, combining IABs and IIICDs with many ungrouped irons, into what they termed the "IAB complex" of related materials. However, at least for silicate-bearing members of these ungrouped members, it is clear that not all formed on the same parent body. Sombrerete and NWA 468, two silicate-bearing irons, and Vermillion, a pyroxene pallasite, have distinctly lower $\Delta^{17}O$ than IABs or IIICDs (Fig. 1). This makes it very unlikely they originated on the same parent body. The ungrouped irons Bocaiuva and NWA 176 were tentatively associated with the IAB complex, but they have $\Delta^{17}O$ ~4–4.5‰ lower than IABs, a huge difference that indicates formation on separate asteroids, possibly in a reservoir similar to that which produced CO or CV chondrites (Malvin et al., 1985).

IIE irons show a relatively small range in composition that generally resembles that of H chondrites (Table 2), consistent with their formation by melting of an H-chondrite-like precursor, either the main H chondrite asteroid, or a related body (e.g., Wasson and Wang, 1986). IIE metal has somewhat more Ga than H chondrite metal. This could indicate that the precursor was somewhat different than H chondrites, or that during melting of metal and silicate, Ga was redistributed and preferentially partitioned into metal.

The small range in composition of IIE metal is inconsistent with extensive fractional crystallization (Scott and Wasson, 1975; Wasson and Wang, 1986; Haack and McCoy, 2005). However, As–Ni covariation trends are more similar to fractional IIIABs than to non-fractional IAB/IIICDs (Choi et al., 1995), suggestive of some solid metal–liquid metal fractionation. Ir is slightly enriched

Table 2
Composition of host metal in silicate-bearing iron meteorite groups compared to metal in H and L chondrites.[a]

	Co mg/g	Ni wt%	Ga μg/g	Ge μg/g	As μg/g	Ir μg/g	Au μg/g
IAB[b]	4.84 ± 0.62	8.26 ± 2.86	71.6 ± 25.6	282 ± 129	15.4 ± 4.7	2.20 ± 1.17	1.71 ± 0.38
N = 118	(0.71–6.94)	(5.55–25.2)	(4.8–104)	(5–519)	(10.2–32.2)	(0.01–5.59)	(1.29–3.36)
IIICD[c]	5.74 ± 0.29	15.67 ± 3.97	12.6 ± 9.8	17 ± 21	24.5 ± 4.4	0.20 ± 0.25	1.74 ± 0.12
N = 14	(5.26–6.29)	(11.4–23.4)	(1.5–33.2)	(1–78)	(15.8–32.7)	(0.02–0.85)	(1.54–2.00)
IIE[d]	4.45 ± 0.17	8.38 ± 0.54	24.6 ± 2.6	69 ± 4	11.3 ± 3.4	5.3 ± 1.5	1.25 ± 0.30
N = 12	(4.19–4.76)	(7.51–9.50)	(21.3–29.9)	(64–75)	(5.7–18)	(3.0–7.9)	(0.81– 1.79)
IVA[e]	4.00 ± 0.14	8.50 ± 0.85	2.14 ± 0.20	0.123 ± 0.015	7.53 ± 4.39	1.80 ± 1.06	1.54 ± 0.73
N = 49	(3.77–4.29)	(7.32–11.1)	(1.68–2.52)	(0.092–0.144)	(2.00–14.5)	(0.12–3.78)	(0.61–2.76)
H chondrite[f]	4.56 ± 0.37	8.70 ± 0.57	14.1 ± 1.8	–	11.7 ± 0.8	3.47 ± 0.72	1.16 ± 0.06
N = 24	(3.82–4.95)	(7.22–9.40)	(10.9–18.0)		(10.8–13.7)	(1.60–4.60)	(1.07–1.30)
L chondrite[g]	6.95 ± 1.06	15.1 ± 1.8	13.1 ± 6.6	–	19.1 ± 2.7	4.99 ± 0.40	1.86 ± 0.23
N = 39	(5.29–8.88)	(12.9–18.0)	(2.0–36.9)		(15.6–23.6)	(4.29–5.70)	(1.55–2.20)

[a] Mean ± standard deviation, range in parenthesis, *N* = number of meteorites analyzed.
[b] Wasson and Kallemeyn (2002). Includes IAB main group, subgroup sLL, subgroup sHL, subgroup sHL, subgroup sHH, Udei Station grouplet, Pitts grouplet, Mundrabilla, EET 84300, Kendall County, San Cristobal; excludes Sombrerete.
[c] Wasson and Kallemeyn (2002). Includes subgroup sLM (originally IIIC) and sLH (originally IIID).
[d] Wasson and Wang (1986).
[e] Wasson and Richardson (2001).
[f] Chou et al. (1973), Rambaldi (1977) and Kong et al. (1995).
[g] Chou et al. (1973), Chou and Cohen (1973), Rambaldi (1976) and Kong and Ebihara (1996).

in average IIE metal compared to average H chondrite metal, which could be explained by partial loss of a liquid metal fraction before the formation of IIE metal. Ebihara et al. (1997) found that average metal composition in Miles is within a factor of a few of H chondrites, and that it is most different from H chondrite metal in being depleted in Re, Os, Ir, and Cu. The first three elements are highly compatible in metal, and Cu is a partly chalcophile element that would partition into sulfide. This led Ebihara et al. (1997) to suggest that the Miles source region experienced partial removal of sulfide and solid metal, not a gain of solid metal, from an H-chondrite-like metallic melt. In any case, the data suggest that relatively small amounts of solid metal were fractionated during melting in the formation of IIEs.

The IVAs show extensive and continuous chemical variations consistent with fractional crystallization in a single core of considerable size (Scott et al., 1996; Wasson and Richardson, 2001). They are poor in volatile elements (Ga, Ge and apparently S and P), possibly reflecting a high-temperature formation (Wasson and Richardson, 2001). The IVAs are unusual compared to other fractional irons in having no high-Ir members, the metal that would be expected to crystallize first from a metallic melt (Wasson and Richardson, 2001). The mostly subchondritic Ir content can be explained as a sampling effect: either early-crystallized metal is missing, because first-formed core material was never delivered to Earth, or the liquid metal fraction sank into a core that was sampled, whereas the solid metal residue of IVAs that was left behind in a mantle was not sampled.

Although IVAs have silicates that resemble L or LL chondrites in O-isotope composition (Fig. 1), they do not at first glance have metal that chemically resembles L chondrite metal (Table 2). If the IVAs were derived from L or LL chondrite-like parent bodies, their metal must have been extensively processed, as indicated by the lower siderophile element and higher Fe contents. This can be explained in part by substantial addition of Fe to metal by reduction of FeO in silicates (Wasson and Richardson, 2001). A similar redox process was invoked to account for the composition of silicates in Steinbach and São João Nepomuceno (Ulff-Møller et al., 1995; Wasson et al., 2006; Ruzicka and Hutson, 2006). The low Ga and Ge contents for IVA metal could reflect a volatile-poor precursor (Scott et al., 1996) or conceivably vapor loss at some later stage. Vapor-loss of Ga and Ge during secondary processing was also inferred for the Tucson ungrouped iron (Nehru et al., 1982).

2.3. Setting the stage – summary

Silicate-bearing irons formed on multiple parent bodies. The IAB/IIICD, IIE, and IVA groups each formed on three or more separate asteroids, and at least seven additional asteroids were sampled by the various ungrouped irons. Adding the rare silicates found in IIAB, IIIAB, and IVB irons, at least 13 different asteroids produced silicate-bearing iron meteorites. The IIEs could have formed by the melting of one or more H chondrite-like parent bodies, involving only modest solid metal–liquid metal fractionation, and the IVAs were possibly derived from an L or LL chondrite-like protolith that was extensively heated and partly FeO-reduced before or during core formation. The IABs and IIICDs may have been derived from one or more volatile-rich, heterogeneous bodies, possibly of C chondrite affinity. These potential associations should be evaluated using stable isotope systems such as Cr, Ti, and Ni, which show promise of distinguishing between carbonaceous and non-carbonaceous chondrite source areas (Warren, 2011; Regelous et al., 2008; Trinquier et al., 2007).

3. Mineralogy and textures

3.1. IAB/IIICD irons

Silicates are present in mm- to cm-sized inclusions, and sometimes in a myriad of small (<100 μm) crystals enclosed in metal (Park et al., 1966; Powell, 1969; Fuchs et al., 1967; Bunch et al., 1970; Scott and Bild, 1974; Buchwald, 1975; Wlotzka and Jarosewich, 1977; Bild, 1977; Prinz et al., 1983a; McCoy et al., 1993, 1996; Olsen and Schwade, 1998; Mittlefehldt et al., 1998; Benedix et al., 2000; Takeda et al., 2000; Ruzicka and Hutson, 2010).

Ubiquitous phases in IABs include olivine (forsterite), low-Ca pyroxene (enstatite), high-Ca pyroxene (Cr-diopside), plagioclase (albite), phosphates (mainly Cl-apatite and merrillite), chromite, metal, troilite, schreibersite, and graphite (Bunch et al., 1970; Benedix et al., 2000). Cohenite, alabandite, daubreelite, and rarely sphalerite, are also found (Bunch et al., 1970; Benedix et al., 2000); small patches of K-feldspar are present in Campo del Cielo (Wlotzka and Jarosewich, 1977). The Ni-rich IAB San Cristobal contains K-feldspar with antiperthite exsolution, roedderite, the carbide haxonite, and is unusually rich in the phosphate brianite ($Na_2CaMg(PO_4)_2$) (Scott and Bild, 1974; Prinz et al., 1983a).

Four IIICD meteorites (as identified by Wasson and Kallemeyn, 2002) contain silicates (Maltahöhe, Carlton, Dayton, Persimmon Creek). The first three have mineralogies related to Ni content of the metal (McCoy et al., 1993). Maltahöhe has the lowest Ni and an IAB-like assemblage, and Carlton is intermediate and rich in Cl-apatite and farringtonite–brianite (Kracher and Kurat, 1977; Prinz et al., 1983a; McCoy et al., 1993). Dayton is the most Ni-rich, has no olivine, graphite, or carbides, and contains a silica mineral at the edges of inclusions, and brianite and panethite [$(NaCa)_2(MgFe)_2(PO_4)_2$] (Fuchs et al., 1967; Prinz et al., 1983a; McCoy et al., 1993).

Most silicate inclusions in IABs have granoblastic textures, chondritic mineralogy, and angular to subrounded shapes (Wlotzka and Jarosewich, 1977; Bild, 1977; Prinz et al., 1983a; McCoy et al., 1996; Mittlefehldt et al., 1998; Benedix et al., 2000; Ruzicka and Hutson, 2010) (Fig. 2a–e and g). Grain sizes are typically ~100–300 μm across (Olsen and Schwade, 1998; Ruzicka and Hutson, 2010) (Fig. 2g). Angular inclusions such as those in Landes (Fig. 2a) are obviously clasts. Clasts (inclusions of the Copiapo-type) lack rimming structures (Bunch et al., 1970).

In other cases a clastic origin is much less obvious. Some areas of Campo del Cielo have compact, subrounded inclusions (Fig. 2b), with cores of silicate and rims of intergrown troilite, schreibersite and graphite (so-called inclusions of the Odessa type) (Bunch et al., 1970). They could have formed by a more protracted interaction between metal and silicate. In other samples of Campo del Cielo, silicates and metal are intergrown in a more intimate, dispersed way, although a clastic texture is still discernible (Fig. 2c).

One slab of Campo del Cielo shows an unusual fabric, with alternating bands of silicate-rich and metal-rich areas (Fig. 2d), representing a foliation, with the silicate and metal-rich bands arranged in sheet-like structures. This implies ductile deformation or flow alignment during dynamic metal–silicate mixing. The textures for Campo del Cielo thus imply a combination of brittle deformation to create clasts, "soft" deformation or flow to produce foliation, and sufficient time during or after metal–silicate assembly to allow for reaction and grain growth at interfaces and create a blurring of clast edges.

IABs show evidence for metallic liquids and for metal and sulfide mobility. Irregular metal and sulfide veins sometimes cross-cut silicate-rich clastic areas and merge into the surrounding metal host (Fig. 2a, c, e, i). This implies the movement of metallic fluid through confined areas in the silicates. Troilite is seldom isolated within the host metal but rather is spatially associated with silicates, possibly as a result of differential wetting behavior of metallic melt, between S-rich melt and silicate (enhanced tendency for sulfide to fully coat silicate) and S-poor melt and silicate (less such tendency) (Tomkins et al., 2013a,b). Landes has areas with silicate clasts surrounded by troilite that are themselves enclosed by the metal host (Fig. 1a, arrow). This texture can be explained by separation of S-rich melt from solid or liquid metal, attachment of the S-rich melt to the surface of a silicate clast, and subsequent crystallization of all metal and troilite (Tomkins et al., 2013a,b). A similar process could have resulted in rimmed inclusions.

The properties of the silicates suggest that they were partly melted and that these melts migrated in the IAB body. Although many inclusions are generally chondritic (Wlotzka and Jarosewich, 1977; Bild, 1977), and mineralogically similar to winonaites (Prinz et al., 1983a; Benedix et al., 2000; Takeda et al., 2000), there are mineralogical and textural variations between them (Wlotzka and Jarosewich, 1977). For example "chondritic" inclusions #1, 1A and U1A-1 (Table 3) vary significantly in graphite (~0–22 vol%), plagioclase (~5.4–20%), high-Ca pyroxene (~2.5–6.3%), and to some extent in olivine/(low-Ca pyroxene) ratio. Variation in plagioclase and in high-Ca pyroxene can be attributed to partial melting and melt migration, as such minerals will be preferentially melted and can be locally crystallized elsewhere (Wlotzka and Jarosewich, 1977; Takeda et al., 2000).

No chondrules have ever been reported in IAB/IIICDs, despite the presence of "chondritic" silicates. This suggests that there was sufficient transformation by grain growth during ultrametamorphism or by silicate partial melting to destroy chondrule-like features.

Non-chondritic rock types were found in Caddo County, Ocotillo, and Udei Station, including broadly basaltic, troctolitic, feldspathic orthopyroxenite, and peridotitic mineralogies (Benedix et al., 2000; Takeda et al., 2000; Ruzicka and Hutson, 2010). In Caddo County, gabbroic (or chemically, Mg-andesite) areas grade into adjacent winonaite-like regions (Takeda et al., 2000) and are strongly enriched in plagioclase and diopside (3B in Table 3). In Udei Station and Ocotillo, basalt or gabbro form separate inclusions (Benedix et al., 2000; Ruzicka and Hutson, 2010). A basalt-gabbro inclusion in Udei Station (Udei-1B) is medium-grained (~0.1–1.4 mm diopside and plagioclase), and resembles the Caddo County gabbro in modal composition (compare Udei U1B and Caddo 3B in Table 3). Udei-1B has an irregular shape and appears to have been brecciated, giving the impression of trailing grains behind it (Fig. 2f). This suggests break-up of basaltic rock during metal–silicate mixing.

Unequivocal evidence for melt migration and differentiation is also shown by other inclusions in Udei Station. The most remarkable evidence for differentiation in Udei Station is found in Udei-3B, an inclusion >1.0 cm × >3.8 cm across, which contains three different igneous rock types (feldspathic orthopyroxenite, lherzolite, harzburgite) with apparently *in situ* contacts (Fig. 2i–l). More information about Udei-3B can be found in Appendix-S1.

The presence of chondritic and non-chondritic rock types present in close proximity in Udei Station (Fig. 2e–l) and in Ocotillo can be explained if the inclusions are clasts that formed in different locations of the parent body, which were then juxtaposed by the time of final assembly within host metal (Benedix et al., 2000; Ruzicka and Hutson, 2010).

3.2. IIE irons

Silicates are present in mm- to cm-sized inclusions whose characteristics differ widely between meteorites. It is convenient therefore to group the meteorites into *fractionated* and *unfractionated* types (Table 1), although there are significant differences within these types. This great diversity prompted Mittlefehldt et al. (1998) to divide eight silicate-bearing IIEs into five groups.

The unfractionated Netschaëvo, Techado, and Watson 001 (hereafter Watson) show the effects of progressive thermal processing of a chondritic precursor, with Netschaëvo the least heat-altered, and Watson the most (Olsen et al., 1994; Bogard et al., 2000). All have more-or-less chondritic mineralogies similar to H chondrites, with ~80 vol% olivine and low-Ca pyroxene (bronzite), ~12–19 vol% plagioclase (oligoclase), ~0–5 vol% high-Ca pyroxene (diopside-augite), and lesser chromite, phosphate (Cl-apatite, merrillite), schreibersite, and metal and troilite (Bunch et al., 1970; Olsen and Jarosewich, 1971; Bild and Wasson, 1977; Prinz et al., 1983b; Olsen et al., 1994; Casanova et al., 1995; Bogard et al., 2000). However, silicate textures differ between the meteorites.

In Netschaëvo, inclusions are angular, have granoblastic textures, and contain relict chondrules (Bunch et al., 1970; Olsen and Jarosewich, 1971; Bild and Wasson, 1977; Rubin, 1990). Plagioclase is relatively coarse (up to ~100 μm) (Bild and Wasson, 1977). The angularity of the silicate clasts, and the presence of chondrules (the only iron in which chondrules have been found) suggest brittle deformation with no silicate melting. However, Netschaëvo shows evidence for intense thermal metamorphism, fitting all the criteria of a type 7 chondrite (Mittlefehldt and Lindstrom, 2001). A norm for Netschaëvo (Table 3) resembles H chondrite but has a low olivine/pyroxene ratio, possibly indicating derivation from a parent

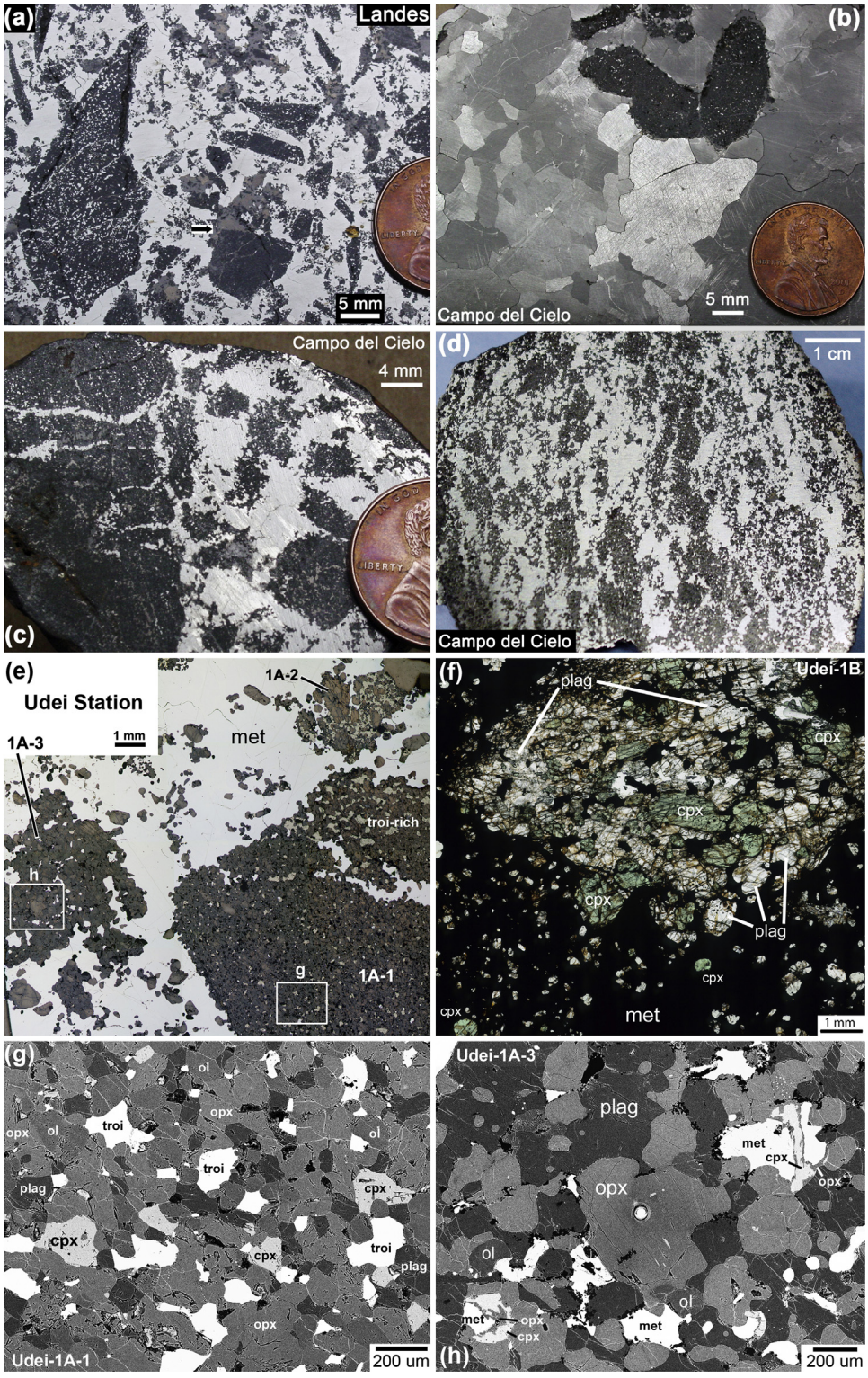

Fig. 2. Images of IABs in polished slab surface (parts a–d) and in thin section (parts e–i). (a) Landes, showing angular clasts. Metal is white, silicate dark gray, troilite tan-bronze. The arrow marks a sharp contact between a silicate clast and surrounding troilite. Marvin Killgore sample. (b) Etched specimen of Campo del Cielo showing metal grain texture (light to dark siliver) which lacks a Widmanstätten pattern, and contains somewhat rounded, rimmed silicate inclusions (dark gray). Marvin Killgore sample. (c) Silicate-rich portion of Campo del Cielo which shows a more dispersed intergrowth between silicate (dark gray) and metal (white), and irregular metal veins crossing silicate. Troilite (tan-bronze) mainly occurs within silicate areas. Marvin Killgore sample. (d) Metal–silicate foliation in Campo del Cielo defined by alternating bands of silicate-rich (gray) and metal-rich (white) bands. Sample CML0077-7. (e) Reflected light mosaic of inclusions 1A-1, 1A-2 and 1A-3 in Udei Station and surrounding fine silicates. Silicate is gray, metal (met) white, troilite (troi) tan-gold. Outlines mark the locations of images in parts g–h. Sample CML0264-1A. (f) Transmitted light image of Udei-1B, which contains plagioclase (plag, white), Cr-diopside (cpx, distinctive green color), and metal and troilite (black). Fine silicates appear to trail to the lower left including diopside, not commonly observed elsewhere in the meteorite. Sample CML0264-1B. (g) Backscattered electron (BSE) image of inclusion 1A-1, showing a granular texture with chondritic mineralogy including orthopyroxene (opx), olivine (ol, slightly darker gray than opx), plagioclase (plag, dark gray), Cr-diopside (cpx, light gray, almost white), and troilite (troi, white) with some metal (white). (h) BSE image of inclusion 1A-3, showing coarser plagioclase (plag) and orthopyroxene (opx), and less olivine and diopside than in nearby 1A-1. Plagioclase poikilitically encloses orthopyroxene and olivine. Thin selvages of orthopyroxene separate metal (met) from clinopyroxene (cpx). The bright

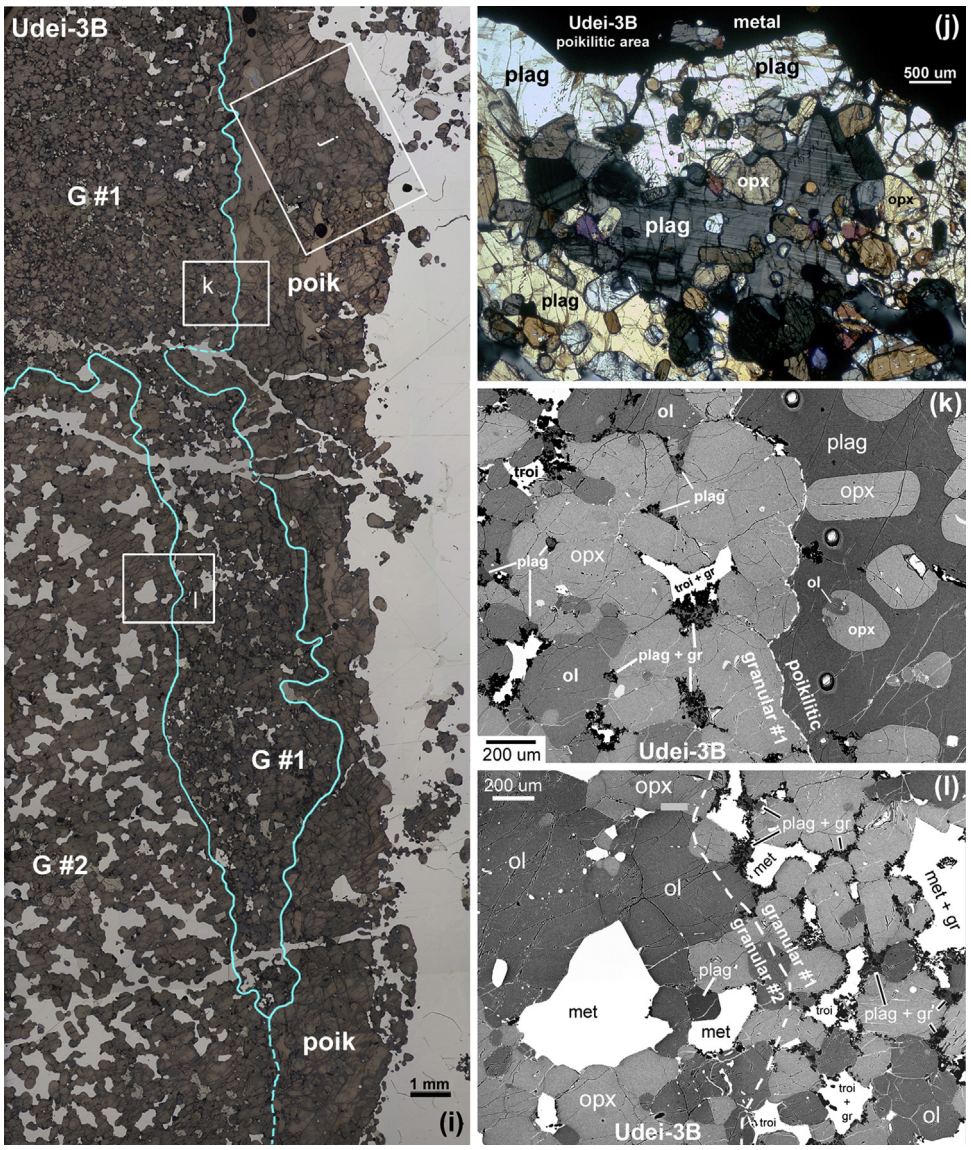

Fig. 2. (*Continued*)

body that was not quite identical to the one that produced H chondrites (Olsen and Jarosewich, 1971; Bild and Wasson, 1977; Rubin, 1990). This is consistent with O-isotopic data (Fig. 1; McDermott et al., 2011) that show this meteorite to be an outlier to the range of compositions measured for H chondrites.

Techado has a single 13 mm long, somewhat rounded silicate inclusion with granoblastic textures (Casanova et al., 1995). Its shape could indicate softening and stretching (Bogard et al., 2000). Grain sizes are olivine up to ~300 μm, low-Ca pyroxene up to ~600 μm, and feldspar up to ~200 μm (Casanova et al., 1995). This coarseness suggests Techado experienced more heating than Netschaëvo, and the inclusion shape and lack of relict chondrules suggests heating close to the point of silicate melting.

Watson contains a huge silicate inclusion (~10 cm long and an exposed area of ~30 cm^2) with a subangular to subrounded shape as well as smaller blebs of silicates at kamacite–kamacite grain boundaries (Olsen et al., 1994). The large inclusion is nearly metal- and sulfide-free, with an igneous texture mainly composed of coarse (~400–1000 μm) orthopyroxene grains that poikilitically enclose olivine (~10–100 μm). Other phases include Ca-pyroxene, clear albitic feldspar with antiperthite exsolution of alkali feldspar, cloudy feldspar, and minor merrillite and chromite. The large inclusion was clearly melted, most likely from a precursor similar to H

spot at the center in orthopyroxene is an LA-ICP-MS analysis spot. (i) Reflected light image of inclusion 3B, showing a poikilitic lithology adjacent to host metal at right, a finely granular lherzolite zone (G#1), and a coarsely granular harzburgitic zone (G#2). Metal veins (white) cross all zones, coarse metal is prevalent in G#2, and troilite and graphite are prevalent in G#1. Boxes mark the locations of insets in parts j–l. Colors as in part e. Sample CML0264-3B. (j) Cross-polarized transmitted light image of the poikilitic zone in 3B, showing twinned plagioclase (plag) grains enclosing orthopyyroxene (opx). (k) BSE image showing the sharp, apparently igneous contact (dashed line) between the poikilitic and G#1 lherzolite zones in 3B. In the granular zone, plagioclase (plag), graphite (gr, black), and troilite (troi, white) occur interstitial to olivine (ol) and orthopyroxene (opx). In the poikilitic zone, orthopyroxene crystals are mainly euhedral. White spots with black edges in plag from the poiklitic zone are LA-ICP-MS analysis locations. (l) BSE image showing the transitional contact (dashed line) between the G#1 (lherzolite) and G#2 (harzburgite) zones in 3B. To the right of the contact within the lherzolite, plagioclase (plag), graphite (gr), and troilite (troi) are interstitial to olivine (ol) and orthopyroxene (opx), whereas to the left in the harzburgite, these phases are almost absent. Note the scalloped texture of the large metal grain at left, which implies liquid metal filling silicate grain interstices.

Table 3
Modes (vol%) of silicate-rich areas in selected iron meteorites, determined by point counting.[a]

Meteorite/area	Rock type	Ol	Low-Ca px	High-Ca px	Plag	Phos	Troi	Metal	Graphite	Other[b]	Ref[m]
IAB irons											
Campo del Cielo/#1	Chondritic	33.0	35.0	2.5	5.4	–	0.1	0.6	22.0	1.7	WJ77
Caddo County/1A	Chondritic	26.0	39.9	5.3	20.0	0.21	4.3	3.7	–	0.03	T00
Udei Station/U1A-1	Chondritic	26.9	40.7	6.3	16.3	0	8.2	1.5	0	0.1	RH10
Caddo County/3B	Gabbro/andesite	8.1	5.4	27.7	58.9	–	–	–	–	–	T00
Udei Station/U1B	Basalt	0	0	33.3	56.4	0	2.6	7.6	0	0	RH10
Udei Station/U3B poik#1	Felds. pyroxenite	0.4	37.4	0.2	59.1	0	1.1	1.2	0.6	0	RH10
Udei Station/U3B gran#1	Lherzolite	33.0	42.3	0.2	2.4	0	11.4	2.6	7.9	0.1	RH10
Udei Station/U3B gran#2	Harzburgite	29.7	44.4	0	0.2	0	1.5	23.7	0.2	0.3	RH10

Meteorite/area	Rock type	Ol	Low-Ca px	High-Ca px	Plag	Phos	Kfeld	Silica	Glass	Other	Ref[m]
IIE irons & ungrouped Sombrerete iron											
Netschaëvo/overall silicate	Chondritic	26.0	52.0	5.4	13.6	1.6	0.0	–	–	1.4[c]	OJ71
Weekeroo St./WS5B	Crys. mafic	0	21.3	18.8	47.5	0.4	0.4	10.9	0	0.7[d]	R99
Weekeroo St./WS7	Glassy mafic	0	6.2	36.0	0	0.2	0.2	0.6	55.1	1.7[e]	R99
Weekeroo St./WS1A	Crys. felsic	0	1.0	1.4	66.1	0.4	0.2	18.2	0	12.7[f]	R99
Miles/M10	Felds. pyroxenite	1.2	33.0	25.7	33.6	2.1	0.1	0	0.3[g]	4.0[h]	RH10
Miles/M1-9 composite	Felds. pyroxenite	0	24.9	36.9	28.8	0.8	1.4	0.4	6.3[g]	0.6[i]	RH10
Miles/M9	Rhyolite	0	0	0	31.0	0	37.2	27.1	4.8[g]	0	RH10
Colomera/6 inclusions	Andesite	0	0	43.9	53.1	1.0	0	0	2.0	0	T03
Sombrerete/overall silicate	Andesite	0	9.4	0	8.3[j]	7.9[j]	0	0	68.5[j]	5.9[k]	R06
Sombrerete/Som1	Bas. andesite	0	14.5	0	11.5	9.5[j]	0	0	64.3[j]	0.3[l]	R06
Sombrerete/Som8	Dacite	0	0.8	0	6.4[j]	1.2[j]	0	0	91.2[j]	0.3[l]	R06

[a] Ol = olivine, low-Ca px = low-Ca pyroxene (mainly orthopyroxene), high-Ca px = high-Ca pyroxene, diopside or augite; phos = phosphate, chiefly Cl-apatite, also merrillite; troi = troilite; Kfeld = K-feldspar; silica = silica mineral, mainly tridymite. Netschaëvo values are a norm.
[b] In IAB irons, "other" includes oxide minerals (primarily chromite), as well as 0.2% schreibersite in U3B gran#2, and 1.7% Fe-oxide produced by terrestrial weathering in Campo del Cielo #1.
[c] Other = 0.9% chromite and 0.5% graphite, latter might be a contaminant.
[d] Other = 0.1% chromite + 0.5% troilite + 0.1% metal.
[e] Other = 0.6% chromite + 0.5% troilite + 0.6% metal.
[f] Other = 0.7% ilmenite + 0.2% chromite + 11.0% troilite + 0.8% metal.
[g] Glass is not glass sensu stricto, but rather a fine-grained K-feldspar + silica intergrowth.
[h] Other = 1.4% chromite + 2.6% metal.
[i] Other = metal.
[j] Plagioclase includes coarser plagioclase and "spongy plagioclase" (a fine-grained intergrowth of plagioclase + Si-rich glass), phosphate includes coarser phosphate and fine-grained phosphate-rich segregations; glass includes both Na- and K-rich types.
[k] Other = 4.3% chromite + 0.3% ilmenite + 0.1% Ti-rich "mixed" phase + 1.2% yagiite.
[l] Other = ilmenite.
[m] References: OJ71 = Olsen & Jarosewich (1971). WJ77 = Wlotzka and Jarosewich (1977). R99 = Ruzicka et al. (1999). T00 = Takeda et al. (2000). T03 = Takeda et al. (2003a). R06 = Ruzicka et al. (2006). RH10 = Ruzicka and Hutson (2010).

chondrites, but aside from metal and sulfide loss did not experience much chemical fractionation (Olsen et al., 1994).

Fractionated IIE irons (Table 1) have globular, igneous-textured inclusions (Prinz et al., 1983b) that compose up to ~10% of the irons (Bogard et al., 2000). They lack or contain only small amounts of olivine (≤2 vol% typically), thus differing sharply from most IABs or unfractionated IIEs (Table 3). Besides having little olivine, fractionated IIEs commonly contain felsic minerals, chiefly albite or oligoclase, and Si-rich glass or tridymite, K-feldspar, and an antiperthite feldspar (Table 3) (Wasserburg et al., 1968; Bence and Burnett, 1969; Bunch et al., 1970; Buchwald, 1975; Osadchii et al., 1981; Prinz et al., 1983b; Ikeda and Prinz, 1996; Ikeda et al., 1997; Ruzicka et al., 1999; Bogard et al., 2000; Takeda et al., 2003a; Kurat et al., 2007; Ruzicka and Hutson, 2010). Colomera contains sanidine, which makes up the chief part of an immense (~11 cm × 2.5 cm × 1 cm across) surface inclusion (Wasserburg et al., 1968; Takeda et al., 2003a). Yagiite, a K–Mg–Al silicate, occurs in Colomera (Bunch et al., 1970), with up to 47% in one inclusion (Prinz et al., 1983b). Pyroxenes of different polytypes are the chief mafic minerals and vary in different meteorites. Subequal orthobronzite and augite occur in Weekeroo Station and Miles, whereas diopside-augite predominates in Colomera, Kodaikanal, and Elga (Table 3) (Prinz et al., 1983b; Bogard et al., 2000). Pigeonite is also present in Weekeroo Station (Ruzicka et al., 1999) and possibly in Elga (Osadchii et al., 1981). Phosphates are mainly Cl-apatite and merrillite, but F-apatite is present in Elga (Osadchii et al., 1981). Tridymite and phosphate are concentrated adjacent to metal grains, implying formation in part by a redox process (Ikeda et al., 1997; Ruzicka et al., 1999; Ruzicka and Hutson, 2010). Accessory minerals include ilmenite, rutile, and armalcolite (Wasserburg et al., 1968; Bunch et al., 1970; Prinz et al., 1983b; Ikeda and Prinz, 1996; Ikeda et al., 1997; Kurat et al., 2007), pentlandite, and sodalite (Ikeda et al., 1997).

The inclusions in fractionated IIEs tend to be uniformly distributed in their metal hosts (Bogard et al., 2000), although some clumping is evident (Fig. 3a and b). This is evidence that on the scale of the meteorites, metal–silicate separation was incomplete. But on the scale of an individual inclusion, separation of metal and troilite from silicate was more extensive, as evidenced by low metal and troilite contents (mainly <1% each) in the inclusions themselves (Table 3). Schreibersite and troilite occur along the edges of the inclusions and metal grain boundaries in the host. In their metal- and sulfide-poor character, the inclusions resemble the large Watson inclusion, and are unlike most inclusions in IAB irons and in the unfractionated IIE irons.

Another difference between the fractionated IIE inclusions and those in other iron meteorites are their globular, as opposed to angular, shapes. This almost certainly results from immiscible separation of metallic and liquid melt (Prinz et al., 1983b; Ikeda and Prinz, 1996). However, the inclusions are somewhat irregular in shape, and take sharp turns in places, conforming around the edges of silicate crystals (Fig. 3b–d) (Ikeda and Prinz, 1996; Ikeda et al., 1997; Bogard et al., 2000; Takeda et al., 2003a; Ruzicka and Hutson, 2010). In detail, metal fills the interstices of pyroxene, whereas

contacts between metal and feldspathic areas tend to be smoother on a bigger scale (Fig. 3c and d). This suggests metal was liquid and filled interstices of pre-existing pyroxene crystals, whereas the boundaries between plagioclase and metal could have been established by liquid immiscibility (Ikeda and Prinz, 1996; Ikeda et al., 1997; Takeda et al., 2003a; Ruzicka and Hutson, 2010). Thus, the silicate could have been a crystal mush (Ikeda et al., 1997; Takeda et al., 2003a). Etched specimens of Miles show that the silicate inclusions are located on metal grain boundaries, and partly jog around them (Fig. 3b). This implies that metal was partially solid at the time silicates were incorporated (Takeda et al., 2003a). If so, both the metallic and silicate portions of fractionated IIEs could

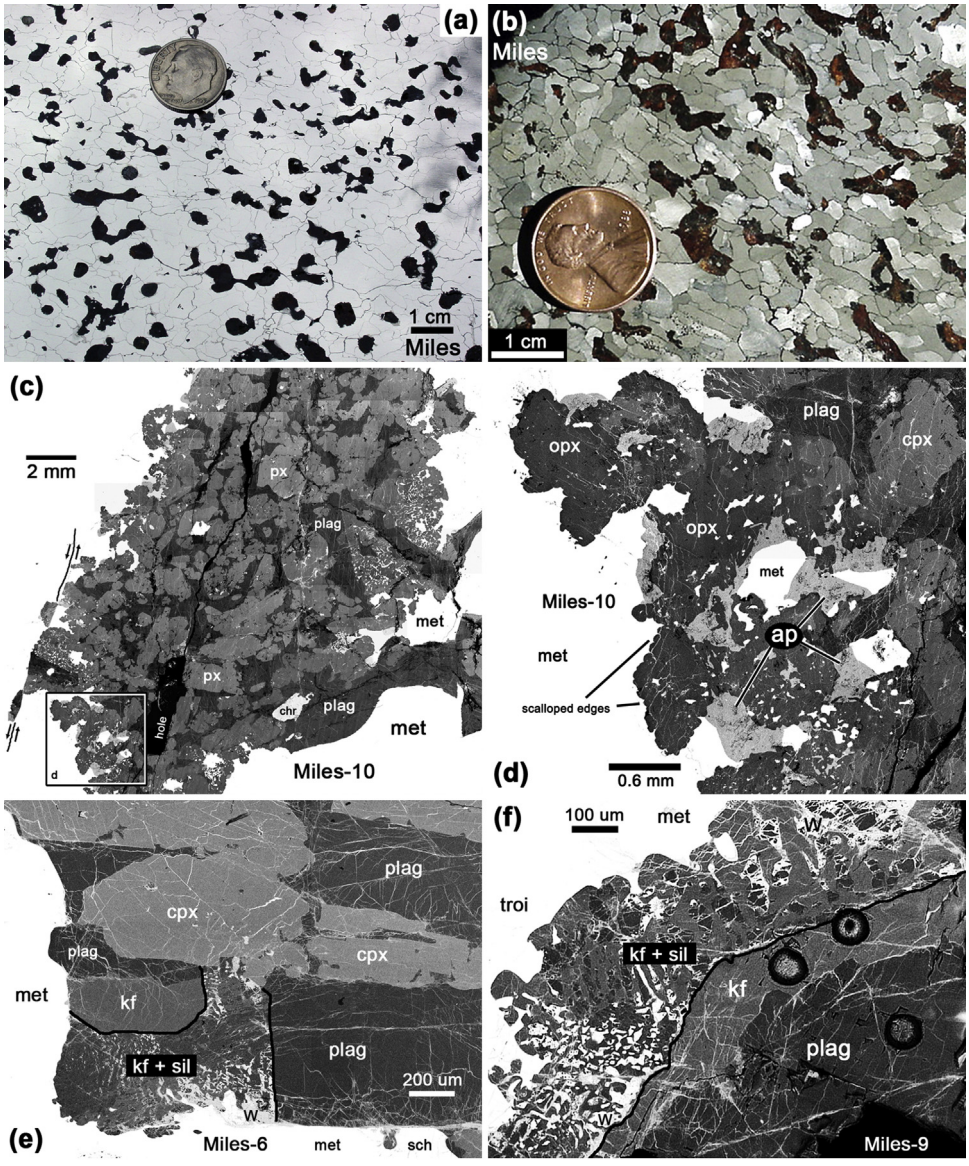

Fig. 3. Images of fractionated IIEs in polished slab surface (parts a–b) and in thin and thick section (parts c–j). (a) Miles showing globular silicate inclusions (nearly black) within metal (white). Marvin Killgore sample. (b) Etched specimen of Miles showing elongate to rounded metal grains (light to dark silver, rarely white) that lack clear Widmanstätten texture, and a non-uniform distribution of silicate inclusions (black to orange) with complex shapes, rounded in places and more angular in others. A faint preferred orientation defined by elongate metal grains and inclusions is visible from upper left to right, possibly indicative of hot-working silicate into preexisting metal with a Widmanstätten texture. Marvin Killgore sample. (c) BSE mosaic of giant inclusion Miles-10, which is composed chiefly of augite and orthopyroxene (px, medium gray) glomerocrysts and interstitial plagioclase (plag, dark gray). Chromite (chr) is also present. Boundaries of the inclusion are more rounded where plagioclase is in contact with metal (met) and more scalloped where pyroxene is in contact with metal. A microfault displaces the inclusion at left. Black areas are cracks and holes. The box shows an enlargement in part d. Sample CML0065-5. (d) BSE image mosaic of the edge of Miles-10 showing apatite (ap, light gray) in contact with metal (met), orthopyroxene (opx) and not clinopyroxene (cpx) or plagioclase (plag) at the inclusion edge, and scalloped edges of the inclusion suggestive of liquid metal infilling spaces between orthopyroxene crystals. (e) BSE image mosaic of a portion of Miles-6, showing coarse augite (cpx), plagioclase (plag), and K-feldspar (kf) grains, and mesostasis composed of an alkali feldspar + silica (kf + sil) intergrowth. Sample CML0065-3. (f) BSE image of Miles-9, which contains coarse plagioclase (plag), K-feldspar (kf), and a fine-intergrowth of alkali feldspar + silica (kf + sil). Weathering product (W, white) surrounds silica (tridymite). Large spots with dark borders are LA-ICP-MS analysis locations. Sample CML0065-3. (g) Cross-polarized transmitted light image of Miles-10 showing orthopyroxene (opx) and augite (cpx), often intergrown, with interstitial plagioclase (plag, dark gray, nearly in extinction). The plagioclase groundmass is all one large crystal. A small patch of striated pyroxene (S.Px) composed of an intergrowth of clinobronzite and orthobronzite, is visible in one location. Sample CML0065-5B. (h) Plane-polarized transmitted light image of WS7 in Weekeroo Station, which consists of tabular and aligned crystals of pyroxene (px), mainly augite, set in glass. Sample AMNH 2620-7. (i) Cross-polarized transmitted light micrograph of inclusion WS5B in Weekeroo Station, a crystalline mafic inclusion composed of tabular and equant pyroxene (px) grains with exsolution lamellae set in holocrystalline groundmass of plagioclase (plag) and tridymite (trid). Note the textural similarity between pyroxene grains in WS7 and WS5B. These inclusions have similar overall "peritectic" compositions. Sample AMNH 2620-5. (j) Cross-polarized transmitted light image of crystalline felsic inclusion WS10B in Weekeroo Station composed of spherulitic plagiocloase and tridymite. Sample AMNH 2620-10.

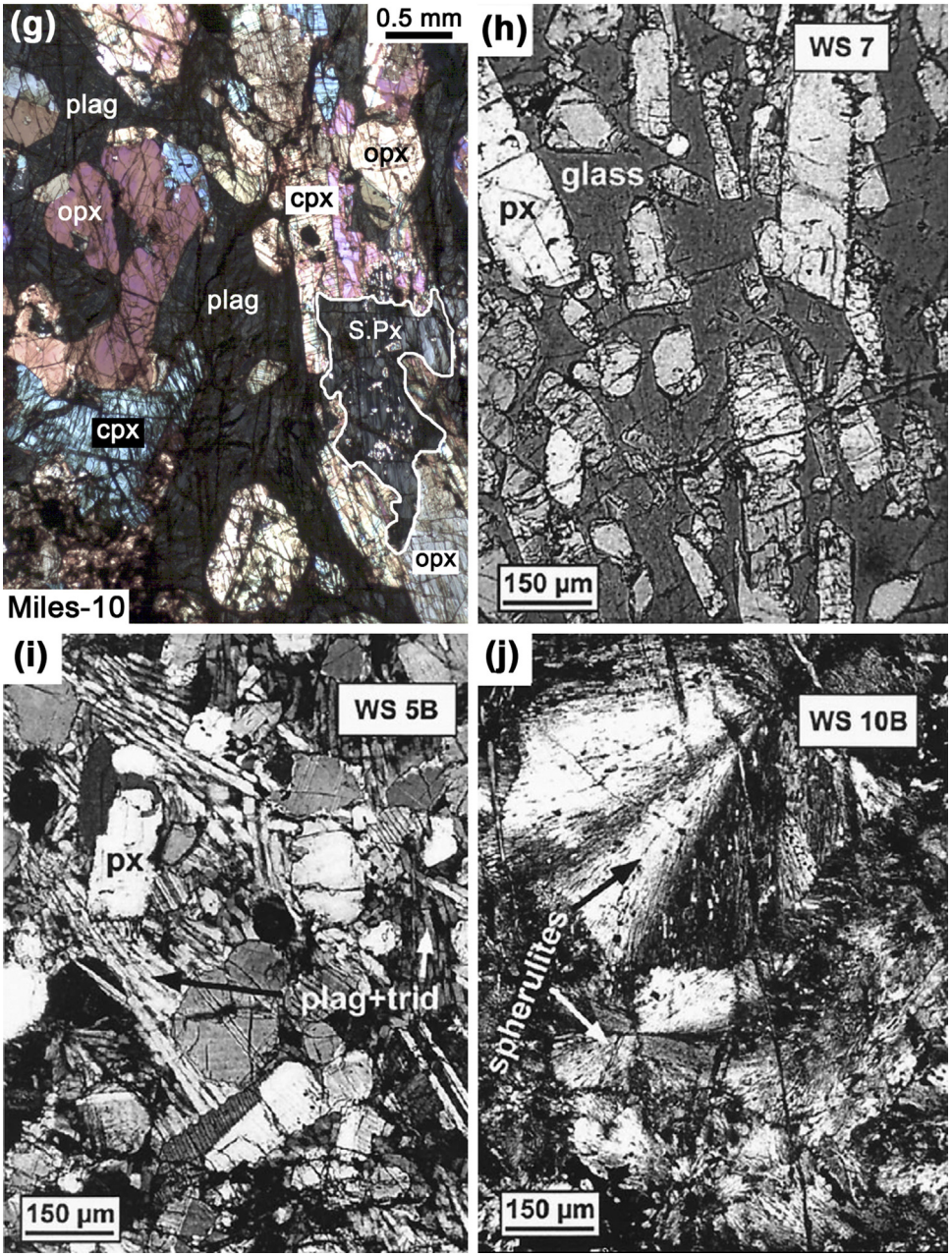

Fig. 3. (*Continued*)

have been partly solid, and partly molten, after metal–silicate mixing.

Silicate inclusions within a given fractionated IIE show large variations in texture and mineralogy (Table 3, Fig. 3c–j) (Prinz et al., 1983b; Ikeda and Prinz, 1996; Ikeda et al., 1997; Ruzicka et al., 1999; Bogard et al., 2000; Takeda et al., 2003a; Hsu, 2003; Ruzicka and Hutson, 2010). This makes it difficult to estimate representative overall modes and compositions for the silicates. Silicates in IIEs include those rich in feldspar and pyroxene (Fig. 3c–e, g and i), feldspar and tridymite (Fig. 3f and j), pyroxene and glass (Fig. 3h), coarse pyroxene, or glass alone. K-rich feldspar is sometimes present, as phenocrysts or in a mesostasis of antiperthite and tridymite (Fig. 3e and f). The mineralogical variations for Colomera (Takeda et al., 2003a) and other fractionated IIEs (Bence and Burnett, 1969; Ikeda and Prinz, 1996; Ikeda et al., 1997; Ruzicka et al., 1999; Ruzicka and Hutson, 2010) suggest mechanical mixing between inclusions rich in pyroxene and feldspar, with metal trapping different proportions of these components. More information about the silicates in Miles and Weekeroo Station can be found in Appendix-S2.

Coarse pyroxene grains in fractionated IIEs show textural evidence of being xenocrysts. Such grains are composed either of augite and orthopyroxene crystals that are much coarser than surrounding feldspathic materials, and which can have a brecciated or corroded appearance (Ruzicka et al., 1999; Bogard et al., 2000), with clinopyroxene sometimes surrounded by an orthopyroxene corona (Bunch et al., 1970; Osadchii et al., 1981; Bogard et al., 2000). This suggests break-up of preexisting pyroxene, sometimes followed by reaction with a secondary melt to produce corona structures (Osadchii et al., 1981; Ruzicka et al., 1999; Bogard et al., 2000). Similar observations and interpretations were made for silicates in the Guin ungrouped iron (Rubin et al., 1986).

3.3. IVA irons

IVA meteorites include two stony irons, Steinbach and São João Nepomeceno (hereafter SjN), and two irons, Gibeon and Bishop Canyon, which contain tridymite (Reid et al., 1974; Ulff-Møller et al., 1995; Scott et al., 1996; Haack et al., 1996; Ruzicka and Hutson, 2006; Wasson et al., 2006). The presence of such low density silicate in high density iron meteorites is striking.

The two stony irons have similar mineralogy and texture and are probably igneous cumulates from which olivine was earlier separated (Ulff-Møller et al., 1995; Ruzicka and Hutson, 2006; Wasson et al., 2006). They are composed chiefly of clumps of coarse-grained low-Ca pyroxene (~0.5–5 mm) and tridymite (~0.35–5 mm), together with coarse-grained (up to ~5 cm × 12 cm) metal with Widmanstätten texture (Fig. 4a and b). Large (>10 cm sized) metal grains can be inferred by uniform Widmanstätten pattern orientations, showing that pyroxene and tridymite often fill spaces within coarser metal grains (Fig. 4a) (Scott et al., 1996). Pyroxene grains are glomerocrystic, composed of separate but attached millimeter-sized grains (Ruzicka and Hutson, 2006). Troilite mostly occurs at edges of metal grains (Wasson et al., 2006), often projecting into silicate areas and not forming isolated grains within metal (Fig. 4a and b), as is often observed in IAB or IIE irons. Metallic areas fill interstices between adjacent pyroxene and tridymite grains forming cusps or scalloped metal–silicate edges (arrows, Fig. 4b) (Scott et al., 1996; Ruzicka and Hutson, 2006; Wasson et al., 2006). This texture implies that silicate grains were surrounded by metallic melt. The presence of swathing kamacite rims on most metal grains implies early crystallization of metal on the silicate (Wasson et al., 2006), involving nucleation of metal from liquid on the silicate, which then grew to encompass the remaining meteorites.

The low-Ca pyroxene in the stony irons consists of different polytypes and textural varieties. Most is orthobronzite and a smaller proportion is clinobronzite (Reid et al., 1974; Ulff-Møller et al., 1995; Scott et al., 1996; Haack et al., 1996; Ruzicka and Hutson, 2006; Wasson et al., 2006). This clinobronzite can be identified by polysynthestic twinning, faint lamellar zoning, and microcracks occurring at a high angle to the lamellar zoning (Fig. 4d). It is typically associated with a cloudy pyroxene composed of small inclusions, chiefly troilite, forming the so-called type 1 pyroxene of Ruzicka and Hutson (2006). Such pyroxene often appears pitted and cracked owing to plucking during sample preparation (Fig. 4b) (Reid et al., 1974; Ruzicka and Hutson, 2006). The cloudy, inclusion-filled pyroxenes probably formed by trapping of melt during crystallization (Ruzicka and Hutson, 2006; Wasson et al., 2006). Both type 1 pyroxene and clinobronzite are enclosed by clear, type 2 orthobronzite (Fig. 4b–d). Sometimes clinobronzite is enclosed by non-lamellar type 1 pyroxene that is itself enclosed in orthobronzite (Fig. 4c and d). Clinobronzite and type 1 pyroxene formed early under probable conditions of rapid cooling that allowed melt trapping and formation of clinobronzite, whereas clear orthobronzite crystallized later under different conditions (Ruzicka and Hutson, 2006).

Steinbach has ~40 vol% low-Ca pyroxene and 20–30% tridymite, with the balance being mostly metal and troilite (Ruzicka and Hutson, 2006, and references therein). The meteorite has a well-determined pyroxene/(pyroxene + tridymite) ratio of ~0.7–0.8. It can be described as a coarse-grained Si-rich orthopyroxenite. SjN has a similar proportion of silicate (Wasson et al., 2006), but a lower proportion of tridymite (Ulff-Møller et al., 1995; Scott et al., 1996; Wasson et al., 2006). SjN too is a Si-rich orthopyroxenite, but not quite as Si-rich.

Tridymite in Gibeon and Bishop Canyon is present mainly as continuous or discontinuous platelets. These are often quite coarse (~22–26 mm × ~1 mm) (Wasson et al., 2006). In Gibeon, these plates can occur within metal grains that have uninterrupted Widmanstätten texture (Wasson et al., 2006), but they also occur at metal grain boundaries, elongated along the straight edges of metal grains that have different Widmanstätten pattern orientations. Given the very different textures of tridymite in the stony irons on the one hand, and in Gibeon and Bishop Canyon on the other, along with differences in minor element composition between the two groups (Ulff-Møller et al., 1995), the tridymite grains in the stony and other irons probably formed by a different process. Wasson et al. (2006) suggested formation of tridymite plates by deposition from Si-rich vapors in contrast to igneous crystallization for tridymite in the stony irons.

3.4. Ungrouped irons

The silicate-bearing ungrouped irons (Table 1) show a rich variety of mineralogies and textures. These range from felsic, fractionated IIE-like inclusions in Guin and Sombrerete, to generally chondritic or IAB-like in Bocaiuva, NWA 176, and Enon, to feldspar depleted in NWA 468, to unique inclusions in Tucson and Mbosi.

The inclusions in Guin (Rubin et al., 1986; Kurat et al., 2007) are very similar to those in IIE fractionated irons. Those in Sombrerete also resemble fractionated IIEs in some ways, but differ in others, notably in high glass and phosphate contents (Table 3). This meteorite contains ~7% silicates in the form of globular inclusions (Prinz et al., 1982). Ruzicka et al. (2006) described a bewildering variety of textures and mineralogies. Among these are inclusions composed of euhedral Cl-apatite phenocrysts set in glass or a combination of glass and other minerals, including yagiite (Fig. 5a and b). Yagiite in Sombrerete links this meteorite to Colomera, a fractionated IIE iron that so far has the only other reported occurrence of the mineral. Fine-grained phosphate-rich segregations have sharp but curving boundaries with the surrounding silicate (Fig. 5d and f) (Ruzicka et al., 2006). Similar segregations were found in Colomera (Bogard et al., 2000, referencing Buchwald, 1975) and in Miles (Ikeda and Prinz, 1996, their Fig. 1-21). These phosphate-rich segregations almost certainly formed by silicate liquid immiscibility, involving separation of P-rich from Si-rich melts (Ruzicka et al., 2006). The sharp boundaries appear to be menisci, and orthopyroxene and ilmenite crystals appear to have sometimes nucleated on them (Fig. 5d) (Ruzicka et al., 2006). Orthopyroxene tends to form elongate euhedral and subhedral crystals often aligned within inclusions, suggestive of flow alignment within the inclusions (Fig. 5c, e, and f). Plagioclase shows evidence for preferential nucleation on grain boundaries, both on metal along the edges of inclusions (Fig. 5e), and on orthopyroxene crystals (Fig. 5f). Plagioclase often forms a fine, spongy intergrowth with glass (Fig. 5c), mostly at inclusion edges. This spongy feldspar probably crystallized rapidly.

NWA 468 contains silicates that are generally similar to those in lodranites (Rubin et al., 2002). A notable feature is the presence of some clinobronzite (Rubin et al., 2002), reminiscent to IVA stony irons and suggesting a link between these two otherwise disparate silicate-bearing irons. The mineral was interpreted as the product of rapid cooling (Rubin et al., 2002), as is suggested for the IVA stony irons (e.g., Haack et al., 1996; Ruzicka and Hutson, 2006), but different than the interpretation of a shearing (shock) origin by Wasson et al. (2006). NWA 468 has an O-isotope composition very similar to that of Sombrerete (Fig. 1), suggestive of pairing (Franchi, 2008). If these meteorites are paired, this would imply that NWA 468 was the fraction poor in feldspathic materials, and Sombrerete the fraction rich in feldspathic materials.

Three ungrouped meteorites, Bocaiuva, NWA 176, and Enon, can be termed stony-irons owing to their high proportion of silicate (roughly 50%) (Malvin et al., 1985; Liu et al., 2001; Bunch et al., 1970; Kracher, 2000). Silicates in Bocaiuva are generally chondritic,

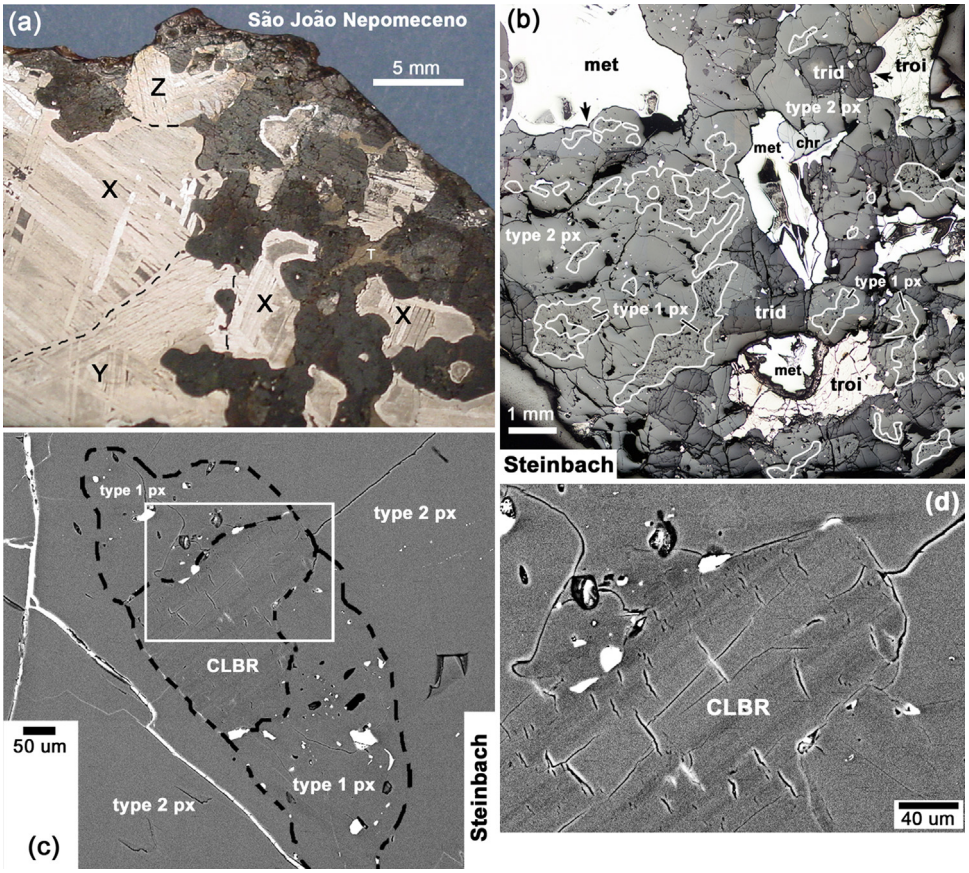

Fig. 4. Images of IVA stony irons in polished slabs. (a) Etched specimen of São João Nepomeceno in reflected light, showing intergrowth between silicate (dark gray) and metal (white). Metal shows Widmanstätten texture and is composed of grains with different lamellae orientations (*X*, *Y*, *Z*), including some separated grains that have the same orientation (*X*), indicating that coarse metal envelopes silicate in a three-dimensional network. Troilite (T, tan-bronze) is located mainly within silicate but typically is in contact with metal. Sample CML0708. (b) Reflected light mosaic of Steinbach, showing metal (met, white), troilite (troi, nearly white, tan color), chromite (chr) and coarse pyroxene (px, medium gray) and tridymite (dark gray). Pxyroxene is composed of more pitted type 1 and less pitted type 2. Metal and troilite fill spaces between tridymite and pyroxene crystals (arrows), suggesting liquid metal enveloped silicate crystals. Sample CML0250-3A. (c) BSE image of Steinbach pyroxene (px) showing a patch of clinobronzite (CLBR) intergrown with pitted and inclusion-filled type 1 pyroxene, both enclosed within type 2 orthobronzite. These textures suggest crystallization of orthobronzite after clinobronzite and type 1 pyroxene. The box shows the area in part d. Sample CML0250-2A. (d) Closeup BSE image of Steinbach, showing clinobronzite with faint lamellar zoning and cracks that trend roughly perpendicular to the lamellae.

except depleted in alkalis, and form "stringers". This implies incorporation of silicates in metal during a shearing process, probably impact-induced (Malvin et al., 1985). NWA 176 has been compared to Bocaiuva owing to similar host metal composition and ^{16}O-enriched bulk composition (Fig. 1) (Liu et al., 2001). It contains ~44% silicate and has an approximately chondritic mineralogy, although plagioclase may be slightly depleted (Liu et al., 2001). Olivine grains in Enon tend to be riddled with micron-sized inclusions of feldspar or feldspathic glass, but plagioclase and orthopyroxene grains tend to be inclusion-free and have euhedral shapes (Kracher, 2000).

The Tucson iron contains ~8% silicates present as small (~0.1–2 mm-diameter) globular inclusions, and the silicate mode (in vol%) is ~66.4 olivine, 30.2 low-Ca pyroxene, 2.7 Ca-pyroxene, and only 0.7 plagioclase (Nehru et al., 1982). Olivine grains range from rounded where in contact with metal to euhedral where in contact with interstitial silicate. The meteorite also contains small amounts of glass, MgAl-spinel, and brezinaite (Cr_3S_4). As with Bocaiuva, silicates in Tucson are arranged in bands and represent a lineation attributed to dynamic flow, caused by an impact process (Miyake and Goldstein, 1974; Nehru et al., 1982).

Mbosi contains sparse, small (1–3 mm across) silicate inclusions, encased in metal with normal Widmanstätten textures (Olsen et al., 1996a). One nearly circular 3.1 mm-diameter inclusion contains a core rich in silica and a fine-grained mantle composed of needle-shaped crystals of pyroxene and plagioclase (Olsen et al., 1996a). Norms imply the presence of plagioclase in the core and Ca-pyroxene and phosphate in the mantle. Two inclusions consist of material similar to the mantle of the larger inclusion, and one contains silica as well. Olsen et al. (1996a) suggested that Mbosi silicate formed by the melting of a unique Si-bearing source rock and injection of this melt into metal.

3.5. IIIAB, IIAB, and IVB irons

Silicates have been found in some IIIAB, IIAB, and IVB fractionally crystallized irons.

Olsen et al. (1996b) described an angular silicate inclusion 7 mm across embedded in a troilite nodule of the Puente del Zacate IIIAB iron. The inclusion has granoblastic textures with grain sizes of ~100–200 μm and an approximate mode (in vol%) of 23 olivine, 14 low-Ca pyroxene, 15 diopside, 15 plagioclase, 1 troilite, 0.5 chromite, 4 metal, and 27 graphite or holes that were probably filled with graphite. It resembles inclusions found in IABs, but has a different, IIIAB-like O-isotope composition. Olsen et al. (1996b) suggested this silicate was derived from the lower mantle of the IIIAB parent body. However, it is unclear why this silicate is not differentiated as one would expect for the mantle of a differentiated body, or how it came to be encased in a metallic core.

Little is known about the silicates in other fractional irons. Santa Clara (IVB) contains silica grains (<25 μm) associated

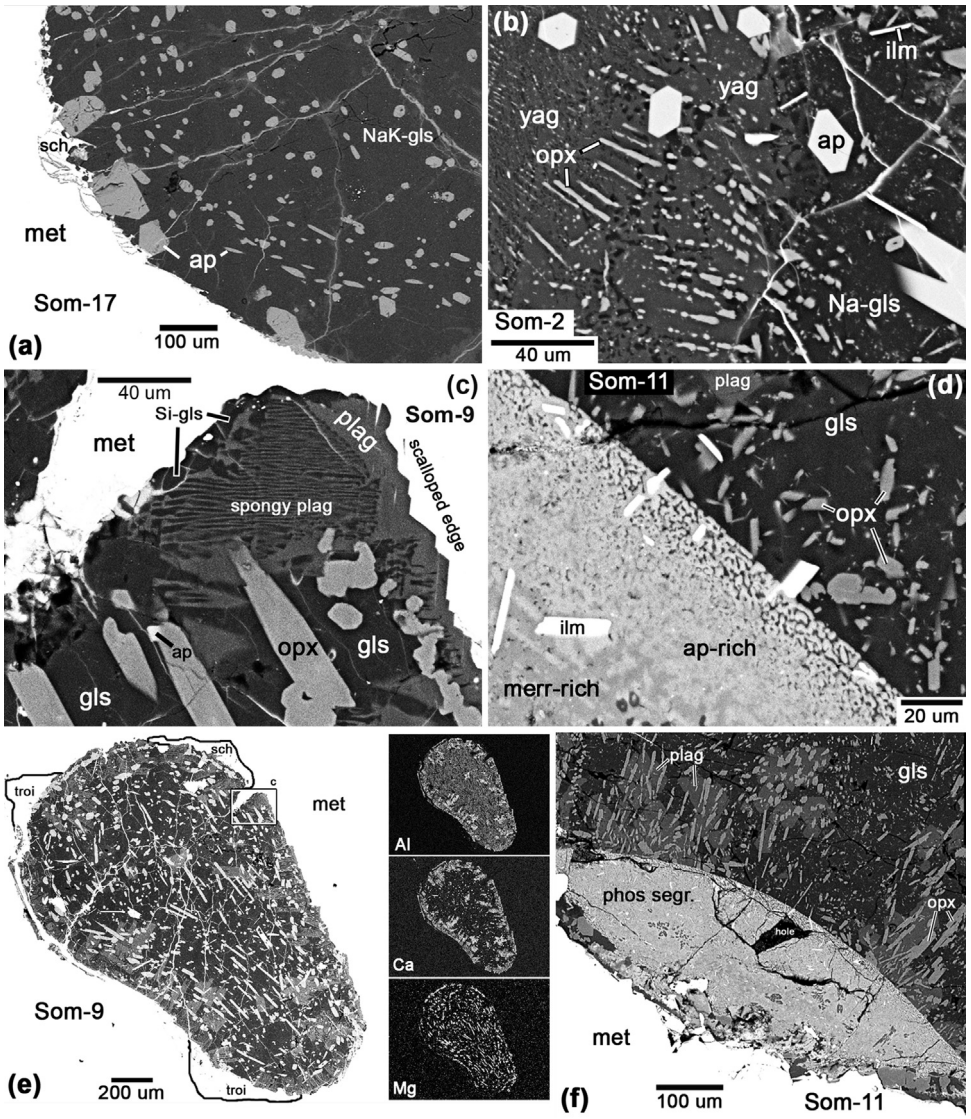

Fig. 5. BSE images of silicate inclusions in Sombrerete (sample AMNH 4493). (a) Som-17 is composed of euhedral phenocrysts of Cl-apatite (ap) set in NaK-glass (NaK-gls). Schreibersite (sch) occurs at the inclusion edge. (b) Som-2 contains euhedral phenocrysts of Cl-apatite and acicular ilmenite (ilm), acicular to equant crystals of orthopyroxene (opx), and large anhedral patches of yagiite, set in a groundmass of Na-glass (Na-gls). (c) Som-9 has elongate to equant phenocrysts of orthopyroxene (opx) and Cl-apatite (ap) set in a groundmass of glasses (gls) of various types. Subhedral grains of plagioclase occur close to the inclusion margins, and in places form a sieved texture ("spongy plag"). Si-glass (Si-gls) occurs adjacent to the inclusion edge. The jagged, scalloped edge of the inclusion is typical for plagioclase-host metal contacts and is suggestive of crystallographic control. (d) Som-11 contains two large phosphate-rich segregations with sharp edges, interpreted to be immiscible separations of P-rich from Si-rich liquids. The edge of one segregation shown here has a marginal zone rich in Cl-apatite (ap) and an interior zone rich in merrillite (merr). Ilmenite (white) occurs as elongate to acicular grains within and outside the segergation; some crystals appear to have nucleated on the segregation boundary. Outside the segregation, elongate to equant orthopyroxene (opx) and subhedral plagioclase (plag) grains are set in glasses of various types (gls). (e) Overview of Som-9 showing the teardrop shape of the inclusion, bordered by troilite (troi) and schreibersite (sch) within the metal (met) host. X ray maps for Al, Ca, and Mg show that plagioclase (high Ca, Al) is concentrated at the inclusion edge, and that orthopyroxene crystals (high Mg) are locally aligned, parallel to the long axis of the inclusion in the center, and circumferential to the edge of the inclusion close to the edge. The box shows the area magnified in part c. (f) Overview of the second phosphate segregation (phos segr.) in Som-11, showing an overall lensoid shape and location close to the edge of the inclusion. Orthopyroxene (opx) crystals are locally aligned perpendicular to the segregation, and plagioclase (plag) surrounds orthopyroxene in places where the pyroxene crystal density is high.

with troilite nodules (Teshima and Larimer, 1983). In the IIABs, minor millimeter-sized olivine has been reported for Sikhote-Alin (Buchwald, 1975), and grains up to 0.5 mm of "ureyite" (kosmochlor) ($NaCrSi_2O_6$) associated with daubreelite and troilite have been found in Coahuila and Hex River Mountains (Frondel and Klein, 1965). Ureyite is also present in the IAB iron Toluca (Frondel and Klein, 1965).

3.6. Mineralogies and textures – summary

The textures of all silicate-bearing irons are generally indicative of the incorporation of solid or liquid silicate in substantially molten metal. Inclusions in IABs irons and the unfractionated IIEs mostly have "chondritic" mineralogies and granoblastic assemblages, which can be explained by high-temperature metamorphism of mostly solid chondritic protoliths, although some also show evidence for silicate melting. The fractionated IIEs contain nearly olivine-free assemblages rich in plagioclase, augite, orthopyroxene, one or more alkali feldspars, phosphates, and glass, and they contain coarser phenocrysts and spherulitic or cryptocrystalline portions. All formed under igneous conditions, probably as crystal – melt mushes, from which olivine was removed. The IVA stony irons contain coarse-grained Si-rich orthopyroxenite assemblages that formed by the incorporation of silicate clusters in a metallic

melt; olivine was removed from their sources. Ungrouped irons extend the range of textures and mineralogies shown by the other groups. In both IABs and IIEs, there are interinclusion variations in mineralogy. Some IABs contain chondritic and non-chondritic igneous assemblages immediately adjacent to one another, probably reflecting impact-mixing of materials with diverse histories from different regions within the IAB parent asteroid. In Tucson, Bocaiuva, and some samples of Campo del Cielo, silicate and metal were mixed together to produce preferred alignments in metal–silicate textures, probably in response to a stress or flow field during metal–silicate mixing. Inclusions in fractionated IIEs are mineralogically and texturally variable, probably the result of variable trapping of silicate crystals and melt during the process of host metal solidification. Some inclusions in fractionated IIEs and in Sombrerete show evidence for silicate flow within their metallic hosts. Coarse crystals of pyroxene in fractionated IIEs and in Guin may be xenocrysts that pre-dated metal–silicate mixing. There is good textural-mineralogical evidence for differential mobility of silicate and metallic melts in the IAB parent body, with silicate melts having been able to migrate more easily than metallic melts, and C–S-rich metallic melts having been able to migrate more readily than C–S-poor metallic melts. Sombrerete shows good evidence in the silicate fraction for immiscible separation of P-rich from Si-rich liquids.

4. Phase compositions

4.1. Major-element phase compositions

Although mineralogies and textures can vary dramatically between inclusions, the same is often not true for major-element mineral compositions (Table 4). Intra-meteorite and intra-grain variations tend to be small. This is especially true for the IABs, which tend to have fairly uniform major-element compositions for olivine, pyroxene, and plagioclase within a given meteorite (Bunch et al., 1970, 1972; Wlotzka and Jarosewich, 1977; Prinz et al., 1983a; McCoy et al., 1996; Olsen and Schwade, 1998; Takeda et al., 2000; Ruzicka and Hutson, 2010). The same can be said for pyroxene and plagioclase in the fractionated IIE irons Colomera, Elga, and Kodaikanal (Bence and Burnett, 1969; Prinz et al., 1983b; Takeda et al., 2003a) and for the IIE unfractionated meteorites Netschaëvo and Watson (Bunch et al., 1970; Olsen et al., 1994). In contrast, Weekeroo Station (IIE fractionated) has an unusually large range in Fs for orthopyroxene ($Fs_{18–41}$) and augite (Fs_{12-22}), although plagioclase compositions vary modestly ($Ab_{78–85}$) (Ruzicka et al., 1999). In Miles (IIE fractionated), the opposite pattern is shown: the composition of plagioclase varies substantially (mainly $Ab_{82–97}$), whereas most pyroxene has a fairly uniform composition (mainly $Fs_{20–23}$ for orthopyroxene and $Fs_{9–12}$ for augite) (Ikeda and Prinz, 1996; Ruzicka and Hutson, 2010).

Figs. 6 and 7 show data for olivine Fa and pyroxene Wo–Fs–En contents. There are two broad groupings, FeO-poor and FeO-rich, based on Fa and Fs compositions. In Fig. 6, there is a bimodal distribution, with IAB, IIICD, and five ungrouped irons and Puente del Zacate having magnesian olivine ($Fa_{0–7}$), and IIE irons having more ferroan olivine ($Fa_{14–29}$). Similarly, in Fig. 7, a distinction can be made between (1) IAB, IIICD and five ungrouped irons and Puente del Zacate with magnesian orthopyroxene ($Fs_{1–12}$ and mostly $Fs_{<8}$), and (2) IIE, IVA and two ungrouped irons with more ferroan orthopyroxene ($Fs_{13–29}$ and mostly $Fs_{>15}$).

The FeO groups generally correspond to different oxygen isotope compositions. The irons with $\Delta^{17}O$ values <0 are less ferroan, whereas IIE irons with $\Delta^{17}O$ values >0 are more ferroan (Table 1; compare Figs. 1, 6 and 7). This likely reflects different chondrite precursors, namely O chondrite-like precursors for the FeO-rich –

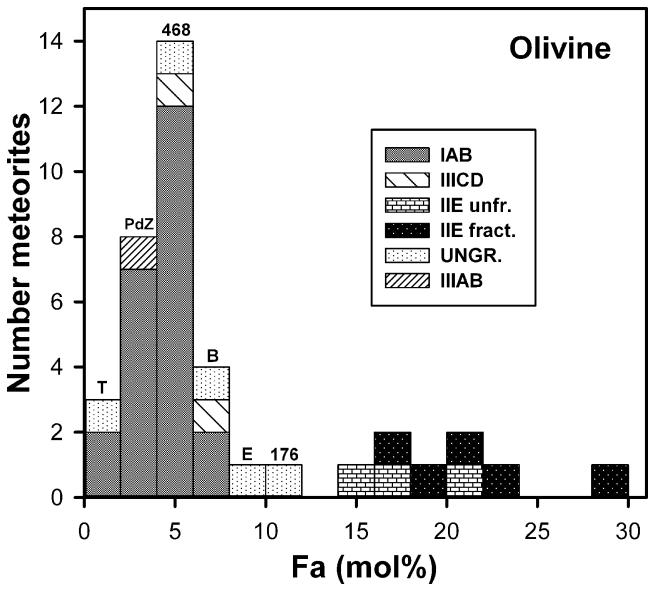

Fig. 6. Histogram of average olivine Fa (atomic 100 · Fe/(Fe + Mg)) in silicate-bearing irons from various groups. Abbreviations as in Fig. 1. Data sources: *IAB irons* – Bunch et al. (1970, 1972), Ramdohr et al. (1975), Bild (1977), Wlotzka and Jarosewich (1977), Luzius-Lange and Palme (1987), McCoy et al. (1996), Olsen and Schwade (1998), Benedix et al. (2000), Takeda et al. (2000), Ruzicka and Hutson (2010), MBD (2013), Ruzicka et al. (2014); *IIICD irons* – McCoy et al. (1993); *IIE unfractionated irons* – Bunch et al. (1970), Olsen and Jarosewich (1970), Olsen et al. (1994), Casanova et al. (1995); *IIE fractionated irons* – Wasserburg et al. (1968), Bunch et al. (1970), Osadchii et al. (1981), Ikeda and Prinz (1996), Ikeda et al. (1997), Takeda et al. (2003a,b), Weisberg et al. (2009), Ruzicka and Hutson (2010); *Puente del Zacate* – Olsen et al. (1996b); *Ungrouped irons* – Bunch et al. (1970), Nehru et al. (1982), Malvin et al. (1985), Desnoyers et al. (1985), Olsen et al. (1992), Kracher (2000), Liu et al. (2001), Rubin et al. (2002).

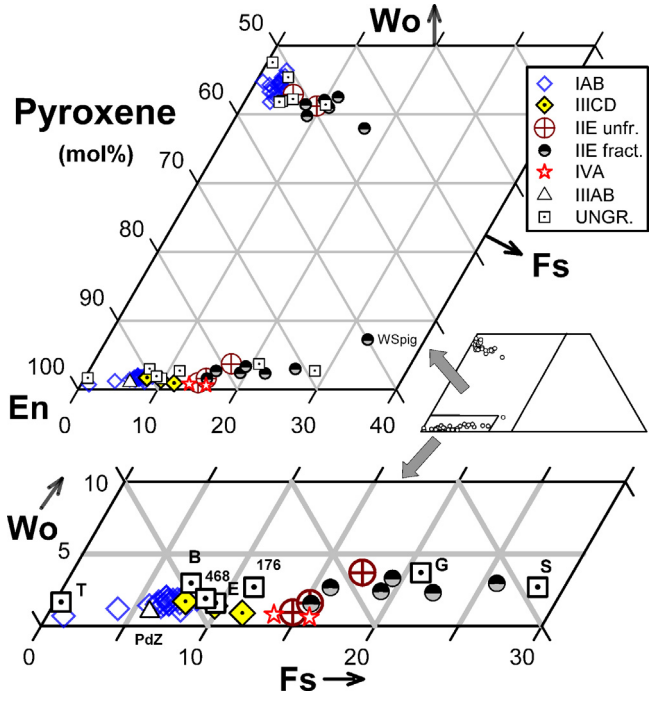

Fig. 7. Average pyroxene Wo, Fs and En [atomic 100 · Ca/(Ca + Fe + Mg), 100 · Fe/(Ca + Fe + Mg) and (100 · Mg/(Ca + Fe + Mg), respectively] in silicate-bearing irons from various groups. Abbreviations as in Fig. 1 and also WS_{pig} = Weekeroo Station pigeonite. Data sources same as in Fig. 6 and also: *IIE fractionated irons* – Bence and Burnett (1969), Ruzicka et al. (1999), Kurat et al. (2007); *IVA stony irons* – Reid et al. (1974), Ulff-Møller et al. (1995), Ruzicka and Hutson (2006); *Ungrouped irons* – Rubin et al. (1986), Ruzicka et al. (2006).

Table 4
Group mean compositions and ranges (mol%) for silicates.[a]

	Ol (Fa)	Opx (Wo)	Opx (Fs)	Opx (En)	Cpx (Wo)	Cpx (Fs)	Cpx (En)	Plag (Ab)	Plag (Or)	Plag (An)	Kfeld (Ab)	Kfeld (Or)	Kfeld (An)	AntiP (Ab)	AntiP (Or)	AntiP (An)
IAB																
Mean	4.1	1.6	6.7	91.7	44.1	3.1	52.8	82.3	3.1	14.7						
s.d.	1.5	0.3	0.9	1.1	1.1	0.5	1.1	3.4	0.6	3.5						
Min	0.8	1.1	4.0	89.8	41.8	1.9	50.6	76.0	1.6	9.2						
Max	7.4	2.0	8.4	94.8	46.4	3.9	55.0	87.1	3.9	21.5						
N	23	18	21	18	18	18	18	14	14	15						
IIICD																
Mean	5.9	1.3	9.7	89.0				93.9	3.0	3.1						
s.d.	1.3	0.4	1.9	1.5				2.8	1.0	1.9						
Min	5.0	0.9	7.8	87.5				91.5	1.9	1.1						
Max	6.8	1.7	11.6	90.5				97	3.6	4.9						
N	2	3	3	3				3	3	3						
IIE unfractionated																
Mean	17.0	2.1	15.8	82.2	42.1	7.5	50.5	78.6	8.0	13.4						
s.d.	3.3	1.4	1.5	2.9	1.2	2.7	1.5	1.5	4.3	3.0						
Min	14.0	1.0	14.6	78.9	41.2	5.6	49.4	77.0	5.1	10.0						
Max	20.6	3.7	17.4	84.5	42.9	9.4	51.5	80.0	13.0	15.4						
N	3	3	3	3	2	2	2	3	3	3						
IIE fractionated																
Mean	21.6	2.5	19.7	77.8	40.9	10.9	48.2	86.7	5.6	7.7	9.5	90.1	0.4	67.7	31.3	1.0
s.d.	5.0	0.6	3.9	4.2	1.6	2.9	2.3	5.1	4.0	5.7	0.1	0.1	0.1	1.3	2.4	1.0
Min	16.0	1.6	15.4	71.2	37.9	7.9	45.0	80.8	2.5	2.9	9.4	90.0	0.4	66.8	29.6	0.3
Max	29.4	3.3	25.8	83.1	42.5	17.0	51.4	93.2	11.4	14.8	9.6	90.2	0.5	68.6	33.0	1.8
N	5	6	6	6	7	7	7	4	4	4	2	2	2	2	2	2
IVA																
Mean		0.7	14.7	84.7												
s.d.		0.1	1.6	1.5												
Min		0.6	13.6	83.6												
Max		0.8	15.8	85.7												
N		2	2	2												

[a] Group means and ranges were determined by first averaging data for individual meteorites, then determining the mean and range for the groups. IAB mean and range excludes Kendall County. IIE unfractionated includes Netschaëvo, Techado, Watson. IIE fractionated includes Colomera, Elga, Kodaikanal, Miles, NWA 5608, Taramuhara, Weekeroo Station. s.d. = standard deviation of the mean, min & max = minimum and maximum value for averaged meteorites, *N* = number of meteorites averaged. Ol = olivine, Opx = orthopyroxene, Cpx = augite-diopside, Plag = plagioclase, Kfeld = K-feldspar, AntiP = antiperthite feldspar.

high $\Delta^{17}O$ irons and different precursors for the FeO-poor – low $\Delta^{17}O$ irons. The only exception is Sombrerete, which has unusually ferroan orthopyroxene (average $Wo_{2.7}$ $Fs_{28.4}$) but $\Delta^{17}O < 0$ (Figs. 1 and 7). The reason for this is not clear, but it may have to do with an unusual history for Sombrerete involving either extremes in partial melting (low degree) or in equilibration (low degree), or both. In any case, Sombrerete is the only low-$\Delta^{17}O$ meteorite that contains alkali glass and abundant phosphate, as is typical for the fractionated IIEs, and the only meteorite besides Colomera (a fractionated IIE) that contains the unusual mineral yagiite. Thus, Sombrerete appears more IIE-like than any of the other low-$\Delta^{17}O$ irons.

Among grouped meteorites, IAB irons are the least ferroan. They have average olivine compositions that range from $Fa_{0.8}$ (EET 84300) to $Fa_{7.4}$ (Udei Station), with a strong peak close to Fa_4 (Fig. 6). Ferrosilite in orthopyroxene is strongly clumped at $Fs_{6–8}$ (Fig. 7). The average olivine and orthopyroxene compositions for the IAB group are $Fa_{4.1\pm1.5}$ and $Fs_{6.7\pm0.9}$, respectively (Table 4) (excluding Kendall County which is an outlier in both average orthopyroxene [$Wo_{0.7}$ $Fs_{1.0}$ $En_{98.3}$] and plagioclase compositions [$Ab_{64.9}$ $Or_{0.9}$ $An_{34.2}$]). IIICD irons are slightly more ferrous but overlap the IAB range (Figs. 6 and 7 and Table 4).

IVA stony irons lack olivine but have pyroxene that are the next most ferroan among grouped irons (Fig. 7). Average low-Ca pyroxene (orthobronzite) ranges from $Wo_{0.8}$ $Fs_{13.6}$ $En_{85.7}$ (São João Nepomeceno) to $Wo_{0.6}$ $Fs_{15.8}$ $En_{83.6}$ (Steinbach), and these meteorites also contain clinobronzite that is slightly more magnesian, $Wo_{0.2}$ $Fs_{13.6}$ $En_{86.1}$ and $Wo_{0.3}$ $Fs_{15.0}$ $En_{84.7}$, respectively.

For IIE irons there is a systematic difference in FeO contents between the unfractionated and fractionated groups. The unfractionated IIEs tend to have slightly less ferroan olivine and pyroxene (Figs. 6 and 7), with average olivine similar to the equilibrated H-group chondrite range ($Fa_{16–20}$; Brearley and Jones, 1998) but extending below (Netschaëvo, Fa_{14}) and above (Watson, Fa_{21}) it, with Techado (Fa_{16}) between. Average Fs in orthopyroxene from Netschaëvo ($Fs_{14.6}$), Techado ($Fs_{15.3}$), and Watson ($Fs_{17.4}$) fall within the equilibrated H chondrite range ($Fs_{14.5–18}$, Brearley and Jones, 1998). For both olivine and pyroxene, iron contents increase in the order of apparent thermal processing (Section 3.2). The reason for this correlation, and for the slightly larger range for Fa in olivine compared to H chondrites, is not clear, but the broadly H-chondrite-like values for the unfractionated IIEs support the idea that they were derived from an H chondrite-like protolith and were not significantly fractionated.

The fractionated IIEs are more ferrous than the IAB group and have more variable pyroxene compositions (Figs. 6 and 7), with average Fa in olivine ranging from $Fa_{16.0}$ (Miles) to $Fa_{29.4}$ (Colomera), and average Fs in orthopyroxene from $Fs_{15.4}$ (Elga) to $Fs_{25.8}$ (Weekeroo Station). This group has overall average compositions of $Fa_{21.6\pm5.0}$ for olivine and $Fs_{19.7\pm3.9}$ for orthopyroxene (Table 4). This overlaps the range for equilibrated H group chondrites but is slightly elevated.

More ferroan compositions for fractionated IIEs are consistent with what one would expect, if the silicates in these irons were produced by partial melting of an H chondrite-like protolith. However, except possibly for Colomera ($Fa_{29–30}$), the average Fa values are not much higher than in H chondrites (Fa_{16} in Miles, Fa_{19} in NWA 5608, Fa_{21} in Kodaikanal, Fa_{22} in Elga), so one must invoke processes other than partial melting, such as redox processes, to explain Fa contents that are lower than expected.

There is evidence that redox processes did in fact occur in various irons, widely in IABs and in at least some IIEs. Evidence for this in the IABs includes slightly FeO-poor rims on olivine and/or pyroxene (Wlotzka and Jarosewich, 1977; McCoy et al., 1996)

and apparent Fe-Mg disequilibrium between olivine and orthopyroxene, with olivine being more magnesian than expected for equilibrium with pyroxene (Prinz et al., 1983a; Kallemeyn and Wasson, 1985; Seckendorff et al., 1992). For example, in IAB and IIICD irons, average Fa values for olivine (4.1 and 5.9, respectively) are lower than average Fs values in orthopyroxene (6.7 and 9.7, respectively) (Table 4), but this should be reversed for equilibrium. Possible reducing agents in IAB meteorites include C from graphite or cohenite (Kallemeyn and Wasson, 1985; McCoy et al., 1996) or P-bearing metal (Fuchs et al., 1967), or some combination of P, C, and S (Seckendorff et al., 1992). Seckendorff et al. (1992) estimated that reduction in IAB irons occurred mainly between 1000 and 600 °C, based on consideration of olivine–pyroxene Fe–Mg distributions, pyroxene geothermometry, and Ca zoning in olivine. Progressive FeO reduction of IIICD-like material to form IABs was proposed by Prinz et al. (1983a).

Fractionated IIEs were also affected by FeO reduction. Evidence includes the presence of low-Fs, low-Fe/Mn orthopyroxene rims on grain cores (Ikeda and Prinz, 1996), similar low-Fe orthopyroxene near inclusion edges in Weekeroo Station and Miles (Ruzicka et al., 1999; Ruzicka and Hutson, 2010), and low Fe/Mn values for minerals in Miles compared to those in H chondrites (Ikeda and Prinz, 1996). Unlike most IIEs which have fairly small ranges in orthopyroxene Fs (Prinz et al., 1983b), Weekeroo Station orthopyroxene has an unusually large Fs range (18–41), which was attributed to a combination of fractional crystallization and FeO reduction (Ruzicka et al., 1999). In Miles, FeO reduction could have been responsible for lowering Fs in orthopyroxene from a typical $Fs_{20–23}$ value to Fs_{13} close to inclusion edges (Ruzicka and Hutson, 2010). The inferred driver for this reduction was reaction of a Ca-silicate component (probably mainly in silicate melt) with a P-metal component (probably in metallic melt) (Ikeda and Prinz, 1996; Ikeda et al., 1997; Ruzicka et al., 1999; Ruzicka and Hutson, 2010). Most researchers have identified the Ca-silicate component as Ca-pyroxene. The redox reaction would have oxidized P in metal and removed Ca-pyroxene to form phosphate, orthopyroxene, and silica. For Miles, the proposed reaction can explain the presence of orthopyroxene overgrowths on clinopyroxene, and the common presence of tridymite, phosphate, and orthopyroxene near metal (Fig. 3d) (Ruzicka and Hutson, 2010). A similar, albeit incipient, P-driven reaction was proposed for IAB iron Udei Station, to account for the presence of orthopyroxene selvages between clinopyroxene and metal (Fig. 2h) (Ruzicka and Hutson, 2010).

Feldspar compositions for iron meteorites range widely (Fig. 8 and Table 4). This includes nearly pure anorthite ($Ab_{0.1}$ $Or_{0.1}$ $An_{99.8}$) in Tucson (ungr.), to nearly pure albite ($Ab_{97.0}$ $Or_{1.9}$ $An_{1.1}$) in Dayton (IIICD) (Fig. 8). NaK-feldspars are present in fractionated IIEs, including K-feldspar in Colomera and Miles ($Ab_{9.5}$ $Or_{90.1}$ $An_{0.4}$), and an antiperthite feldspar in Elga ($Ab_{66.7}$ $Or_{33.0}$ $An_{0.3}$) and Miles ($Ab_{68.6}$ $Or_{29.6}$ $An_{1.8}$) (Fig. 8). Miles contains three alkali feldspars – albitic feldspar, K-feldspar and antiperthite, whereas Colomera contains two – K-feldspar and albite.

Despite the overall variety in feldspar compositions, many irons contain plagioclase that generally resembles the oligoclase composition of equilibrated ordinary chondrites (typically $Ab_{80–88}$ $Or_{2–7}$ $An_{10–14}$, Brearley and Jones, 1998) (Fig. 8). This includes (1) most IAB irons (average $Ab_{82.3±3.4}$ $Or_{3.1±0.6}$ $An_{14.7±3.5}$) excluding the anomalous Kendall County; (2) the unfractionated IIE irons Netschaëvo ($Ab_{80.0}$ $Or_{6.0}$ $An_{15.4}$) and Techado ($Ab_{78.8}$ $Or_{6.0}$ $An_{15.4}$); (3) the fractionated IIE irons Miles ($Ab_{87.5}$ $Or_{2.5}$ $An_{9.9}$) and Weekeroo Station ($Ab_{80.8}$ $Or_{4.4}$ $An_{14.8}$); (4) various ungrouped irons, including Guin ($Ab_{86.3}$ $Or_{3.1}$ $An_{10.6}$), Enon ($Ab_{78.9}$ $Or_{6.4}$ $An_{14.7}$), and NWA 468 ($Ab_{78.7}$ $Or_{2.6}$ $An_{8.7}$); and (5) IIIAB Puente del Zacate (Ab_{82} Or_4 An_{14}) (all average compositions) (Fig. 8).

That so many irons have chondritic feldspar compositions suggests that most could have been derived from chondritic

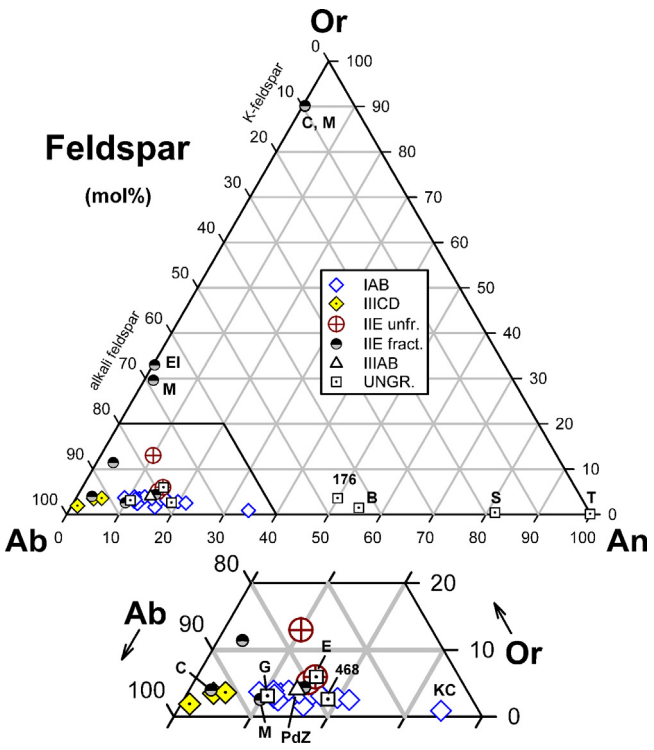

Fig. 8. Average feldspar Ab, Or and An contents [atomic 100 · Na/(Na + K + Ca), 100 · K/(Na + K + Ca) and (100 · Ca/(Na + K + Ca), respectively] in silicate-bearing irons from various groups. Abbreviations as in Fig. 1, and also KC = Kendall County, C = Colomera, M = Miles, El = Elga; data sources as in Fig. 7.

precursors. Melting in an open system should lead to fractionation, either enrichment in the Ab component if feldspar crystallized from a segregated Na-rich partial melt, or enrichment in the An component if feldspar formed by fractional crystallization from a melt of a chondritic precursor. To avoid fractionation, one could have had either (1) minimal melting to begin with, (2) complete, closed-system melting and crystallization of feldspar, or (3) equilibration with unmelted feldspar components. Based on their mineralogies and textures (Section 3), minimal silicate melting is consistent with the data for most IABs, the two unfractionated IIEs Netschaëvo and Techado, Enon (ungr.) and Puente del Zacate (IIIAB). Complete melting of a feldspar component (not necessarily the same as complete whole rock melting) is consistent with the data for fractionated IIEs, Guin (ungr.), and NWA 468 (ungr.). To explain relatively uniform plagioclase compositions between extensively and less melted areas in the IABs Caddo County (Takeda et al., 2000) and Udei Station (Ruzicka and Hutson, 2010), equilibration between melted and unmelted components during metamorphism is a possibility.

The Ca-rich plagioclase found in the ungrouped irons Tucson, Sombrerete ($Ab_{18.1}$), Bocaiuva ($Ab_{43.5}$), NWA 176 ($Ab_{46.5}$) and IAB Kendall County (approximately $Ab_{64.9}$) stands in contrast to the compositions in other irons (Fig. 8). Such relatively calcic feldspar could have formed either by fractional crystallization from a chondrite melt, or by vapor loss of volatile element Na during intense heating. For the calcic feldspar in Sombrerete, fractional crystallization from a melt is the most likely explanation, as this can explain: (1) the coexistence of alkali-rich glasses with calcic feldspar (see below); (2) systematic, normal Ca–Na zoning patterns in plagioclase; and (3) trace element phase compositions that can be modeled by fractional crystallization (Ruzicka et al., 2006). For Tucson, vapor loss is a viable explanation, as it has alkali-free glasses and shows other evidence for intense heating (Nehru et al., 1982). Vapor loss of alkalis was also suggested for Bocaiuva, which has

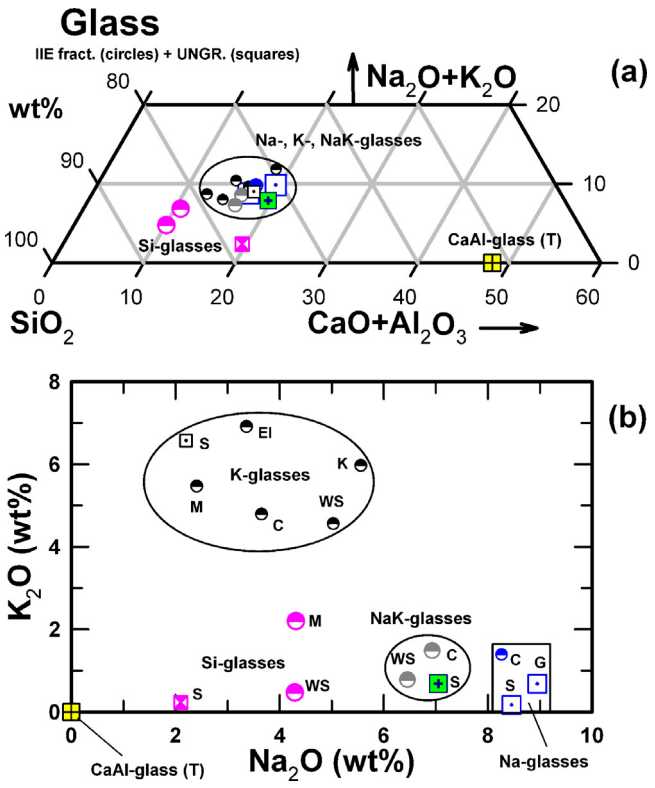

Fig. 9. Average glass compositions in IIE fractionated irons (circle symbols) and ungrouped irons (square symbols). Meteorite abbreviations as in Figs. 1 and 8 and also K = Kodaikanal, WS = Weekeroo Station. Glass types are described in the text. Data sources as in Fig. 7.

metal depleted in volatile siderophile trace elements (Cu, Sb, Ga, Ge) (Malvin et al., 1985).

The presence of alkali feldspars are a notable feature of fractionated IIEs. Some of the K-feldspar crystals have subhedral forms and appear to have crystallized from melt (Fig. 3e). Both phenocrystic K-feldspar and mesostasis alkali feldspar (antiperthite) in Miles were interpreted as having formed by late-stage fractional crystallization (Ikeda and Prinz, 1996; Ruzicka and Hutson, 2010). Takeda et al. (2003a) suggested that sanidine in the large surface inclusion of Colomera crystallized from a segregated K-rich melt that had leached K from surrounding materials. Ruzicka et al. (2006) noted evidence for separation of a K-rich melt by immiscibility in Sombrerete, inferred that this process could have produced K-rich areas that subsequently crystallized the K-rich mineral yagiite, and speculated that a similar immiscibility process could have been the dominant way to create the large K-feldspar-rich Colomera surface inclusion.

Glasses are present in fractionated IIE irons and in some ungrouped irons and consist of different chemical types (Fig. 9). Except for a CaAl-glass in Tucson, the glasses in iron meteorites typically are relatively siliceous (~70–80 wt% SiO_2) and rich in alkalis (~7 wt% $Na_2O + K_2O$) (Fig. 9a). They are subdivided into three types (K-glasses, Na-glasses, and NaK-glasses), depending on their relative Na and K contents (Fig. 9b). K-glasses are present in many fractionated IIEs and Sombrerete, and contain ~2–6 wt% Na_2O and ~4–9 wt% K_2O (Fig. 9b). Sombrerete, Colomera, and Guin contain a Na-rich glass that has ~8–9 wt% Na_2O and <2 wt% K_2O (Fig. 9). NaK-glasses are found in Weekeroo Station, Colomera and Sombrerete and have an intermediate Na and K content (Fig. 9b). A Si-glass is found in Miles, Weekeroo Station, and Sombrerete (Fig. 9). Compared to the alkali glasses, Si-glasses contain more Si and less Na and K.

Different origins have been proposed for the various glasses. The CaAl-glass may have formed by vapor loss of Na and K during intense vaporization (Nehru et al., 1982). For others, immiscibility may have been important (Ruzicka et al., 2006), although Kurat et al. (2007) suggested that alkali fractionation via the involvement of precursor alkali sulfides was more plausible. In Sombrerete, compact regions of K-glass are found clumped around orthopyroxene and plagioclase phenocrysts, suggesting immiscible separation of a K-rich melt that wetted phenocrysts (Ruzicka et al., 2006). Na-glass in Sombrerete is found only in those inclusions that contain either K-glass or yagiite (Ruzicka et al., 2006), and Colomera also contains yagiite and Na-glass, suggesting that the formation of yagiite, Na-glass and possibly K-glass are all linked. The NaK-glasses in Sombrerete are found only in those inclusions that do not also contain Na-glass and K-glass or yagiite, and have compositions that lie on mixing lines between these glasses. Ruzicka et al. (2006) suggested that the NaK-glasses are residual melt that had not immiscibly separated and that had not crystallized yagiite. Na-glass could have formed from a separate Na-rich melt by the removal of K from the residual melt and the incorporation of this K into other phases (yagiite or an immiscible K-rich melt). The Si-glass has the same bulk composition as a glass + plagioclase intergrowth in Sombrerete dubbed "spongy plagioclase" (Fig. 5c), which appears to have formed by rapid crystallization (Ruzicka et al., 2006). Si-glass could have formed by rapid immiscible separation of a Si-rich liquid; solidification of this liquid would produce Si-glass whereas partial crystallization would produce spongy feldspar.

4.2. Trace-element phase compositions

Trace-element phase compositions (Fig. 10a–e) are generally consistent with melting and crystallization processes (Olsen et al., 1994; Ruzicka et al., 1999, 2006; Hsu, 2003; Takeda et al., 2003a; Ruzicka and Hutson, 2006, 2010). The conceptual framework suggested for various meteorites is as follows: (1) Whole-rock melting of H chondrite and subsequent crystallization, for Watson (Olsen et al., 1994); (2) partial melting of an H chondrite-like precursor, followed by localized remelting to form glasses, for Weekeroo Station and Miles (Ruzicka et al., 1999; Hsu, 2003); (3) partial melting of an H chondrite-like precursor, followed by crystallization under two different conditions, for Miles (Ruzicka and Hutson, 2010); (4) partial melting of a CR chondrite-like precursor, followed by fractional crystallization under changing conditions, to form Sombrerete (Ruzicka et al., 2006); (5) spatially variable metamorphism and partial melting of a chondritic precursor, followed by variable equilibration between phases, to form Udei Station (Ruzicka and Hutson, 2010); (6) partial melting of an LL chondrite-like precursor, followed by significant FeO reduction, fractional crystallization, and removal of residual silicate melt, to form Steinbach as a cumulate (Ruzicka and Hutson, 2006); (7) condensation of refractory minerals and silicate liquids followed by interaction with surrounding nebular gas, to form Kodaikanal and Guin (Kurat et al., 2007).

Besides igneous processes, vapor phase partitioning probably was important for fractionated assemblages in the IIEs, Guin, and Sombrerete. Silicates in these irons locally show positive or negative Yb, and less commonly, Sm anomalies in phosphates, orthopyroxene, and glass (Armstrong et al., 1990; Hsu et al., 1997; Hsu, 2003; Takeda et al., 2003a; Ruzicka et al., 2006; Kurat et al., 2007). The origin of the widely observed Yb anomalies is a matter of debate, but probably reflects the presence of a vapor (Ruzicka et al., 2006; Kurat et al., 2007), as Yb (together with Eu and to a lesser extent Sm) can be volatile at high temperatures under reducing conditions (Boynton, 1989; Lodders and Fegley, 1993). More details about the anomalies are provided in Appendix-S3.

Trace element data for low-Ca pyroxene (orthopyroxene) and high-Ca pyroxene (augite-diopside) (Fig. 10a and b) exhibit

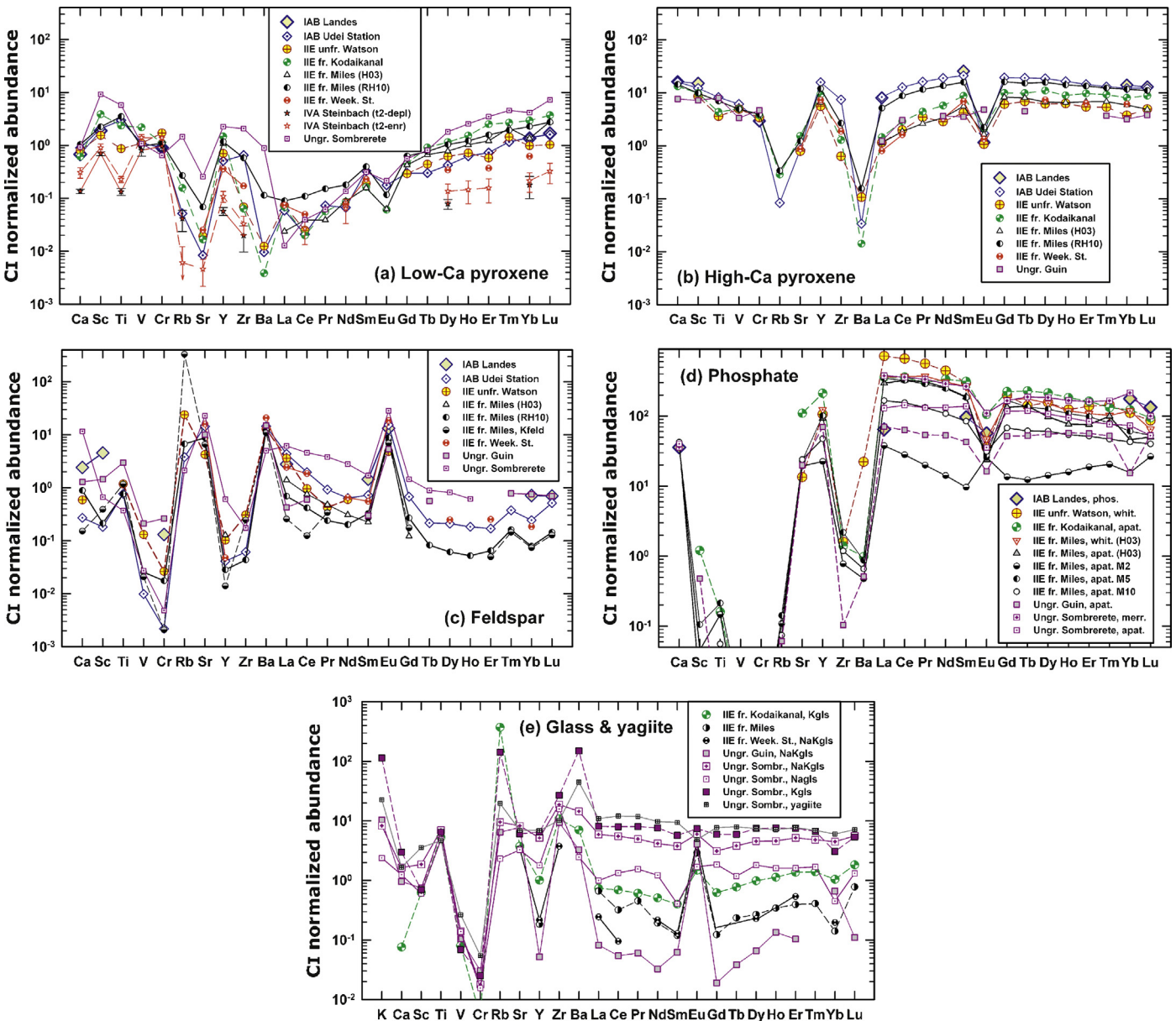

Fig. 10. Average (geometric mean) CI chondrite-normalized trace element abundances for phases in different silicate-bearing irons, including (a) low-Ca pyroxene, (b) high-Ca pyroxene, (c) feldspar including plagioclase feldspar and K-feldspar (Kfeld), (d) phosphate including "whitlockite" (whit), Cl-apatite (apat), and merrillite (merr), (e) various glasses (Kgls = K-glass, NaKgls = Na-K-glass, Nagls = Na-glass) and yagiite. Meteorite abbreviations: Week. St. = Weekeroo Station, Sombr. = Sombrerete. Data sources: *Guin* – Rubin et al. (1986) (Ca-pyroxene, feldspar) and Kurat et al. (2007) (phosphate, glass); *Kodaikanal* – Kurat et al. (2007); *Landes* – Luzius-Lange and Palme (1987); *Miles* – Hsu (2003) (H03) and Ruzicka and Hutson (2010) (RH10); *Sombrerete* – Ruzicka et al. (2006); *Steinbach* – Ruzicka and Hutson (2010) (t2-depl = type 2 depleted; t2-enr = type 2 enriched); Udei Station – Ruzicka and Hutson (2010); *Watson* – Olsen et al. (1994); *Weekeroo Station* – Ruzicka et al. (1999). Data were normalized to the average CI chondrite abundances of Anders and Grevesse (1989).

generally consistent patterns among all of the meteorites, with orthopyroxene showing a more monotonic LREE depletion and augite-diopside showing a more bowed M-shaped REE pattern with a large negative Eu anomaly. The high-Ca pyroxene data reported for Guin lacks a Eu anomaly (Fig. 10b) and possibly reflects contamination with plagioclase in the separated sample.

The compositions of low-Ca and high-Ca pyroxene are nearly identical in two IABs, Landes and Udei Station (Fig. 10a and b). In Udei Station, the high-Ca pyroxene was analyzed in a basalt inclusion (Udei-1B, Fig. 2f), whereas the low-Ca pyroxene was analyzed in multiple lithologies. Feldspar compositions in these two meteorites (see below) are also similar, although less so than for pyroxene. These similarities could be a coincidence, or could indicate that IABs experienced a homogenization process. Ruzicka and Hutson (2010) found that orthopyroxene and plagioclase in Udei Station were in equilibrium with one another, whereas diopside in the basalt was out of equilibrium with the other minerals. This raises the possibility of equilibration occurring under two different conditions. Pyroxene geothermometry implies equilibration in Udei Station under mainly igneous conditions for diopside (1142 ± 36°C) and under mainly metamorphic conditions for orthopyroxene (958 ± 46 °C) (Ruzicka and Hutson, 2010), but these conditions and temperatures may not be relevant for the trace elements.

Data for Steinbach are shown for two kinds of so-called type 2 orthobronzite, one variety more depleted in incompatible elements, and the other more enriched (t2-depl and t2-enr in Fig. 10a, respectively). The pyroxenes were interpreted to have

crystallized over a ~60–70% crystallization interval during fractional crystallization (Ruzicka and Hutson, 2006). Compared to other meteorites, both pyroxenes in Steinbach are depleted in those elements, especially the HREE, Ti, Rb, Y and Zr, that are incompatible in orthopyroxene. Chromium, in contrast, is compatible in orthopyroxene and is slightly enriched in Steinbach orthopyroxene compared to other meteorites. These data suggest that orthopyroxene crystallized from a melt that was less enriched in incompatible elements and that was more enriched in compatible elements than for other irons. Loss of partial melt prior to the melting episode that produced Steinbach (Ulff-Møller et al., 1995) is one possibility to explain the incompatible-element-poor nature of Steinbach pyroxene. Another is that Steinbach may have been derived from a high-temperature, high-degree partial melt (Ulff-Møller et al., 1995; Ruzicka and Hutson, 2006) that subsequently lost the last bit of incompatible-element-rich residual melt during cumulate formation (Ruzicka and Hutson, 2006).

Sombrerete has orthopyroxene enriched in many incompatible elements and has a negative Yb anomaly (Fig. 10a). It possibly crystallized from a relatively evolved melt, such as would be produced by a low degree of partial melting or by extensive fractional crystallization (Ruzicka et al., 2006). However, this interpretation does not explain why only some HREE (Dy-Lu), and not more incompatible REE, have high abundances (Fig. 10a). Also notable is the unusually high Sc, which is moderately incompatible in orthopyroxene (Fig. 10a). These considerations suggest that the trace element composition of orthopyroxene in Sombrerete reflects disequilibrium caused by rapid cooling.

Two sets of orthopyroxene and augite data by different researchers are shown for Miles, one of which (H03) has a negative Yb anomaly for orthopyroxene (Fig. 10a and b). The average values between the two sets differ, but individual analyses overlap. Variations in absolute abundances most likely reflect differences in crystallization extent (Ruzicka and Hutson, 2010). Although there are variations between grains, the average composition of orthopyroxene (Group A) and augite can be modeled as being in approximate equilibrium with melt in a crystal-melt assemblage that was largely (98%) solidified (Ruzicka and Hutson, 2010).

All feldspars have large positive Eu anomalies ($Eu/Eu^* \sim 20–70$), and K-feldspar in Miles is strongly enriched in Rb (~350 × CI chondrites) (Fig. 10c). All feldspars except those in Guin have a tendency to be LREE-enriched ($La/Ho \sim 10–25 \times CI$); the Guin data possibly reflect contamination with pyroxene. Among all irons, feldspar compositions vary significantly in Ca (or An) and to a somewhat lesser extent in REE content, with a tendency for more calcic feldspars to be more enriched in the REE (Fig. 10c). The same trend is observed among individual plagioclase analyses in Miles (Ruzicka and Hutson, 2010). A positive correlation between Ca and REE contents in feldspar is odd from the standpoint of igneous petrogenesis, as lower temperature melts should be less anorthitic and incorporate higher concentrations of incompatible elements. Ruzicka and Hutson (2010) attributed the REE variation in Miles feldspar to REE acting as compatible elements as a result of phosphate co-crystallization (see below). In this case, Ca and REE abundances could co-vary in feldspar.

The phosphates in silicate-bearing irons show large variations in compositions, and a bewildering variety of patterns that have positive and negative Eu and Yb anomalies (Fig. 10d). Merrillite grains all have LREE-enriched patterns with negative Eu anomalies, but two show positive Yb anomalies (Sombrerete, Miles H03) and one shows no Yb anomaly (Watson). For apatite, there are five different REE patterns among six different analyses (Fig. 10d): (1) LREE-enriched with negative Eu and no other anomalies (Kodaikanal, Miles M10); (2) LREE-enriched with a negative Eu and negative Yb anomaly (Miles H03); (3) flat REE with a negative Eu and small positive Yb and Sm anomalies (Sombrerete); (4) flat REE with negative Eu and a negative Yb anomaly and generally low REE abundances (Guin); and (5) W-shaped REE pattern with a positive Eu and a negative Yb anomaly and the lowest REE abundances (Miles M2).

Apatite compositions in Miles and other meteorites can be explained by fractional crystallization of phosphate itself (Ruzicka and Hutson, 2010): During phosphate crystallization, the REE could have been behaving as compatible elements. Crystallization of phosphate in a relatively small volume of melt can cause the melt to become depleted in REE, and subsequent phosphates will be less enriched in REE. The negative Eu anomaly can turn positive because Eu is less compatible than the other REE, creating an inverted pattern. This pattern could become "W-shaped", because the D-value pattern for phosphate can be M-shaped or LREE-enriched, and because the melt itself can be fractionated by silicate–silicate partitioning to a LREE-enriched pattern. Thus, early-crystallizing phosphates could include Miles apatite M10 or whitlockite H03 and a late crystallizing phosphate could include Miles M2 (Fig. 10d). If the early-crystallizing phosphates had positive Yb anomalies (e.g., whitlockite H03 in Fig. 10d), it could produce a negative Yb anomaly in the melt that would appear in later-formed apatites (e.g., Miles apatite H03 and apatite M2 in Fig. 10d).

Glasses show large compositional variability, and generally are poor in REE, Cr, and V (Fig. 10e). Those that are most REE-depleted show a strong, "W-shaped" pattern, whereas those that are least depleted have less pronounced Eu anomalies and flatter patterns. The strongest "W" patterns are for NaK-glass in Guin, Weekeroo Station, and Miles, and for K-glass in Kodaikanal. Three of these have negative Yb anomalies and one (Guin) appears to have a positive Yb anomaly, which would make the latter the only known example of a positive Yb anomaly in a phase from iron meteorites other than phosphate. An irregular REE pattern with negative Sm and Yb anomalies is shown by Na-glass in Sombrerete. The least fractionated REE glass patterns are for NaK-glass and K-glass in Sombrerete, which have small positive Eu anomalies. K-glasses appear generally similar to other glasses except that they are enriched in Rb and K. Yagiite in Sombrerete resembles K-glass in the same meteorite except for being less strongly enriched in K and Rb and having a small negative Eu anomaly (Fig. 10e).

K- and Na-glasses were interpreted based on major-element data to have formed by the combined effects of phosphate crystallization and immiscible separation (Ruzicka et al., 2006), but the trace element compositions seem more dominated by phosphate crystallization. On the other hand, broadly similar compositions for yagiite and K-glass in Sombrerete support the hypothesis that these two phases may have formed in similar ways, possibly involving immiscibility (Ruzicka et al., 2006).

4.3. Trace element models for forming and relating glass to other minerals

Glass is a distinctive phase found in fractionated IIEs and some ungrouped irons such as Guin, Sombrerete, and Tucson. The glasses (at least the alkalic-siliceous variety present in all but Tucson) are chemically distinctive in being depleted in REE, in contrast to what one would normally expect for a late-stage differentiated liquid (Section 4.2). Different models have been advanced to explain the origin of the glass and how it is related to coexisting minerals. These include: (1) glass did not form as a residual melt after the crystallization of other minerals with which it coexists, but rather by remelting in a later impact event (Ruzicka et al., 1999; Hsu, 2003); (2) glass formed by solidification of melt following the crystallization of phosphate, which depleted the melt in elements concentrated in phosphate (Ruzicka et al., 2006; Ruzicka and Hutson, 2010); (3) glass formed as the remnants of a liquid condensate that was interacting with surrounding gas during cooling (Kurat et al., 2007).

There are various arguments in favor of the remelting hypothesis, but the most compelling is that the composition of glass in Weekeroo Station and Miles can be modeled fairly well as a mixture of orthopyroxene and plagioclase, implying that the glass formed by the remelting of these minerals (Ruzicka et al., 1999; Hsu, 2003). Ruzicka et al. (1999) noted that the average glass composition in Weekeroo Station inclusions (Weekeroo NaKgls in Fig. 10e) can be adequately matched for a variety of trace elements (Sr, Y, La, Ce, Nd, Sm, Eu, Dy) by an average of 77% orthopyroxene and 23% Na-plagioclase in the meteorite. They also noted that the proportion of orthopyroxene and plagioclase required for melting was similar to the norm for average H chondrites, about 73:27 = orthopyroxene:feldspar, suggesting that the glass could have formed by almost complete remelting of a noritic protolith that formed by melting of an H chondrite-like precursor.

Hsu (2003) found two different glass patterns in Miles, one that has a LREE-rich pattern with a positive Eu anomaly resembling plagioclase, and the other a HREE-rich pattern that could be modeled as a mixture of 90% feldspar and 10% orthopyroxene. The implication is that glass formed by the melting of relatively coarse-grained precursors of plagioclase and orthopyroxene, with different inclusions sampling various proportions of these minerals.

Ruzicka et al. (1999) noted that although the trace element composition of the glasses could be modeled as melted mixtures of orthopyroxene and plagioclase, their major-element composition could not, with glasses being too siliceous and insufficiently magnesian and ferroan. They suggested that melt lost an $(Mg,Fe)SiO_3$ (orthopyroxene) component prior to solidification, involving crystallization of orthopyroxene in corona structures, and FeO-reduction that removed Fe from silicate and added it to host metal. They suggested that Weekeroo Station inclusions could have formed by two melting episodes, an early one that produced coarse phases which remain as relict pyroxene grains (Ca-rich and Ca-poor), and a later, reducing episode that produced the remainder of the inclusions. The first stage of melting was ascribed to internal differentiation in the parent body and the formation of a gabbroic/noritic crust, and the second stage of melting was ascribed to impact melting of this crust, accompanied by metal–silicate mixing.

The main drawback to this model is that it does not explain why only orthopyroxene and feldspar are involved in the remelting process, and not Ca-pyroxene or phosphate. Also, the model does not explain the variations in trace-element compositions found for phosphate, plagioclase, and glass in fractionated silicates (Fig. 10c–e).

The hypothesis that REE-poor glass solidified following the crystallization of phosphate is supported by various trace element data. Complementary REE patterns for some phosphate and some glass suggests a genetic relationship between the two, with glass forming out of the same chemical system that had previously crystallized phosphate (Ruzicka et al., 2006). “W-shaped” patterns for glasses, with positive Eu anomalies that become more pronounced with lower overall REE contents, are a striking feature of glass (Fig. 10e). These patterns continue and extend the patterns shown by phosphates (Fig. 10d), strongly suggesting that phosphate and glass formed out of the same, evolving system. As fractional crystallization of phosphate can explain the compositions of phosphate minerals (Section 4.2) (Ruzicka and Hutson, 2010), the same is likely true for glass compositions. Complementary or similar anomalies for Yb in phosphate and orthopyroxene are also often seen, which are explained by having some orthopyroxene crystallize from the same magma that had previously crystallized phosphate (Ruzicka et al., 2006).

In Miles, the trace element compositions of most orthopyroxene and augite grains are in equilibrium with one another and not with plagioclase or phosphate, whereas the latter two minerals could have co-crystallized. This led Ruzicka and Hutson (2010).to suggest a model involving two stages of crystallization. In the first stage, low- and high-Ca pyroxene and plagioclase crystallized under slow-cooling conditions at depth in the parent body during a process that was approaching equilibrium crystallization. This was followed by a change to more rapid cooling involving fractional crystallization of phosphate and plagioclase. The second episode may have occurred following an impact event that led to (1) some remelting, (2) more rapid cooling of the silicate, (3) FeO reduction, and (4) metal–silicate mixing and reaction. Silicate glass would be a partial product of impact melting, but would have trace element compositions that reflect the crystallization of phosphate (Ruzicka and Hutson, 2010). However, this model does not reconcile inferences that glass can have a composition created by melting of orthopyroxene and plagioclase and that reflects phosphate crystallization. Another potential drawback is that there is not always a clear connection between the compositions of particular glasses with particular phosphates, possibly because of the limitation in studying three-dimensional inclusions in two-dimensional sections. Finally, the amount of plagioclase that crystallized from impact melt compared to an earlier stage of crystallization is not well defined.

Noting that glass does not have the composition one might expect for igneous differentiation, Kurat et al. (2007) suggested a condensation-metasomatism model for Kodaikanal (IIE) and Guin (ungr.). Glass in Kodaikanal has a typical “W-shaped” pattern with a positive Eu and negative Yb anomaly (Fig. 10e), and apatite has a typical LREE-rich pattern (Fig. 10d). The glass in Guin has a strongly depleted “W shaped” REE pattern with positive Eu and Yb anomalies (Fig. 10e), whereas the apatite has a flat REE pattern with negative Eu and Yb anomalies (Fig. 10d). The system for Guin is in disequilibrium but has a roughly complementary chemical relationship between glass and phosphate. Two slightly different models were proposed by Kurat et al. (2007) to explain the observations for Kodaikanal and Guin. For Kodaikanal, refractory condensate droplets were envisioned to have formed under reducing conditions that crystallized more or less diopside-augite, and which reacted with nebular gas as they cooled under more oxidizing conditions, allowing P and alkalis to enter the melt via a metasomatic process. Apatite was created by reaction of Ca from diopside with P in the liquid. The droplets solidified and the REEs diffused out of the glass by metasomatism to create glass-only or disequilibrium diopside + glass + apatite assemblages. For Guin, a siliceous liquid droplet condensed under reducing conditions after the removal of a high-temperature oldhamite and osbornite condensate from the gas, resulting in REE-poor abundances and positive Eu and Yb anomalies in the silicate droplet. The system cooled and became more oxidizing, and alkalis were added to the melt by metasomatism. Oldhamite and osbornite were transformed into apatite and rutile, respectively, and became embedded in the droplet, which then solidified.

There are significant drawbacks to the condensation-metasomatism model. (1) It does not account for how nebular processes can explain the overall fractionated compositions of the silicates or the particular mineral assemblages that are present; olivine must be removed, and phases such as diopside, albitic feldspar, phosphate and a siliceous glass – phases expected for a chondrite partial melt – must coexist. (2) There is no evidence that refractory precursor phases such as oldhamite or osbornite ever existed in the silicates. (3) It is doubtful that perfectly formed phenocrysts of Cl-apatite in silicate inclusions could represent transformed refractory precursor minerals of different symmetry without leaving textural evidence of the process. (4) There is no evidence for subsolidus diffusion of REE out of the glass – no radial gradients have been reported. (5) It is unclear why two different processes (loss of REE by diffusion out of inclusions, and condensation from a gas that had lost a refractory precursor) are

needed to account for REE-depleted glasses that have broadly similar trace element patterns (Kodaikanal and Guin, Fig. 10e). (6) There is no explanation why diffusion of REE should occur to produce a fractionated "W-shaped" pattern in glass (Fig. 10a), or why such diffusion should go to an extreme to produce a subchondritic REE content. (7) Complementary REE patterns including complementary positive and negative Yb anomalies between glass and other minerals (phosphate, orthopyroxene) are not satisfactorily explained, if the composition of glass is supposed to be the result of metasomatism. (8) It is not clear how coarse silicate phases are accommodated by a model that invokes the presence of a liquid condensate droplet that must cool rapidly to preserve glass and disequilibrium features. (9) The conditions needed to create such droplets are not well defined but would appear to require gas pressures higher than typically assumed for the nebula. (10) The process by which liquid condensates became enclosed in a large volume of metal is not fully articulated, other than to claim that there was "subsolidus deposition of metal" (Kurat et al., 2007), a process that has not received support from other researchers. Given these difficulties, I conclude that the nebular condensation model as discussed by Kurat et al. (2007) does not offer any particular advantages and has some serious shortcomings.

4.4. Phase compositions – summary

Mineral-chemical data are consistent with the idea that the irons could have been derived from chondritic precursors and suggest processes such as differentiation, redox reactions, liquid immiscibility, and vapor phase partitioning. The IIEs could have been derived from one or more H chondrite-like bodies that experienced more (fractionated IIE) or less (unfractionated IIE) differentiation. The FeO contents of silicates were established by differentiation and FeO reduction involving reactions between silicate and metallic components, and also reflect differences in parent body compositions. Feldspar compositions range greatly, from nearly pure anorthite in Tucson (ungrouped), to nearly pure albite in Dayton (IIICD), although most irons (including IABs, various IIEs and ungrouped irons) contain plagioclase that resembles the oligoclase composition of O chondrites. Calcic feldspar in some irons (Sombrerete) formed by fractional crystallization, in others (Tucson) it probably formed by alkali loss during intense heating. But a preponderance of feldspar compositions close to the chondritic value suggests that in most iron meteorites, silicates were derived from chondritic chemical systems with regard to feldspar components. Different glass chemical types are present in the fractionated IIEs and in Guin, Sombrerete, and Tucson, and may have been derived from melts affected by evaporation (CaAl-glass in Tucson) or immiscibility (siliceous-alkali glasses in other meteorites). Major-element and available trace-element data for silicates in IABs indicate they have fairly uniform compositions, suggesting they were equilibrated. Steinbach (IVA) orthopyroxene crystallized from a melt unusually poor in incompatible trace elements. Orthopyroxene, augite, plagioclase, and glass in fractionated IIEs vary considerably in trace element compositions, probably mainly as a result of crystallization processes. An apparent anticorrelation between An content and overall REE content in feldspar can be explained by REE uptake in fractionally crystallizing phosphate, which itself could be a product of redox reactions. This would have caused residual melt to be REE-poor and alkalic. Glasses in fractionated assemblages may be the product of such solidification processes. Another possibility is that such glasses formed by impact-remelting of pre-existing phases. A competing idea, that glasses formed by condensation and metasomatism, has serious shortcomings. A striking feature of fractionated silicate assemblages (fractionated IIEs, Sombrerete, Guin) is the presence of Yb anomalies (common) and Sm anomalies (rare) in various phases (phosphate, orthopyroxene, glass). These anomalies probably indicate exchanges with a vapor phase under reducing conditions at high temperature, pointing to a formation origin that involved gas as an important constituent.

5. Bulk compositions

The bulk compositions of silicates in silicate-bearing iron meteorites provide significant clues for understanding their origins.

5.1. Major-element bulk compositions

Two main compositional groups are evident in plots of bulk silicate ($Na_2O + K_2O$) vs. SiO_2 and MgO (Fig. 11): (1) an alkali-poor, Si-poor, Mg-rich group that overlaps the compositions of chondrites, and (2) an alkali-rich, Si-rich, Mg-poor group. The alkali-poor group includes most of the IABs, including Udei-1A-1, which has a chondritic mineralogy and granoblastic texture (Fig. 2e and g). It also includes the unfractionated IIE irons Netschaëvo and Watson, which have bulk silicate compositions very similar to those of ordinary chondrites (Olsen and Jarosewich, 1971; Olsen et al., 1994). The ungrouped Bocaiuva and Mbosi and IIIAB Puente del Zacate have compositions within the alkali-poor group. One inclusion from Weekeroo Station (WS4) is dominated by coarse orthopyroxene and is unlike other inclusions from the meteorite (Ruzicka et al., 1999) and falls within the alkali-poor group.

The alkali-rich group has 3-7 wt% $Na_2O + K_2O$, 54–66 wt% SiO_2, and 0–19 wt% MgO (Fig. 11). This composition is notably different from that of chondrites. It includes most inclusions in the fractionated IIEs, such as those from Weekeroo Station, Miles, and Colomera, and from the ungrouped Guin and Sombrerete. The alkali-rich group also contains lithologies from the IABs Caddo County and Udei Station, including gabbro from Caddo County, basalt-gabbro inclusion Udei-1B (Fig. 2f), and the poikilitic, feldspathic pyroxenite assemblages in Udei-1A-3 (Fig. 2e and h) and Udei-3B (Fig. 2i, j and k).

Some silicates fall outside the two main groups. Composite silicate from Weekeroo Station (WS, Fig. 11) (Olsen and Jarosewich, 1970) has somewhat less MgO than other silicates in the alkali-poor group. Inclusion WS2 from Weekeroo Station is a pure glass inclusion devoid of ferromagnesian silicates and consequently poor in MgO and rich in SiO_2, but it has total alkali contents similar to those in the alkali-rich group. Some silicates have very low alkali contents (<0.2 wt% $Na_2O + K_2O$). These include the IVA stony irons Steinbach and São João Nepomeceno, the ungrouped Tucson iron, and peridotite in the granular portion of Udei-3B (Fig. 2i, k and l), reflecting very low feldspar and glass contents. Inclusion Miles-9, in contrast, is composed entirely of Na-feldspar, alkali feldspar, and silica (Fig. 3f). It was observed on a section edge and is not representative of Miles as a whole, but does demonstrate that apparently evolved material is present.

Fig. 12 shows bulk compositions of silicates from iron meteorites in an olivine – quartz – plagioclase ternary diagram with superposed cotectic and reaction curves. This multicomponent diagram has an advantage in that comparison can be made to igneous phase equilibria which here refer to a chemical system that has Mg# = 0.7 and a feldspar fraction with normative albite = 0.5 and normative orthoclase = 0.05. The topology of this system is very similar to one that has been suggested to be a better overall match for bulk chondrite (with Mg# = 0.8 and normative albite = 0.9, normative orthoclase = 0.01, and Mg# = 0.8) (Takeda et al., 2003a), so the phase boundaries in Fig. 12 are approximately correct for chondritic systems. O chondrites plot toward the olivine apex in the field labeled "OC". Equilibrium partial melting of this composition

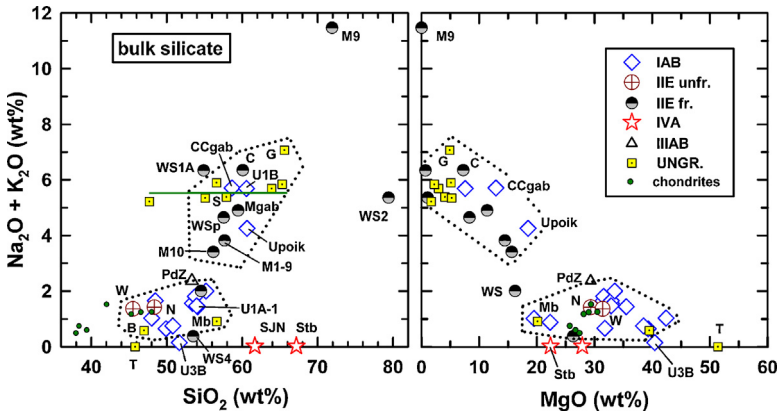

Fig. 11. Average bulk compositions of silicates in different silicate-bearing irons shown in total alkali ($Na_2O + K_2O$) vs. SiO_2 and MgO diagrams. Dotted outlines are shown for the "chondritic" and "alkalic, siliceous" groups. A green horizontal line shows the trend for inclusions in Sombrerete. Data sources and abbreviations: *IAB irons* – Mason (1967), Kracher (1974), Wlotzka and Jarosewich (1977), Olsen and Schwade (1998), Takeda et al. (2000), gabbro in Caddo County (CCgab); Ruzicka and Hutson (2010), including Udei-1A-1 (U1A-1), Udei-1B (U1B), average of poikilitic lithologies in Udei-3B and 1A-3 (Upoik), and average of granular lithogies in Udei-3B (U3B); *IIE unfractionated (IIE unfr.) irons* – Olsen and Jarosewich (1971), Netschaëvo (N); Olsen et al. (1994), Watson (W); *IIE fractionated (IIE fr.) irons* – Olsen and Jarosewich (1970), composite of 12 inclusions in Weekeroo Station (WS); Ikeda and Prinz (1996), average of 27 gabbroic inclusions in Miles (Mgab); Ruzicka et al. (1999), average of 7 peritectic inclusions in Weekeroo Station (WSp), also crystalline felsic inclusion WS1A, glass inclusion WS2, orthopyroxene-rich inclusion WS4; Takeda et al. (2003a), average of 6 interior inclusions in Colomera (C); Ruzicka and Hutson (2010), including Miles-10 (M10), Miles-9 (M9), and composite of smaller inclusions in Miles (M1-9); *IVA stony irons* – Ruzicka and Hutson (2006), Steinbach (Stb); Scott et al. (1996), São João Nepomeceno (SjN); *IIIAB irons* – Olsen et al. (1996b), Puente del Zacate (PdZ); *Ungrouped irons* – Malvin et al. (1985), Bocaiuva (B); Rubin et al. (1986), Guin (G); Olsen et al. (1996a), Mbosi (Mb); Ruzicka et al. (2006), average of 19 inclusions in Sombrerete (S) and also representative inclusions Som-1, Som-4, Som-6, Som-8, Som-15; Nehru et al. (1982), Tucson (T); *chondrites* – Jarosewich (1990), average H silicate, L silicate, LL silicate, CI, CM, CO and CV chondrites, all water- and C-free.

would produce a peritectic melt at composition R until plagioclase was melted, at which point the melt would follow a reaction curve (or cotectic, depending on Fe/Mg ratio) between olivine and low-Ca pyroxene until all low-Ca pyroxene was melted. Further melting would drive the melt composition off the olivine–pyroxene boundary toward the olivine apex until the starting OC composition was reached. If the system were albitic (normative albite = 1) and magnesian (Mg# = 1), the peritectic would shift to point R*. The lowest temperature melt is at the eutectic composition E, a composition that could be reached by fractional crystallization of almost any composition, or by partial melting or equilibrium crystallization from non-chondritic starting compositions.

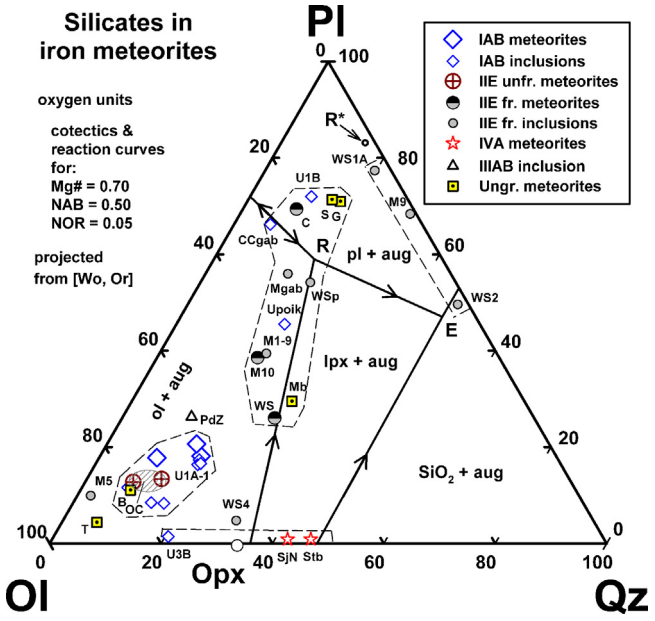

Fig. 12. Average bulk compositions of silicates in different-silicate bearing irons, shown in an olivine (ol) – quartz (qz) – plagioclase (pl) pseudoternary liquidus diagram projected from wollastonite (wo) and orthoclase (or) (see Ruzicka et al., 1999 for an algorithm). Dashed lines indicate 4 groupings discussed in the text. Data sources and abbreviations same as in Fig. 11, except OC = ordinary chondrite silicate (Jarosewich, 1990), M5 = phosphate-rich inclusion Miles-5 (Ruzicka and Hutson, 2010), R = peritectic, R* = peritectic in Fo-Ab-Qz system, aug = augite, lpx = low-Ca pyroxene mineral, SiO_2 = silica mineral.

Silicate compositions from iron meteorites fall into 4 multicomponent groups (Fig. 12). This includes (1) a "chondritic" group, (2) a "peritectic" or "olivine–pyroxene boundary" group, (3) a "felsic" group on the plagioclase – quartz join, and (4) a "feldspar-poor" group on the olivine – quartz join. Virtually all silicates fall into one of these four groups. The most populous is the "chondritic" group. It includes the OC subfield and the bulk compositions of C chondrites (not shown, but with slightly higher olivine/orthopyroxene ratio than OC). The unfractionated IIEs Watson and Netschaëvo and the ungrouped Bocaiuva overlap the OC subfield. Most silicates in IABs fall in the chondritic group, but compared to O chondrites they are often slightly displaced away from the olivine apex. Nearly in this group but slightly feldspathic is the single silicate inclusion in Puente del Zacate. All of these materials fall into the alkali-poor group of Fig. 11 and can be explained as having essentially unfractionated silicate compositions. The chondritic group represents silicates that were either unmelted, or melted without significant silicate melt – silicate solid separation.

That some IAB silicates are displaced away from the olivine apex compared to OC implies that they have slightly subchondritic olivine contents. This includes silicates from Landes, Woodbine, and some inclusions of Campo del Cielo and Udei Station (e.g., Udei-1A-1), whereas other inclusions from Campo del Cielo and Ocotillo are not depleted in olivine. This suggests a small fractionation with more or less olivine in different areas of the IAB parent body. The fractionation cannot be solely ascribed to FeO reduction, for which there is evidence (Section 4.1), as this would create low-Ca pyroxene at the expense of olivine, and would displace compositions from olivine to orthopyroxene at constant plagioclase contents (left to right in Fig. 12), unlike the olivine-depletion trend needed. Another possibility is silicate melt migration, which would produce olivine-depleted melt areas, but there is no textural evidence that inclusions such as Udei-1A-1 (Fig. 2g and e) are the products of such silicate melts. Another possibility is that the IAB parent body, or the sampled portion of it, is slightly poor in olivine

as a result of formation or post-formation processes, but this is very *ad hoc*. A combination of FeO-reduction and minor melt migration can perhaps best explain the data for the "displaced IABs".

The next most populous field in Fig. 12 is one that extends from the expected peritectic composition and up the olivine–pyroxene boundary. Most inclusions from the fractionated IIEs lie in this field, including silicates from Weekeroo Station, Miles, and Colomera. Also within this field are silicates from IABs, including the gabbro from Caddo County, the basalt-gabbro Udei-1B (Fig. 2f), and the poikilitic feldspathic orthopyroxenite observed in different areas, including Udei-3B (Fig. 2j and k) and Udei-1A-3 (Fig. 2h). Silicates from the ungrouped irons Mbosi, Guin, and Sombrerete also lie within this field. All silicates in the peritectic/olivine–pyroxene group can be explained as the products of partial melting from a chondritic precursor similar to O or C chondrites (Ikeda and Prinz, 1996; Ikeda et al., 1997; Ruzicka et al., 1999, 2006; Takeda et al., 2000, 2003a; Ruzicka and Hutson, 2010).

A significant feature of the peritectic or olivine–pyroxene boundary group is the distribution of compositions from close to the peritectic R or R* part way up the olivine–pyroxene boundary. This is exactly what one would expect for partial melts of chondritic precursors produced by variable degrees of partial melting. At the low-melting-degree end are "peritectic" silicates, including inclusions from Sombrerete, Guin, Colomera, the basaltic or gabbroic inclusions in Caddo County and Udei Station, gabbroic inclusions in Miles (Mgab in Fig. 12 and Table 5b), and the so-called peritectic inclusions in Weekeroo Station (WSp in Fig. 12 and Table 5b). In Weekeroo Station, they include both glassy (Fig. 3h) and crystalline (Fig. 3i) varieties. All of the peritectic materials could have been formed by either incomplete melting of feldspar in the source region or melting just to the point of feldspar exhaustion.

At the high-melting-degree end are silicates that trend along the olivine–pyroxene boundary, which can be explained by progressive melting following the exhaustion of plagioclase in the source region of a chondritic parent body. With increasing degrees of melting, this includes the poikilitic inclusions in Udei Station, the large silicate inclusion Miles-10 and a composite set of inclusions in Miles (M10, M1-9, Fig. 12 and Table 3b), silicate in Mbosi, and a composite of silicate inclusions from Weekeroo Station (WS in Fig. 12). The latter corresponds approximately to the composition one would get at which all low-Ca pyroxene in an O chondrite precursor would have been melted (Olsen and Jarosewich, 1970). The composition of this composite of Weekeroo Station inclusions is much less feldspathic than the peritectic inclusions in the same meteorite (WS vs. WSp, Fig. 12). This can be explained if the WS composite has a roughly equal mixture of peritectic inclusions and orthopyroxene-rich inclusions such as WS4. If the WS composition is representative, it implies that orthopyroxene-rich inclusions in Weekeroo Station are much more prevalent than those studied by Ruzicka et al. (1999) and Evensen et al. (1979).

Some isolated inclusions from the fractionated IIEs lie along the plagioclase – quartz join and form the felsic group. These include inclusions from Weekeroo Station, Colomera, and Miles (Ruzicka et al., 1999; Takeda et al., 2003a; Ikeda and Prinz, 1996; Ruzicka and Hutson, 2010). WS2 is pure glass similar in composition to that expected for the euctectic (Fig. 12). Inclusion Miles-9 (Fig. 3f) is displaced toward plagioclase from this eutectic, as are crystalline felsic inclusions such as WS1 and WS10B (Fig. 3j). It has been suggested that felsic inclusions could have formed in one of two ways, by either: (1) remelting of feldspathic materials, accompanied by FeO-reduction (Ruzicka et al., 1999), or (2) separation of feldspathic melts from a crystal – liquid mush (Ikeda and Prinz, 1996; Ikeda et al., 1997; Takeda et al., 2003a). Possibly both processes occurred to some extent. If melt (impact-generated or not) did become separated from crystals to form feldspathic melts, FeO-reduction would help drive the composition of the melts to the plagioclase – quartz join. Crystallization of plagioclase could then ensue to create inclusions that had variable proportions of plagioclase and residual eutectic melt (Takeda et al., 2003a). Different amounts of trapping of feldspar and melt during solidification would produce a variety of crystalline felsic inclusions or glass.

A group of silicates extremely depleted in normative feldspar includes the IVA stony irons Steinbach and São João Nepomeceno (Fig. 4) and the granular portion of Udei-3B in Udei Station (Fig. 2i, k and l). These have very different mineralogies and probably formed in different ways. The IVA stony irons are orthopyroxene- and tridymite-rich and have compositions close to the low-Ca pyroxene – silica cotectic (Fig. 12). They probably formed as cumulates of melts that had reached this cotectic (Ulff-Møller et al., 1995; Ruzicka and Hutson, 2006; Wasson et al., 2006). The granular portion of Udei-3B, in contrast, is rich in both olivine and orthopyroxene and almost certainly formed as a restite after the extraction of feldspathic materials.

Aside from pure silica inclusions in IVA Gibeon and Bishop Canyon and IVB Santa Clara, only a few silicates do not have compositions that fall into one of the four groups described above. This includes some inclusions from fractionated IIEs and Tucson (Fig. 12). Orthopyroxene-rich inclusions such as WS4 in Weekeroo Station are not representative and may contain xenocrystic orthopyroxene (Ruzicka et al., 1999). Other inclusions such as Miles-5 are rich in orthopyroxene and phosphate (Ruzicka and Hutson, 2010) and are unrepresentative samples of Miles silicate in containing little feldspar and Ca-pyroxene. Silicate in Tucson has a composition displaced from the chondritic field toward the olivine apex (Fig. 12). This indicates that an olivine component is enriched. Possibly the inclusions consist mainly of residual olivine from which silicate melt was removed.

5.2. Trace-element bulk compositions

The IABs mostly contain silicates only weakly fractionated compared to a chondrite composition (Fig. 13a). An unfractionated silicate would have abundances of ~1–2 × CI chondrites for most elements, depending on the exact protolith and whether more or less metal and sulfide were included in the analysis (e.g., Udei Station inclusion 1A-1, Figs. 2g and 13a). Many of the unfractionated silicates have small depletions in V, Cr, and Mn (Fig. 13a). This could indicate undersampling of chromite, which is rich in V and Cr, but probably does not account for the depletion in Mn. Low abundances of the three elements could thus be a signature of weakly fractionated IABs. An inclusion of Campo del Cielo (Fukuoka and Schmitt, 1978) is more fractionated and has a slightly LREE-depleted pattern with low abundances of Na, Al, and Ca, suggesting that it has a subchondritic proportion of feldspar. Other analyses of Campo del Cielo have higher abundances of Na and Al, lower abundances of Ca and most REE except Eu, and may have incompletely sampled phosphate (Bild, 1977). Despite these sampling issues, the data strongly suggest that any separation of liquid from solid silicate was very limited in most IABs.

Nonetheless, strongly fractionated compositions are shown for some samples in Caddo County and Udei Station (Fig. 13b), suggesting that there was silicate solid–liquid separation locally within the IAB body. These include materials interpreted as melts, melt residues, and possible melt–solid mixtures. Basaltic materials in Caddo County and Udei Station (Udei-1B) have similar compositions, although the latter is richer in Na, K, and Ca and poorer in Mg (compare CCgab and U1B in Table 5a and Fig. 13b). They are enriched in incompatible elements and less enriched in the more compatible elements Mg, Mn, and Cr (Fig. 13b). A small negative Eu anomaly is present in Caddo County. The REE pattern for the Udei Station basalt lacks an Eu anomaly but is bowed upwards in the center (Fig. 13b). These data were interpreted as reflecting the

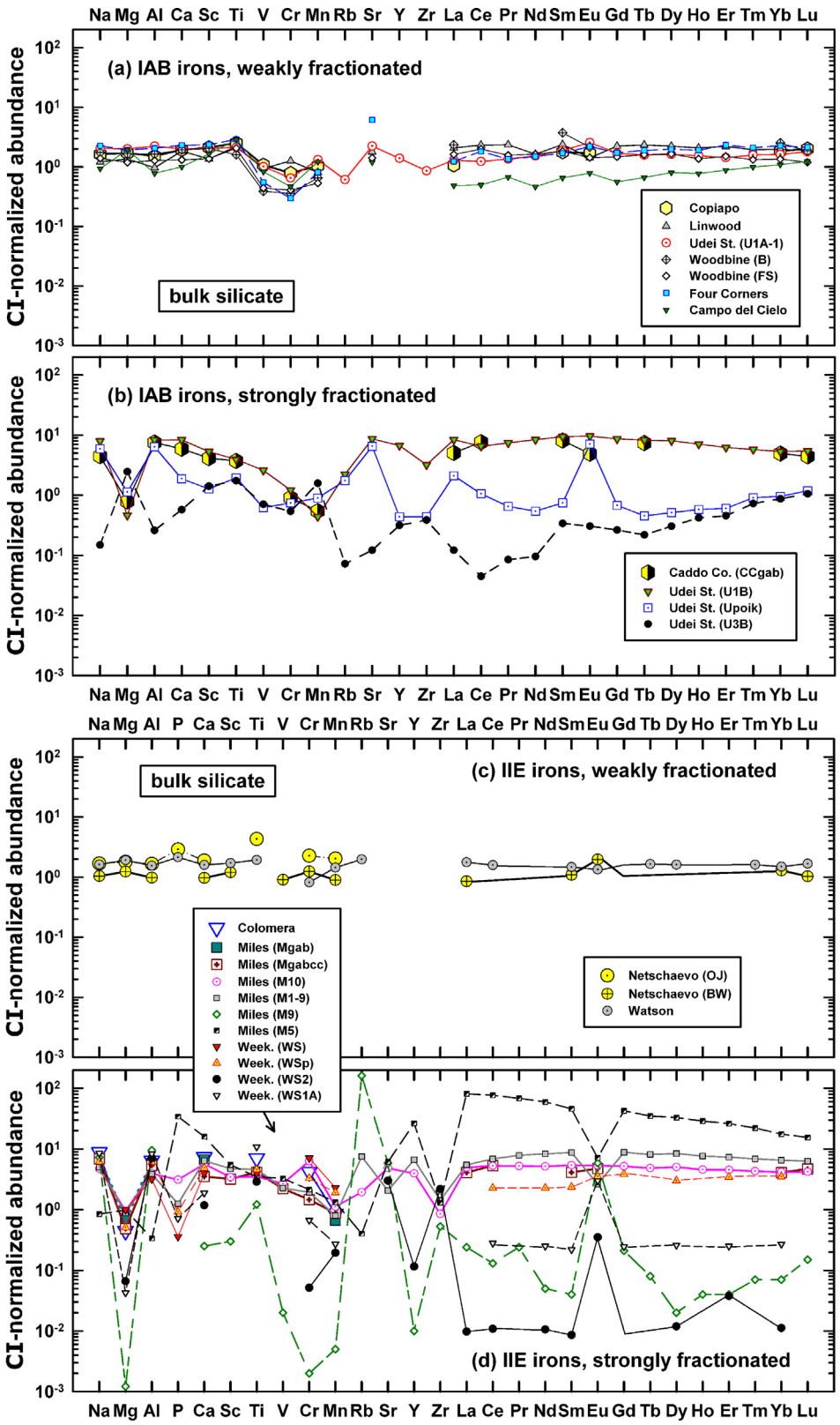

Fig. 13. Average (geometric mean) CI chondrite-normalized trace element abundances for bulk silicates in different silicate-bearing irons, including (a) weakly fractionated IAB materials, (b) strongly fractionated IAB materials, (c) weakly fractionated IIE materials, (d) strongly fractionated IIE materials, (e) feldspathic materials in ungrouped irons, and (f) chondritic to ultramafic materials in ungrouped irons. Data sources and abbreviations: *Bocaiuva* – Malvin et al. (1985); *Caddo County (Caddo Co.)* – Takeda et al. (2000) (CCgab), gabbro; *Campo del Cielo* – Fukuoka and Schmitt (1978); *Colomera* – Takeda et al. (2003a), average of 6 interior inclusions; *Copiapo* – Bild (1977); *Enon* – Kallemeyn and Wasson (1985); *Four Corners* – Fukuoka and Schmitt (1978); *Guin* – Rubin et al. (1986); *Linwood* – Fukuoka and Schmitt (1978); *Mbosi* – Olsen et al. (1996a), trace elements estimated from graphs; *Miles* – Ikeda and Prinz (1996) (Mgab), average of 27 gabbroic inclusions; Ebihara et al. (1997) (Mgabcc), mass-weighted average of 9 gabbroic and cryptocrystalline inclusions; Ruzicka and Hutson (2010) (M10, M1-9 composite, M9, M5); *Netschaëvo* – Olsen and Jarosewich (1971) (OJ); Bild and Wasson (1977) (BW); *NWA 468* – Rubin et al. (2002); *Puente del Zacate* – Olsen et al. (1996b), silicate portion excluding FeS, C, metal, REE estimated from graph; *Sombrerete (Sombr.)* – Ruzicka et al. (2006), inclusions Som-1 (S1), Som-4 (S4), and average phosphate-rich segregation (Sombr. segr.); *Udei Station (Udei St.)* – Ruzicka and Hutson (2010) (regions

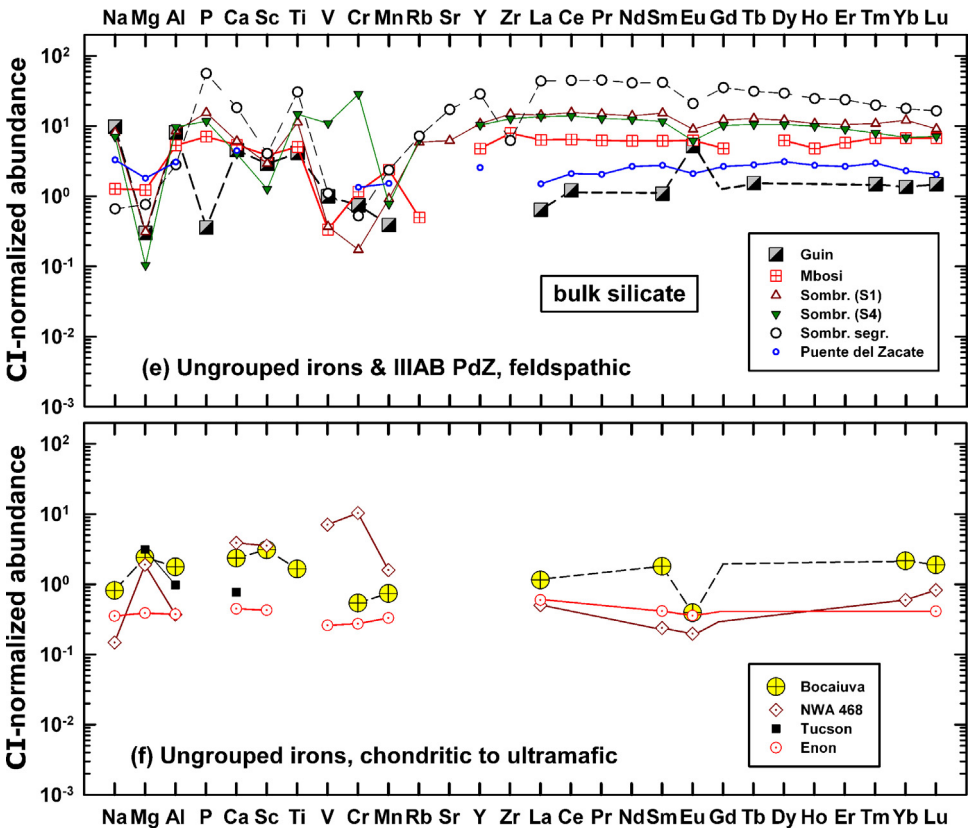

Fig. 13. (*Continued*)

formation of partial melts, either locally and *in situ* within Caddo County (Takeda et al., 2000), or in the form of a basalt lithology that was separated as a clast (Ruzicka and Hutson, 2010). The data for the Udei-1B basalt are generally consistent with ~10–20% partial melting of a chondritic precursor, but the bowed pattern is not consistent with the basalt being an unprocessed melt sample (Ruzicka and Hutson, 2010). Plagioclase and diopside are out of equilibrium, suggesting a complicated evolution that involved equilibration under different conditions (Ruzicka and Hutson, 2010). Plagioclase and clinopyroxene are similarly out of equilibrium for Sm and Nd in a sample of Caddo County (Stewart et al., 1996), suggesting that this may be a feature of IABs containing coarse clinopyroxene. In any case, the lack of an Eu anomaly in Udei-1B is more consistent with partial melting closer to 20% than 10%.

The granular areas within Udei-3B represent different types of peridotite and are depleted in most incompatible elements (U3B, Fig. 13b and Table 5a). Elements that would most partition into a partial melt (the LREE and MREE, Rb, Sr, Na, Al, Y, Zr) are the most depleted, and elements that would least partition into a partial melt (Mg, Mn, Sc) are not depleted (Fig. 13b). (Titanium is also not depleted, for reasons that are not clear.) This composition was modeled as corresponding to a residue during 3–10% equilibrium partial melting (Ruzicka and Hutson, 2010). This is lower than the degree of partial melting needed to create the basalt lithology in the meteorite, suggesting formation of the peridotite and basalt in different settings in the parent body.

Adjacent to the peridotite in Udei-3B across an apparent igneous contact is a poikilitic lithology that is also present elsewhere in the meteorite (Fig. 2j and h). This lithology has a distinctive trace element composition with a strong positive Eu anomaly and high Sr, Na, and Al (Fig. 13b). It reflects an abundance of plagioclase, which poikilitically encloses other minerals, chiefly orthopyroxene but also olivine. The abundances of some incompatible elements such as Y, Zr, and the HREE are similar in the poikilitic lithology as in the peridotite, and the same is true for less incompatible transition elements (Sc, Ti, V, Cr) (compare Upoik with U3B, Fig. 13b). This suggests that the poikilitic lithology has a mixed liquid and solid character, and that it probably formed as a partial cumulate with feldspathic liquids enveloping mafic phases (Ruzicka and Hutson, 2010).

As with the IAB parent body, the IIEs contain both unfractionated and fractionated lithologies, except that in the IIEs a given meteorite has one or the other. Relatively flat, unfractionated abundances occur in Netschaëvo and Watson (Fig. 13c). The lithophile elements have an average abundance of $1.64 \pm 0.29 \times$ CI for Watson (mean and standard deviation), and $1.14 \pm 0.28 \times$ CI for Netschaëvo (Bild and Wasson, 1977), with the latter containing some metal as evident from elevated Fe and Ni contents (Table 5a). These are essentially indistinguishable from chondritic values.

The fractionated IIEs Colomera, Weekeroo Station, and Miles, in contrast, contain silicates with fractionated compositions (Fig. 13d). Different inclusions have such variable trace element compositions that it is difficult to be sure what is representative for the meteorites overall. In general, smaller individual inclusions are more fractionated, whereas larger inclusions or composites are less fractionated though still enriched in most incompatible elements.

U1A-1, U1B, Upoik, U3B); *Tucson* – Nehru et al. (1982); *Watson* – Olsen et al. (1994); *Weekeroo Station (Week. St.)* – Olsen and Jarosewich (1970) (WS), average of 12 random inclusions; Evensen et al. (1979) (WSp, REE only), average of 4 peritectic inclusions, and also inclusion crystalline felsic inclusion WS1A estimated from graph; Ruzicka et al. (1999) (WSp, major elements only), average of 7 peritectic inclusions, and also glass inclusion WS2; *Woodbine* – Bild (1977) (B), Fukuoka and Schmitt (1978) (FS). Data were normalized to the average CI chondrite abundances of Anders and Grevesse (1989).

Table 5a
Bulk compositions of silicates in selected IAB irons and in the ungrouped irons NWA 468 and Bocaiuva.

Meteorite Area		Campo del Cielo 5 incl.	Campo del Cielo	Four corners	Linwood	Woodbine	Udei Station Granular, U1A-1	Caddo County Gabbro, CCgab	Udei Station Basalt, U1B	Udei Station Poikilitic, Upoik	Udei Station Granular, U3B	NWA 468	Bocaiuva
Na	mg/g	7.42	4.67	11.4	6.1	7.0	10.3	22.3	39.8	29.6	0.740	0.74	4.1
Mg	wt%	22.7	19.2	19.0	13.4	11.8	19.8	7.79	4.57	11.1	24.4	18.7	23.8
Al	mg/g	14.8	6.77	18.0	8.42	11.1	19.1	65.4	70.7	54.8	2.12	3.2	15.3
Si	wt%	23.9					25.2	27.4	28.3	28.3	24.1		22.0
P	mg/g	1.27											
K	µg/g	660	290	980	490	630	664	1500	2740	2160	415	15	249
Ca	mg/g	11.8	9.3	21	17	12	18.2	55.1	78.2	16.6	4.92	36	21.9
Sc	µg/g		9.6	13.8	7.9	8	11.9	24.1	30.8	7.41	8.23	20.6	18.0
Ti	mg/g	0.78	1.3	1.3	0.96	0.90	1.08	1.6	1.92	0.955	0.839		0.72
V	µg/g		47	31	53	25	57.1		147	35.2	39.8	398	
Cr	mg/g	1.6	1.24	0.794	3.4	1.09	1.85	2	3.63	1.38	1.50	27.5	1.4
Mn	mg/g	2.9	2.42	1.61	1.60	1.06	2.71	1.1	0.929	1.84	3.29	3.16	1.5
Fe	wt%	3.50	4.59	2.90	5.99	25.1	3.66	5.06	0.700	2.30	4.51	134	47.1
Co	µg/g		383	71	103	1220	2.51	104	1.51	2.51	3.16	85	254
Ni	mg/g		1.19	1.52	1.63	9.95		3.55				1.8	22.9
Zn	µg/g		217	206	438	699		119				48	
Ga	µg/g						2.10		6.60	5.19	0.592	1.30	0.6
Rb	µg/g						1.40		5.13	4.03	0.166		
Sr	µg/g		9.3	48	14	11	17.5		67.5	50.8	0.949		
Y	µg/g						2.17		10.5	0.683	0.491		
Zr	µg/g						3.39		12.6	1.73	1.52		
Nb	µg/g						24.6		71.3	22.9	13.5		
Ba	µg/g		3.4	8.6	16.6	13.5	5.15		19.6	15.4	0.285		
La	ng/g		114	290	490	380	305	1190	1420	495	21.6	118	270
Ce	ng/g		300	1100	1400	1200	742	4610	3940	639	27.0		
Pr	ng/g		60	120	210	140	121		660	58.1	7.56		
Nd	ng/g		210	680	740	740	692		3800	245	43.2		
Sm	ng/g		96	250	350	270	278	1190	1380	110	49.8	35	265
Eu	ng/g		44	124	79	80	143	275	539	397	17.1	11	22
Gd	ng/g		110	340	440	290	334		1700	134	51.9		
Tb	ng/g		24	69	85	58	57.4	267	299	16.4	7.95		
Dy	ng/g		195	480	540	400	393		1960	125	73.9		
Ho	ng/g		43	106	116	76	85.6		394	32.2	23.3		
Er	ng/g		140	370	350	240	227		992	95.9	72.3		
Tm	ng/g		24	51	47	32	38.2		140	22	17.5		
Yb	ng/g		177	370	320	220	263	803	866	155	141	97	350
Lu	ng/g		30	52	46	29	43.5	108	132	28.9	25.6	20	46
Reference[a]		WJ77	FS89	FS89	FS89	FS89	RH10	T00	RH10	RH10	RH10	R02	M85

[a] WJ77 = Wlotzka and Jarosewich (1977); FS89 = Fukuoka and Schmitt (1978); RH10 = Ruzicka and Hutson (2010), inclusions Udei-1A-1 (chondritic), 1A-3 (poikilitic), 1B (basaltic), and 3B (poikilitic and peridotitic); T00 = Takeda et al. (2000); R02 = Rubin et al. (2002); M85 = Malvin et al. (1985).

Table 5b
Bulk compositions of silicates in selected IIE irons and in the ungrouped iron Sombrerete.

Meteorite Area		Netschaëvo	Netschaëvo	Watson	Weekeroo Station WSp	Weekeroo Station WSp	Colomera 6 incl.	Miles Mgab	Miles Mgabcc	Miles M10	Miles M9	Miles M5	Sombrerete S1
Na	mg/g	8.4	5.2	8.1	30.9		44.1	34.5	34.5	23.7	36.3	4.2	40.3
Mg	wt%	17.7	12.2	18.9	5.02		4.38	6.86	4.79	9.44	0.012	9.76	3.08
Al	mg/g	14.4	8.5	13.4	52.6		55.7	51.0	46.4	34.2	82.8	2.9	74.1
Si	wt%	22.6		21.3	26.9		28.1	27.8		26.3	33.6	19.5	26.5
P	mg/g	3.5		2.6	1.12					3.8		41.9	18.9
K	µg/g	2400	620	2300	4040		3000	2080	8500	1830	54,600	80	3900
Ca	mg/g	17.5	9	14.8	45.2		67.9	62.3	32.6	55.6	1.6	150	56.4
Sc	µg/g		7	9.97					18.6	20	1.75	31.8	17.1
Ti	mg/g	1.9		0.84	2.00		3.1		1.80	2.0	0.24	2.5	4.9
V	µg/g		51						125	152	1.13	184	20.8
Cr	mg/g	6.0	3.3	2.17	8.78		11.2		3.90	4.7	0.005	5.7	0.5
Mn	mg/g	4.1	1.78	2.9	3.79		1.7	1.3	1.75	2.6	0.01	2.6	1.9
Fe	wt%	10.2	41.0	10.8	5.28		2.97	3.61	9.37	6.35	0.54	5.89	3.45
Co	µg/g		1.72	47.1					337	65.3	151	326	
Ni	mg/g		33	0.629					7.85				0.099
Zn	µg/g		22.1	34.3					190	215	1.56	71.8	
Ga	µg/g		13.4							8.3	36.2	1.60	
Rb	µg/g			4.54						4.46	373	0.920	13.5
Sr	µg/g									37.7	45.7	47.8	48.4
Y	µg/g									6.16	0.016	41.5	16.8
Zr	µg/g									3.35	2.09	5.08	58.3
Nb	µg/g									81.2	27.1	157	5880
Ba	µg/g									12.7	22.1	1.29	23.4
La	ng/g		200	414		120			960	1160	56.3	19100	3360
Ce	ng/g			953		1400			3210	3180	78.4	46300	9410
Pr	ng/g									467	21.4	6100	1320
Nd	ng/g					1000				2330	22.6	27000	6330
Sm	ng/g		160	217		350			606	797	5.88	6740	2250
Eu	ng/g		110	74.9		200			266	299	328	400	502
Gd	ng/g									1020	41.3	8360	2399
Tb	ng/g			59.8						176	2.9	1260	465
Dy	ng/g			391		730				1220	4.85	7980	2940
Ho	ng/g									254	2.22	1600	600
Er	ng/g					550				717	6.36	4160	1670
Tm	ng/g			39						104	1.69	535	261
Yb	ng/g		210	242		570			665	676	11.4	2860	1970
Lu	ng/g		25	40.6					114	102	3.65	377	221
Reference[a]		OJ70	BW77	O94	R99	E79	T03	IP96	E97	RH10	RH10	RH10	R06

[a] OJ70 = Olsen and Jarosewich (1970), silicate fraction; BW77 = Bild and Wasson (1977); O94 = Olsen et al. (1994); R99 = Ruzicka et al. (1999), average of 7 peritectic inclusions (WSA, WSB, WS1B, WS5A, WS5B, WS6, WS7); E79 = Evensen et al. (1979), average of 4 peritectic inclusions (WS1B, WS5A, WS6, WS7, values estimated from plot); T03 = Takeda et al. (2003a); IP96 = Ikeda and Prinz (1996); E97 = Ebihara et al. (1997), weighted average (by mass) of 9 gabbroic and crypto-crystalline inclusions; RH10 = Ruzicka and Hutson (2010), inclusions Miles-10, Miles-9, Miles-5; R06 = Ruzicka et al. (2006), inclusion Som-1.

This suggests a sampling effect, whereby smaller inclusions are unrepresentative of the whole (Ruzicka and Hutson, 2010). Among the smaller inclusions, compositions range by about 4 orders of magnitude in REE abundances (Fig. 13d and Table 5b). This includes (1) REE-rich inclusions such as Miles-5 (M5), which is rich in phosphate; (2) REE-poor inclusions such as WS1A and WS2 in Weekeroo Station, which are rich in plagioclase and tridymite; (3) REE-poor inclusions such as Miles-9 in Miles (M9), which is rich in plagioclase + alkali feldspar + tridymite; and (4) REE-poor inclusions such as WS2, which is pure glass. In general, inclusions with more phosphate contain higher REE abundances and negative Eu anomalies, and those with more feldspar or glass contain lower REE abundances and positive Eu anomalies. This indicates a strong mineralogical control for the bulk inclusion compositions. Ruzicka and Hutson (2010) modeled the Miles-9 inclusion composition, as well as the mesostasis composition of alkali feldspar + tridymite found in some Miles inclusions, as being the result of fractional crystallization by phosphate. To first approximation this can explain the inverted REE patterns in Fig. 13d.

The larger inclusions and composites show less extreme fractionations, such as Miles-10 (Fig. 3c and d; M10 in Fig. 13d and Table 5b). It has a composition similar to a mass-weighted composite of different gabbroic and cryptocrystalline inclusions in Miles calculated from data obtained by Ebihara et al. (1997) (Mgabcc in Fig. 13d and Table 5b), and to an average of many gabbroic inclusions analyzed in Miles by Ikeda and Prinz (1996) (Mgab in Fig. 13d and Table 5b). The main differences are that Miles-10 is richer in Mg and poorer in Al (Table 5b). Miles-10 has an almost flat REE pattern slightly enriched in the LREE, with abundances of 4–5 × CI (Fig. 13d). This composition is as expected for a partial melt, and can be modeled as having formed as an equilibrium batch melt of an H chondrite-like source with 25–30% partial melting (Ruzicka and Hutson, 2010).

Other compositions in Fig. 13d and Table 5b for fractionated IIEs include aggregate silicate in Weekeroo Station (WS, Olsen and Jarosewich, 1970), an average of inclusions with peritectic compositions in Weekeroo Station (WSp, Ruzicka et al., 1999), and an area-weighted composite of smaller inclusions in Miles (M1-9, Ruzicka and Hutson, 2010). These compositions are reminiscent of Miles-10 but differ in ways that suggest more or less sampling of different minerals, including: excess orthopyroxene and less phosphate in WS, excess augite and less phosphate in M1-9, and less phosphate in WSp. These variations do not appear to be related to igneous differentiation but can be explained by sampling more or less different minerals in inclusions that trapped different proportions of various phases. These composites are approaching the overall composition of the silicates in the irons but are still not entirely representative.

Bulk chemical data for silicates in ungrouped irons and Puente del Zacate are separated into those that have relatively feldspathic (Fig. 13e) and those that have relatively chondritic or ultramafic compositions (Fig. 13f), based arbitrarily on whether CI chondrite-normalized $(Al/Mg)_{CI}$ >1 or ≤1, respectively. For Sombrerete, the bulk compositions of two inclusions as well as for average phosphate segregation are shown. For Mbosi silicate, the trace element abundances were estimated from data given in Olsen et al. (1996a); for Puente del Zacate, REE abundances were estimated from a plot (Olsen et al., 1996b).

The feldspathic inclusions in Fig. 13e include those that vary from only slightly enriched in incompatible elements, as in Puente del Zacate, to those that are considerably more enriched in many incompatible elements (Al, P, Ca, Ti, Y, Zr, REE), as in Mbosi and Sombrerete. Inclusion Som-4 (S4) is unusually rich in chromite, whereas Som-1 (S1, Fig. 13e and Table 5b) is poor in the mineral, accounting for alternately high or low V and Cr. The trace element compositions of silicates in Sombrerete were attributed to a low degree of partial melting (~4–8%) insufficient to exhaust plagioclase in the chondritic source region and leading to a negative Eu anomaly for Sombrerete melt (Fig. 13e) (Ruzicka et al., 2006). A higher degree of melting can be inferred for Mbosi, based on lower enrichments in incompatible elements and the lack of an Eu anomaly (Fig. 13e).

The inclusion of Guin is highly felsic, and has high Na and Al and low Mg similar to those in Sombrerete (Fig. 13e). This was attributed to a mixture of 62% plagioclase, 25% orthopyroxene, and 13% diopside that was melted in a chondritic source by impact (Rubin et al., 1986). However, it is also possible that the composition reflects phosphate removal: The low P and REE and positive Eu anomaly are roughly a mirror image of the phosphate-rich materials in Sombrerete (Fig. 13e), suggesting removal or incomplete sampling of phosphate.

The silicates in Enon, Bocaiuva, Tucson, and NWA 468 range from chondritic to ultramafic. Enon has relatively unfractionated compositions but lithophile abundances are low owing to a high proportion of metal (Fig. 13f, Kallemeyn and Wasson, 1985). Bocaiuva has roughly chondritic abundances, except for a prominent negative Eu anomaly (Fig. 13f). Sodium and K are low in Bocaiuva (Table 5a), possibly owing to vapor loss during impact heating (Malvin et al., 1985). A high Mg/Al together with the negative Eu anomaly suggests that Bocaiuva could be deficient in feldspar relative to mafic minerals. This is supported by a measured modal abundance of 10% plagioclase (Malvin et al., 1985), which is somewhat subchondritic. Compared to Bocaiuva, Tucson has even lower Al and higher Mg (Fig. 13f) and is more enriched in mafic minerals relative to feldspar (Section 5.1). Interestingly, this iron resembles Bocaiuva in having low alkalis (evident in glass and feldspar) (Section 4.1), possibly caused by vapor loss. The most depleted in feldspar is NWA 468. Rubin et al. (2002) noted a chemical resemblance to lodranites (melt residues, e.g., Mittlefehldt et al., 1998). NWA 468 (Table 5a and Fig. 13f) is unsually rich in Cr and V, probably owing to an oversampling of chromite, but is otherwise depleted in REE, Na, and Al, with concentrations of all but La at levels similar to those in the peridotite restite from Udei Station. However, the two materials differ significantly in that NWA 468 has higher Ca, Sc and La and lower Mg and K (Table 5a). Thus, if NWA 468 silicate is a melt residue, it is chemically different than the one in Udei Station.

5.3. Bulk compositions – summary

The compositions of silicates in irons can be grouped into those with no or limited fractionation from a chondritic composition, and those that are more fractionated. Chondritic compositions are prevalent for the IABs and unfractionated IIEs Netschaëvo and Watson and the ungrouped Enon. Silicates in Bocaiuva (ungr.) and Puente del Zacate (IIIAB) are similar to chondrite but have slight depletions or enrichments in feldspar, respectively. Collectively, these silicates were either unmelted, or melted in such a way as to avoid significant silicate melt – silicate solid separation. Other silicate materials are more fractionated and were affected by igneous differentiation, including: (1) all silicates in the fractionated IIEs, (2) some in the IABs, (3) those in the ungrouped Guin, Sombrerete, Mbosi, NWA 468, and Tucson, and (4) the IVA stony irons Steinbach and São João Nepomeceno. The differentiated silicates can be placed into various groups that can be interpreted as melts, melt residues, cumulates, and partial cumulates. The compositions of many differentiated silicates ("gabbroic", "basaltic", "andesitic", "feldspathic pyroxenite") are enriched in alkalis and Si and depleted in Mg, and fall close to the peritectic or the olivine–pyroxene equilibria boundary. These can be explained as partial melts of an O- or C-chondrite-like source. The degree of partial melting from a chondritic precursor varied over a large range, from sufficiently low to incompletely melt feldspar (e.g., <8% for Sombrerete), to sufficiently

high to melt all feldspar and much pyroxene in the source region (e.g., 30% for Miles). The melts then partially crystallized to form crystal – melt mushes that varied in the proportion and identity of crystals and melts between different inclusions. Highly felsic inclusions ("cryptocrystalline", "crystalline felsic", "glassy") present in the fractionated IIEs approach a eutectic composition but have an uncertain origin. Very different are feldspar-poor rocks that probably formed either as cumulates from siliceous melts (the Si-rich orthopyroxenites of the IVA stony irons), or as restites of an equilibrium batch partial melting process (peridotite in Udei Station). Other silicates in the ungrouped irons NWA 468 and Tucson may be partial melt residues.

6. Ages

Radiometric ages of silicate-bearing irons constrain the origin and evolution of the meteorites. Silicates have been dated with short-lived I–Xe and Hf–W chronometers and with long-lived Ar–Ar, K–Ar, Rb–Sr, Sm–Nd, Pb–Pb and U–Pb chronometers. Metallic phases have been dated using the short-lived Pd–Ag (Chen and Wasserburg, 1996; Carlson and Hauri, 2001; Chen et al., 2002; Horan et al., 2012) and Hf–W chronometers and long-lived Re–Os chronometer. Phosphates have been dated using the short-lived Mn–Cr decay scheme (see Goldstein et al., 2009). Troilite has been dated with the Re–Os and Pb–Pb chronometers. Table 6 summarizes data for many of these systems. For consistency, I–Xe and Hf–W ages were recalculated to the same benchmarks, Shallowater (4563.3 Ma old – Gilmour et al., 2006) and CAIs (4568.3 Ma old – Kleine et al., 2009), respectively, and older Rb–Sr ages were recalculated using an updated decay constant for ^{87}Rb ($\lambda_{Rb} = 1.42 \times 10^{-11}$ a^{-1}).

6.1. Discrepant and young ages

Two first order observations can be made regarding the data in Table 6. (1) The Hf–W ages for metal tend to exceed the ages of silicates in the same groups (IAB, IIE). However, the oldest silicate ages overlap the Hf–W metal ages in each group. (2) There are "young" and "old" silicate ages for both the unfractionated and fractionated IIEs using long-lived decay schemes for the silicates (Niemeyer, 1980; Casanova et al., 1995; Mittlefehldt et al., 1998; Bogard et al., 2000). The IIEs with young silicate ages include Kodaikanal (fractionated), Netschaëvo (unfractionated), and Watson (unfractionated). Those with old silicate ages include Colomera (fractionated), Miles (fractionated), Taramuhara (fractionated), Techado (unfractionated), and Weekeroo Station (fractionated). No correlation for the IIEs exists between the degree of differentiation and the age.

The significance of discrepant and young ages can be evaluated by examining individual age data for selected IAB and IIE irons (Fig. 14a and b). For each meteorite, ages are shown top to bottom in rough order of decreasing closure temperature as summarized by Schulz et al. (2009, 2010), and the oldest ages are always given with the Hf–W and I–Xe chronometers, which have the highest closure temperatures. Younger ages are commonly shown with the Sm–Nd, Rb–Sr, K–Ar, and Ar–Ar chronometers. The implication is that the I–Xe and Hf–W ages record initial formation times at higher temperatures, and the younger ages record resetting times at lower temperatures. Resetting appears to have been common in the IAB body (Bogard et al., 2005; Schulz et al., 2009), but it was also prevalent among the IIEs.

In principal, resetting could arise in two ways, by later impact heating events that mainly affected more easily perturbed dating systems with low closure temperatures or by a single, slow cooling process, which allowed minerals with progressively lower closure temperatures to record later closure as cooling occurred. In either case, given that the Hf–W system has a higher closure temperature than most silicate chronometers, metal Hf–W ages will be higher than silicate ages in the IAB and IIE irons. This accounts for the ~37 Ma spread in average metal and silicate ages for the IAB body (Table 6). Considering only the IIEs with "old silicates", the difference between average metal and silicate ages is somewhat larger, ~106–108 Ma. There is therefore a qualitative difference between the IAB and IIE irons, with resetting for the IAB body occurring at significantly earlier times.

Silicate chronometry for the IABs has been discussed in the framework of slow cooling in the IAB parent body. Fig. 14a shows that variations in Ar–Ar plateau ages occur for different plagioclase separates in the IABs (Vogel and Renne, 2008). The data suggest that Ar closure was not attained for feldspar in all samples until ~4.35 Ga ago. The "plag all" datums in Fig. 14a represent the average of all plagioclase size fractions, whereas the "plag hi" and "plag lo" represent fractions with especially high and low ages, respectively. These separates were sorted by grain sizes, but there was no correlation between age and grain size, suggesting that the plagioclase could not all have cooled in the same environment (Vogel and Renne, 2008). Instead, the data were interpreted to indicate that plagioclase from different cooling settings in the parent body were impact-mixed in a major collisional break-up and reassembly event (Vogel and Renne, 2008), following the model of Benedix et al. (2000). The putative impact would have scrambled plagioclase from the deeper, warmer portions with the shallower, cooler portions of the parent body.

In principle, reassembly of the IAB parent body could have occurred while the parent body was warm or cool. If it was cool and not significantly reheated by the impact, all of the variation in Ar ages could be attributed to cooling in the parent body before impact, and this would place the impact at any time after ~4.35 Ga ago. If the IAB body instead was warm and reaccreted warm, age resetting could have occurred after reassembly, and the time of impact would be moved to earlier times. Although the timing of the disruptive impact is not well constrained from the Ar–Ar dates, Vogel and Renne (2008) suggested an impact at ~4.47–4.50 Ga ago, based on assuming that the lowest Caddo County ages were formed by cooling to Ar closure after the impact. Similarly, Bogard et al. (2005) suggested that Ar–Ar dates and metallographic cooling rates for IABs (Herpfer et al., 1994) could be reconciled if post-assembly metamorphism occurred as late as 4.53 Ga ago, placing the time of impact slightly before that. This latter age is close to the most probable Re–Os crystallization age for metal in IABs (4.54 ± 0.02 Ga, see Section 6.3) and also resembles Sm–Nd ages obtained for Caddo County (Fig. 14a). A large impact-scrambling event occurring while metal was partly molten, which mixed material from different levels, appears to be consistent with the age data.

For the three IIEs shown in Fig. 14b, the pattern is somewhat different. Weekeroo Station is representative of an "old silicate" IIE. Unlike for the IABs, there is no systematic change in age with closure temperature. Although Rb–Sr, K–Ar, and Ar–Ar ages overlap within error, the two Rb–Sr ages are generally less than two K–Ar and one Ar–Ar age, despite having a higher closure temperature (Fig. 14b). The reason for this is not clear, but it suggests that the Rb–Sr ages and K–Ar/Ar–Ar systems were perturbed in different ways during late heating so as to give discrepant results. It is possible that this perturbation arose as a result of an impact heating process that was briefer than the type of resetting that could have affected the IAB asteroid.

Watson and Kodaikanal are representative of "young silicate" IIEs. Their Rb–Sr, K–Ar, Ar–Ar and Pb–Pb/U–Pb ages are *much* younger (by ~1 Ga) than Hf–W and I–Xe ages (Fig. 14b). Resetting by late impact heating is the only viable explanation for such young ages, but it did not fully erase old silicate and metal ages. A Re–Os

Table 6
Radiometric ages (Ma) of silicate-bearing iron meteorite groups.[a]

	Mean ± s.d.	Range	N	References
IAB silicate[b,l]	4528 ± 63	4313–4610	36	1–11
IAB metal (Hf–W)[c,m]	4564.7 ± 3.1	4557.8–4570.9	37	6, 12–15, 17
IAB metal (Re–Os)	4537 (21)		1	32
IIE unfractionated silicate, "old"[d]	4550 ± 56	4489–4600	3	13, 19, 21
IIE unfractionated silicate, "young"[e]	3480 ± 290	3040–3790	5	18, 20–22
IIE fractionated silicate, "old"[f]	4448 ± 100	4270–4554	11	11, 18, 21–23, 25, 28–29
IIE fractionated silicate, "young"[g]	3610 ± 150	3350–3740	6	11, 24, 26, 27
IIE metal (Hf–W)[h,n]	4556.3 ± 9.0	4536.4–4564.8	10	12, 13, 15, 17, 22
IVA metal (Hf–W)[i]	4569.3 ± 2.9	4565.0–4577.4	20	12, 13, 16, 17
IVA metal (Re–Os)[j]	4456 (25)		1	31, 32
IVA troilite (Pb–Pb)[k]	4565.3 (0.1), 4544.7 (7)		2	33
Enon silicate, ungrouped	4590 (30)		1	30
Sombrerete silicate, ungrouped	4541 (12)		1	21

References: **1** = Stewart et al. (1996), Caddo County, internal Sm–Nd; **2** = Liu et al. (2002), Caddo County, internal Sm–Nd; **3** = Takeda et al. (2000), Caddo County, Ar–Ar plateau; **4** = Bogard et al. (2005), Caddo County, Campo del Cielo, EET 83333, Udei Station, Ar–Ar and I–Xe plateau; **5** = Vogel and Renne (2008), average plagioclase separates in Caddo County, Campo del Cielo, Landes, Ocotillo, Ar–Ar plateau; **6** = Schulz et al. (2012), Caddo County, Campo del Cielo, Copiapo, Landes, Mundrabilla, San Cristobal, bulk, rock, internal Hf–W; **7** = Podosek (1970), Campo del Cielo bulk I–Xe; **8** = Liu et al. (2003), Campo del Cielo, internal Rb–Sr; **9** = Niemeyer (1979a), Campo del Cielo, Landes, Mundrabilla, Woodbine, bulk I–Xe; **10** = Niemeyer (1979b) Campo del Cielo, Landes, Mundrabilla, Pitts, Woodbine, Ar–Ar plateau and bulk K–Ar; **11** = Bogard et al. (1967), Kodaikanal, Toluca, Weekeroo Station, internal K–Ar; **12** = Qin et al. (2008), Arlington, Bishop Canyon, Bohumilitz, Duchesne, Gibeon, Hill City, Nantan, Surprise Springs, Watson, Wood's Mountain, bulk Hf–W; **13** = Markowski et al. (2006), Caddo County, Canyon Diablo, Cranbourne, Miles, Morasko, Mundrabilla, Seelasgen, Toluca, Watson, all bulk, and alone for Watson, internal Hf–W; **14** = Kleine et al. (2005), Campo del Cielo, Nagy Vazsony, bulk Hf–W; **15** = Schulz et al. (2012), Campo del Cielo, Canyon Diablo, Kodaikanal, Landes, Lueders, Magura, Mundrabilla, Nantan, Zagora, Netschaëvo, bulk Hf–W; **16** = Horan et al. (1998), Bushman Land, Canyon Diablo, Duel Hill, Jamestown, Magura, New Leipzig, Seelasgen, Shrewsberry, Yanhuitlan, rock Hf–W and Re–Os and bulk Hf–W; **17** = Scherstén et al. (2006), Coolac, Cranbourne, Toluca, Weekeroo Station, bulk Hf–W; **18** = Niemeyer (1980), Netschaëvo, Weekeroo Station, Ar–Ar plateau, bulk K–Ar and I–Xe; **19** = Casanova et al. (1995), Techado, bulk K–Ar; **20** = Olsen et al. (1994), Watson, bulk K–Ar; **21** = Bogard et al. (2000), Colomera, Miles, Sombrerete, Watson, Techado, Ar–Ar plateau; **22** = Snyder et al. (2001), Miles, Watson, Weekeroo Station, bulk Hf–W and model Sm–Nd (latter excludes anomalous ~0.7 Ga age for Weekeroo Station); **23** = Sanz et al. (1970), Colomera, internal Rb–Sr; **24** = Burnett and Wasserburg (1967a), Kodaikanal, internal Rb–Sr, $\lambda_{Rb} = 1.42 \times 10^{-11}$ a^{-1}; **25** = Burnett and Wasserburg (1967b), Colomera, Weekeroo Station, internal Rb–Sr, $\lambda_{Rb} = 1.42 \times 10^{-11}$ a^{-1}; **26** = Bogard et al. (1967), Kodaikanal, internal K–Ar and Rb–Sr; **27** = Göpel et al. (1985), Kodaikanal, internal Pb–Pb and U–Pb; **28** = Takeda et al. (2003b), Ar–Ar plateau; **29** = Evensen et al. (1979), Weekeroo Station, bulk Rb–Sr; **30** = Niemeyer (1983), Enon, Ar–Ar plateau. **31** = Smoliar et al. (1996), Re–Os rock isochrons. **32** = Horan et al. (1998), Re–Os rock isochrons. **33** = Blichert-Toft et al. (2010), $^{206}Pb/^{207}Pb$ method for troilite in two irons, lower age (4544.7 Ma) for Gibeon attributed to shock, higher age (4565.3 Ma) for Muonionlusta attributed to original formation.

[a] Ages determined by a variety of techniques (silicates: Sm–Nd, Rb–Sr, K–Ar, Ar–Ar plateau, I–Xe, Hf–W, Pb–Pb and U–Pb; metal: Hf–W and Re–Os). *N* = Number of determinations (different works), s.d. = standard deviation of mean, values in parentheses give error. I–Xe ages calculated relative to Shallowater, taken to be 4563.3 Ma old (Gilmour et al., 2006); Hf–W ages for chondritic system calculated relative to CAIs, taken to be 4568.3 Ma old (Kleine et al., 2009).

[b] Caddo County, Campo del Cielo, Copiapo, EET 83333, Four Corners, Landes, Lueders, Mundrabilla, Ocotillo, Pitts, Toluca, Udei Station, Woodbine.

[c] Bohumilitz, Caddo County, Campo del Cielo, Canyon Diablo, Coolac, Copiapo, Cranbourne, Deport, Landes, Lueders, Magura, Morasko, Mundrabilla, Nagy Vaszony, Nantan, New Leipzig, San Cristobal, Seelasgen, Shrewsberry, Surprise Springs, Toluca, Zagora.

[d] Techado, Watson.

[e] Netschaëvo, Watson (Hf–W).

[f] Colomera, Miles, Taramuhara, Weekeroo Station.

[g] Kodaikanal.

[h] Arlington, Netschaëvo, Kodaikanal, Miles, Watson, Weekeroo Station.

[i] Bishop Canyon, Bristol, Bushman Land, Duel Hill, Gibeon, Hill City, Huizopa, Jamestown, Mantos, Putnam, Steinbach, Yanhuitlan, Wood's Mountain.

[j] Age probably spurious (see text).

[k] Muonionlusta, Gibeon.

[l] Including I–Xe and Hf–W only and excluding outlier 4538 I–Xe age for Udei Station, ages are 4562.2 ± 4.0 Ma, range 4557.5–4569.0 Ma (*N* = 8).

[m] Excluding Mundrabilla (see text), ages are 4565.2 ± 2.5 Ma, range 4561.0–4570.9 Ma (*N* = 33).

[n] Excluding Kodaikanal and Watson (see text), ages are 4562.1 ± 2.4 Ma, range 4558.7–4564.8 Ma (*N* = 6).

age for Kodaikanal metal gives a high age consistent with that of Hf–W, possibly because Re and Os are so siderophile that they cannot be lost from metal once it forms, regardless of later heating events (Birck and Allègre, 1998).

The "young silicate" IIEs, both unfractionated and fractionated, have similar ages (Table 6), and thus could have had ages reset in the same, late impact event. Bogard et al. (2000) suggested that these irons were derived in the same cratering event on the same parent body. Whether or not the other IIEs formed in the same or a different parent body is not clear from age data (Niemeyer, 1980; Bogard et al., 2000). Individual ages for the "young" IIEs range from 3.04 to 3.79 Ga and are based on a variety of chronometers including Ar–Ar plateau, K–Ar, U–Pb, a precise Pb–Pb age (3.676 ± 0.003 Ga – Göpel et al., 1985), a younger Sm–Nd model age (3.04 Ga – Snyder et al., 2001), and older Rb–Sr ages (3.7 Ga – Burnett and Wasserburg, 1967a; 3.74 Ga – Bogard et al., 1969). Excluding the outlier model Sm–Nd age but weighting all others equally, the ages average 3.60 ± 0.15 Ga (mean and standard deviation), although Bogard et al. (2000) suggested the possibility of an impact occurring at the time implied by the Pb–Pb date, 3.676 Ga ago.

That so many chronometers record the same age for the "young silicate" IIEs implies intense heating, involving either partial or complete melting or extensive metamorphism. Watson and Kodaikanal silicate were molten at some point in their evolution, but Netschaëvo silicate appears only to have been metamorphosed (Section 3.2). Thus, intense metamorphism of silicate was sufficient for resetting the ages of Netschaëvo and possibly for the other two meteorites. Reheating for Netschaëvo was sufficiently intense that the I–Xe system was significantly disturbed (Niemeyer, 1980). The deformed Widmanstätten textures of Kodaikanal (Bence and Burnett, 1969) and Watson (Olsen et al., 1994) imply that strong shock affected the irons after the slow cooling event that originally produced the Widmanstätten textures. This could have been the ~3.6 Ga impact event, although Olsen et al. (1994) suggested that for Watson it was the impact at ~8 Ma that started the cosmic ray exposure clock for the iron.

That the "young" IIEs include both unfractionated (Netschaëvo, Watson) and fractionated (Kodaikanal) members that could have been affected by the same impact, suggests the co-existence of these on the same parent body ~3.6 Ga ago. Moreover, cosmic ray exposure ages for these meteorites are not all the same, but

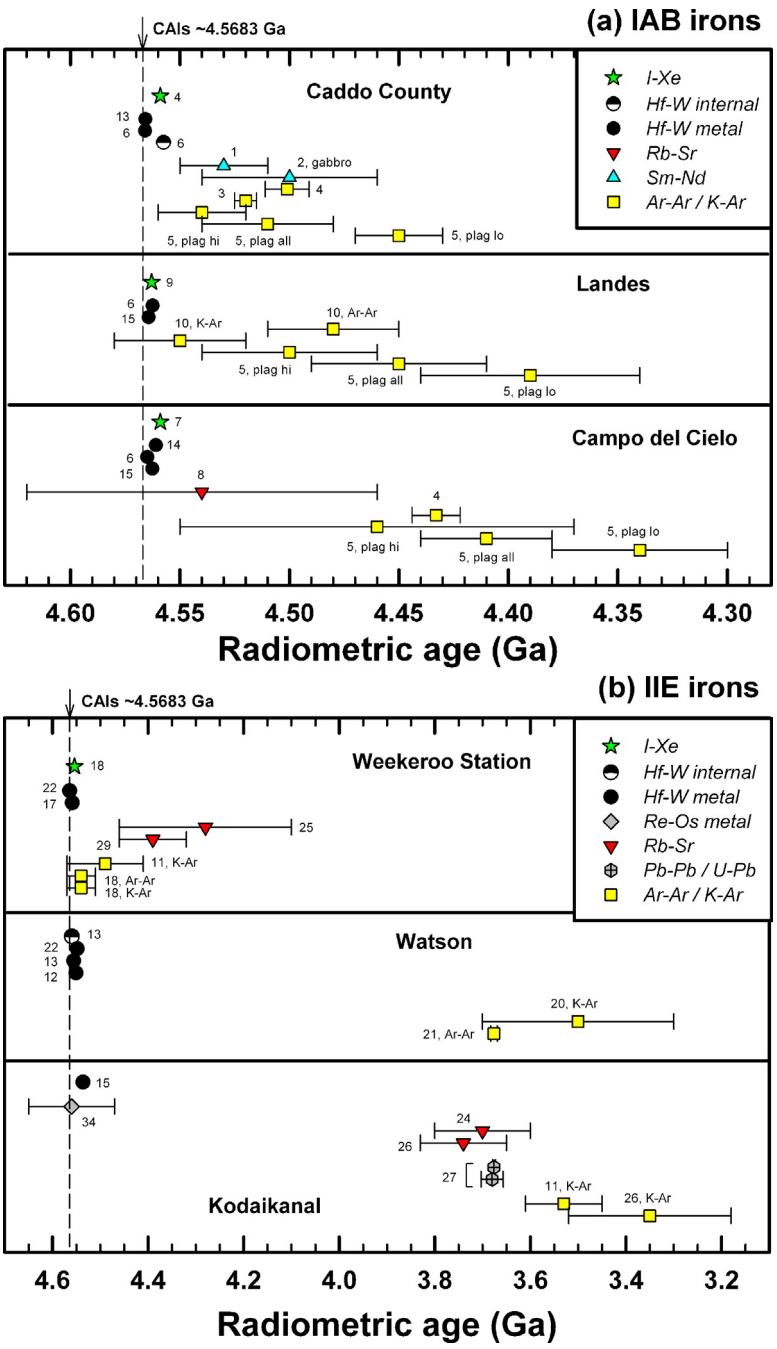

Fig. 14. Summary of radiometric ages for selected (a) IAB irons and (b) IIE irons. Numbers near symbols give references keyed to Table 6, except for reference 34 which is Birck and Allègre (1998). The reference age for CAIs is from Kleine et al. (2009) and is shown by a dashed line.

generally resemble H-group chondrites and are distinctly younger than other IIEs (Bogard et al., 2000). This implies they were derived from meteoroids that were similar in overall size and strength to those ejected from the H chondrite asteroid at about the same time.

However, a different question is whether a late impact event *created* the melt lithologies in Watson and Kodaikanal. Impact melting to create Watson is reasonable, as the silicate shows good evidence for being a melt of an H chondrite-like body, similar in bulk composition to Netschaëvo (Section 5) with which it evidently coexisted. But to create by impact a fractionated assemblage such as Kodaikanal would seem to be more difficult, because the assemblage is not a whole-rock chondrite melt such as one would expect for an impact collision (e.g., Keil et al., 1997), but rather a partial melt.

The question of whether impact melting can create fractionated Kodaikanal-like silicate is important, because if this process can work for Kodaikanal, it can potentially work for all fractionated IIE silicates. The young Rb–Sr age for Kodaikanal is the chief evidence that chemically evolved silicates can be created by impact-induced differentiation (Burnett and Wasserburg, 1967a; Bence and Burnett, 1969; Bogard et al., 2000). The Rb–Sr data for Kodaikanal provide information on the initial $^{87}Sr/^{86}Sr$ isotopic composition at the time the age was set, which is related to the time evolution of Rb/Sr in the source region. The latter can be used to evaluate whether the source region was chondritic or not. According to Burnett and Wasserburg (1967a) and Bence and Burnett (1969), Kodaikanal probably formed by impact-induced differentiation because the source region was essentially chondritic at the late

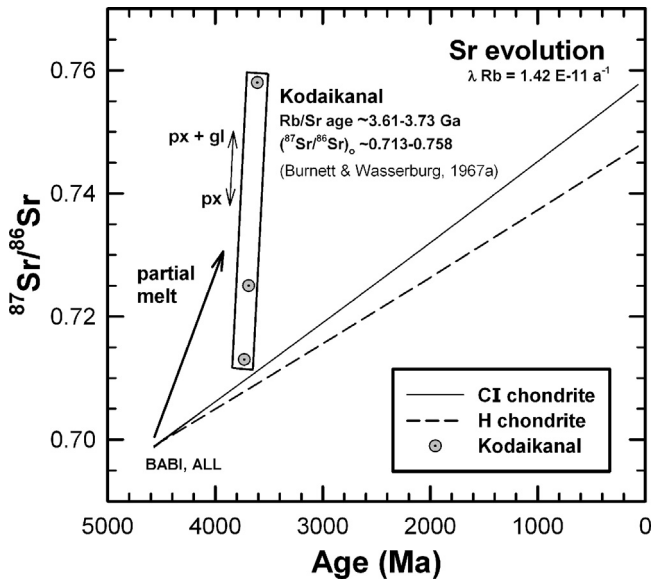

Fig. 15. Strontium evolution diagram showing the evolution of $^{87}Sr/^{86}Sr$ with time for a reservoir with CI chondrite and H chondrite composition (Lodders and Fegley, 1998) and initial Sr isotope composition of BABI (Papanastassiou and Wasserburg, 1969) and ALL (Gray et al., 1973), compared to data for Kodaikanal (Burnett and Wasserburg, 1967a). All data utilize a decay constant $\lambda_{Rb} = 1.42 \times 10^{-11}\ a^{-1}$ (McSween and Huss, 2010). The growth curves for BABI and ALL are indistinguishable on this scale. Kodaikanal points are for different fractions including various proportions of pyroxene (px) and glass (gl), with the proportion of pyroxene increasing to the bottom.

date recorded by the silicate. The proposition of impact-induced differentiation to form Kodaikanal is re-evaluated in Fig. 15. The Sr growth curves for two chondrite compositions are shown, as well as data for Kodaikanal, which are presented in a band with different initial $^{87}Sr/^{86}Sr$ values because the isochron is not a perfect line. The CI chondrite growth curve is enriched in Rb/Sr so it evolves to higher $^{87}Sr/^{86}Sr$ values faster, and is likely to be an upper limit on $^{87}Sr/^{86}Sr$ for chondrite, whereas the H chondrite growth curve is more plausible for Kodaikanal. The overall Kodaikanal isochron, fit through all pyroxene and glass points, gives the highest initial $^{87}Sr/^{86}Sr$ value, whereas progressively more pyroxene-rich fractions give lower initial ratios. Fig. 15 shows that Sr-isotope growth curves for chondrite compositions do not pass through the Kodaikanal data. Regardless of which growth curve, or which portion of the Kodaikanal isochron (or which initial Sr composition, BABI or ALL) one uses, Fig. 15 implies that the source region for Kodaikanal was enriched in $^{87}Sr/^{86}Sr$ at the time the Rb–Sr ages were set. This is what one would expect if Kodaikanal formed as a partial melt at an earlier time, and was reheated ~3.6–3.7 Ga ago. The earlier the differentiation occurred, the easier the elevated $^{87}Sr/^{86}Sr$ values for Kodaikanal silicates can be explained. Thus, Kodaikanal probably differentiated well before 3.6–3.7 Ga ago, most likely at the times implied by the old Hf–W and Re–Os metal ages (~4.50–4.55 Ga) for the meteorite. The Rb–Sr data for Kodaikanal do not support the hypothesis of impact-induced differentiation.

6.2. Hf–W chronometry

Among the various decay systems that can provide high-precision ages, Hf–W has been the most widely applied to irons and provides a detailed record for metal–silicate separation and heating events. The data suggest that (1) there are age differences between the fractionally crystallized and IAB and IIE groups, and (2) there are differences within the IAB and IIE groups that reflect either different datable events or late-homogenization events. Together the data can be used to evaluate the nature of the heat sources that affected silicate-bearing irons (Scherstén et al., 2006; Qin et al., 2008; Schulz et al., 2009, 2012).

There is a resolvable difference in the W isotope composition of metal in IAB and IIE irons and in fractional irons, and although prolonged cosmic ray exposure can affect W-isotope compositions, it cannot explain most of this difference (Kleine et al., 2005, 2009; Markowski et al., 2006; Scherstén et al., 2006; Qin et al., 2008). The simplest interpretation is that isotopic variations reflect age differences, or more properly, metal–silicate separation ages from a chondritic precursor. Thus, metal from the IVAs yield old ages essentially indistinguishable from CAIs, as is true for other fractional irons, but metal from the IAB and IIE groups is progressively younger (Table 6). Taken at face value, the averaged data imply that metal–silicate separation on the IVA body took place 1 ± 2.9 Ma *before* CAIs (i.e., not distinguishable from CAIs), on the IAB body 3.6 ± 3.1 Ma *after* CAIs, and on the IIE body, 12 ± 9.0 Ma *after* CAIs. A better understanding of neutron capture effects led Kruijer et al. (2013) to suggest a Hf–W age of 1.6 ± 1.0 Ma post-CAIs (4566.7 ± 1.0 Ma) for the IVAs. This is similar to a precise $^{207}Pb/^{206}Pb$ age for troilite in IVA Muonionalusta of 4565.3 ± 0.1 (Blichert-Toft et al., 2010). Regardless, the apparently later metal–silicate separation for the IABs and IIEs has been attributed to a slightly later accretion time for the IAB and IIE groups, when the main driver for internal heating, radioactive ^{26}Al, would have significantly decayed (e.g., Kleine et al., 2005, 2009; Markowski et al., 2006; Wadhwa et al., 2006; Qin et al., 2008).

The averaged ages for IABs include some outliers that could have been affected by resetting in either earlier or later impact heating events, and do not fully take into account cosmic ray exposure effects. Refined estimates of IAB metal ages were presented by Schulz et al. (2012) from correlations between W-isotope compositions and cosmic ray exposure ages. It was suggested that Mundrabilla was reset by an impact-melting event ~13 Ma after CAIs, consistent with metal–troilite intergrowth textures suggestive of unusually fast cooling (~6 °C/yr) during crystallization (Scott, 1982). Metal in Caddo County gives evidence for earlier metal–silicate separation, at $0.86 + 0.93/-0.86$ Ma after CAIs (Schulz et al., 2012). Caddo County is classified as an ungrouped member of the IAB complex, as is true also for Mundrabilla (Wasson and Kallemeyn, 2002), meaning that these have outlier metal compositions. Excluding Mundrabilla and Caddo County, Schulz et al. (2012) suggested that metal segregation in the IAB parent body occurred mainly within a well-defined period of $5.06 + 0.42/-0.41$ Ma after CAIs. This age is similar to that inferred for winonaites (Schulz et al., 2012). That IAB ages of ~5 Ma after CAIs are so widespread, and early, is consistent with metal–silicate differentiation occurring by internal heating processes driven by ^{26}Al decay in the IAB – winonaite parent body (Qin et al., 2008; Schulz et al., 2009, 2012).

For metal from IIEs, chronology inferences are less clear. Qin et al. (2008) noticed a large difference in W-isotope composition for metal in silicate-free Arlington and silicate-bearing Watson, and suggested that isotopic exchange between metal and silicate during late thermal events could have occurred for the silicate-bearing irons, which prevent chronologic interpretation. Scherstén et al. (2006) noted that Watson metal has unusually radiogenic W and suggested that it formed by impact melting and re-equilibration of the silicate and metal fractions.

Schulz et al. (2012) found that of six IIE irons analyzed, three (Netschaëvo, Watson, Kodaikanal) have negligible cosmic ray exposure but three different $\varepsilon^{182}W$ values, implying metal–silicate separation at three different times (~3, ~13, and ~28 Ma after CAIs, respectively). However, there is reason to question the validity of the 13 and 28 Ma IIE events. Metal in Watson and Kodaikanal have the most radiogenic metal (least negative $\varepsilon^{182}W$ values) of any of

the IIEs. In these meteorites, metal was extensively deformed during a strong shock event, with disruption, shearing, and granulation of Widmanstätten patterns, and even localized melting (Bence and Burnett, 1969; Buchwald, 1975; Olsen et al., 1994). Regardless of when or how the metal originally formed, there was likely partial W isotope re-equilibration between metal and silicate during the event that created strong metal shock effects, so the relatively high ε^{182}W for Watson and Kodaikanal probably do not in themselves provide valid metal–silicate fractionation dates.

Omitting Watson and Kodaikanal, the average Hf–W metal age for the IIEs would be 4562.1 ± 2.4 Ma, or 6.2 ± 2.4 Ma after CAIs (Table 6). These ages might be slightly biased to older values given that cosmic ray exposure effects are not included, but they overlap with, and are only slightly younger than, the Hf–W ages for IABs.

Besides model ages for metal, Hf–W can be used to determine ages of silicates using internal isochrons. Schulz et al. (2009) analyzed silicate and metal separates from IABs. They identified apparent silicate differentiation ages and later re-equilibration events within an early time frame. Of three high-clinopyroxene (basaltic) inclusions in Caddo Country, two defined a linear host metal–silicate trend which was interpreted as an isochron, indicative of a partial melting event occurring 4.6 + 0.7/−0.6 Ma after CAIs. However, this is younger than the ~0.86 Ma (zero cosmic ray exposure) age for metal–silicate separation inferred for Caddo County (Schulz et al., 2012), so it is possible that the apparent 4.6 Ma post-CAI age reflects later equilibration. Several inclusions from Landes, Copiapo, and Campo del Cielo form a linear trend on an isochron diagram interpreted as reflecting silicate differentiation 2.5 + 2.3/−2.0 Ma after CAIs (Schulz et al., 2012). This may be slightly older than the preferred global IAB metal–silicate fractionation age of 5.06 + 0.42/−0.41 Ma after CAIs inferred by Schulz et al. (2012), but the error bars overlap. If this age difference is real it could indicate that magmatic activity preceeded the global metal–silicate separation event. Other silicates in Campo del Cielo (El Taco) were interpreted as having been homogenized at 10 + 2.4/−2.0 Ma after CAIs, and Lueders showed evidence for complete re-equilibration of silicate by metal. These events could have been caused by relatively late impact reheating (Schulz et al., 2009).

Whether or not the Hf–W ages for metal or silicate have a fully consistent chronology with I–Xe ages for silicate in the IABs is not clear. For example, among four irons, Niemeyer (1979a) found a ~6 Ma spread in I–Xe ages in the sequence Woodbine (early), Mundrabilla, Copiapo, and Landes (late). Different silicate inclusions in Landes and Copiapo appear to have different Hf–W ages (Schulz et al., 2009), making the comparison with I–Xe difficult. Comparing relative I–Xe ages for silicate (Niemeyer, 1979a) with relative (non-exposure-corrected) Hf–W metal ages (Schulz et al., 2009, 2012; Markowski et al., 2006), Copiapo and Landes are consistent, but Mundrabilla is inconsistent as it has a late Hf–W age and an earlier I–Xe age. (No Hf–W dates are available for Woodbine.)

Whether or not the Hf–W and I–Xe silicate ages for particular IABs are always consistent, the two high-temperature chronometers both suggest early melting of the IAB body. Excluding one anomalously young I–Xe age for Udei Station (Bogard et al., 2005), the overall average ages with the Hf–W and I–Xe chronometers are similar, 3.6 ± 3.1 Ma and 6.1 ± 4.0 Ma after CAIs, respectively. This gives a combined high-temperature closure age of 4562.2 ± 4.0 Ma for IAB silicate.

6.3. Re–Os chronometry: late crystallization?

Re–Os ages for metal date the time of metal crystallization (e.g., Shirey and Walker, 1998; Horan et al., 1998), as opposed to Hf–W ages, which date metal–silicate separation (e.g., Horan et al., 1998; Kleine et al., 2009). Assuming an absolute age of 4558 Ma for the IIIAs, Smoliar et al. (1996) found crystallization ages for fractionally crystallized iron groups of 4537 ± 8 Ma for IIA, 4527 ± 29 for IVB, and 4456 ± 29 for IVA, and Horan et al. (1998) determined a Re–Os crystallization age of 4537 ± 21 Ma for the IABs (Horan et al., 1998). These are tens to hundreds of Ma after metal–silicate separation, with the IVAs anomalously young. However, the assumed reference age for IIIABs of 4558 Ma may be too young, as Mn–Cr ages for phosphate are 3 ± 4 Ma after CAIs (Goldstein et al., 2009). Moreover, the anomalous age for IVA metal is probably spurious. A late Re–Os age for IVAs is at variance with evidence for early closure ages based on the ^{182}Hf–^{182}W system (Table 6) and the ^{107}Pd–^{107}Ag system (Chen and Wasserburg, 1996), and with Pb–Pb dates of 4562 ± 0.1 Ma for troilite from Muonionalusta and 4544 ± 7 Ma for troilite in Gibeon, the latter age attributed to shock (Blichert-Toft et al., 2010). In addition, apparently young Re–Os ages for IVA irons (Smoliar et al., 1996) conflict with apparently old Re–Os ages obtained by others (Shen et al., 1996).

6.4. Ages – summary

Different ages for the silicate-bearing irons are obtained with different chronometers, and this probably reflects various susceptibilities to resetting in later thermal events. Hf–W ages for metal and I–Xe ages for silicates mainly record the earliest high-temperature events. Metal–silicate fractionation in the IVA body occurred at about the same time as the formation of CAIs, and within 10 Ma later for both the IAB and IIE parent bodies. Relatively consistent early Hf–W dates (~5 Ma after CAIs) for IAB irons suggest that metal–silicate separation could have occurred in a body that was being internally heated by ^{26}Al decay. The situation is less clear for the IIEs. Available evidence indicates that silicate differentiation in irons occurred early, around the time of metal–silicate fractionation. Silicate chronometers mainly record later ages, caused either by later impacts or by slow cooling in a large parent body. In the IABs, there is evidence that slow cooling in a large parent body was partly responsible for resetting. Early scrambling of the IAB body during a major collision is consistent with variable ages of plagioclase separates within the same iron meteorite. For the IIE irons, younger ages may be the result mainly of impact heating events. Later impact reheating was clearly responsible for an event that affected the IIE parent body 3.60 ± 0.15 Ga ago, which reset most silicate chronometers in the Watson (unfractionated IIE), Netschaëvo (unfractionated IIE), and Kodaikanal (fractionated IIE) “young silicate” iron meteorites. The data suggest, but do not prove, that all three meteorites were derived from the same parent body in the same impact event, which would indicate that both unfractionated and fractionated IIEs were present in close proximity together. Kodaikanal was probably not differentiated at this time, but rather formed as a partial melt at an earlier time and was significantly reheated in the late impact event.

7. Thermal histories

The thermal histories of silicate-bearing irons have been constrained by radiometric dating (Section 6) and geothermometry and geospeedometry (quantitative cooling rate models).

7.1. Geothermometry

Table 7 presents a compilation of geothermometry results for silicates in iron meteorites. These include older applications of pyroxene geothermometry based on the Ca–Mg solvus for clinopyroxene (Bence and Burnett, 1969; Bunch et al., 1970), more modern applications of two- or three-pyroxene geothermometry in multicomponent systems (Olsen et al., 1994; Ruzicka et al., 1999; Benedix et al., 2005; Ruzicka and Hutson, 2010), older (Bunch et al., 1970) and more recent formulations of olivine–chromite

Table 7
Geothermometry results for silicates in iron meteorites.[a]

Group	Meteorite	Method/system	T_c (°C)	Reference
IAB	Odessa	Ca–Mg, cpx	1125	BB69
IAB	Campo del Cielo	Ca–Mg, cpx	1000	BB69
IAB	Four Corners	Ca–Mg, cpx	950	BB69
IAB	6 meteorites[b]	ol-chr	1335–1154	Bu70
IAB	6 meteorites[b]	Ca–Mg, cpx	1030–900	Bu70
IAB	Landes	ol-cpx, Sc	≤1000	LLP87
IAB	5 meteorites[c]	ol-chr	700–590	Ben05
IAB	5 meteorites[c]	2 px	1200–900	Ben05
IAB	Udei Station	2 px, diop	1148 ± 36	RH10
IAB	Udei Station	2 px, opx	958 ± 46	RH10
IIE unfr	Netschaëvo	ol-chr	894 ± 100	Bu70
IIE unfr	Netschaëvo	Ca–Mg, cpx	870	Bu70
IIE unfr	Watson	ol-chr	1100	O94
IIE unfr	Watson	2 px	1100	O94
IIE fr	Kodaikanal	Ca–Mg, cpx	1100	BB69
IIE fr	Weekeroo Station	3 px, pig	1250–1100	R99
IIE fr	Weekeroo Station	3 px, coarse opx core	1080 ± 30	R99
IIE fr	Weekeroo Station	3 px, aug	1120–975	R99
IIE fr	Weekeroo Station	3 px, opx	925–750	R99
IIE fr	Weekeroo Station	3 px, coarse opx rim	800	R99
IIE fr	Miles	2 px, augite	1168 ± 31	RH10
IIE fr	Miles	2 px, opx	967 ± 95	RH10
Ungr	Enon	ol-chr	1293 ± 100	Bu70

[a] Abbreviations and sources: T_c = closure temperature, IIE unfr = IIE unfractionated, IIE fr = IIE fractionated, Ungr = ungrouped, px = pyroxene, ol = olivine, chr = chromite, cpx = Ca-pyroxene, diop = diopside, pig = pigeonite, aug = augite, opx = orthopyroxene. BB69 = Bence and Burnett (1969), Ben05 = Benedix et al. (2005), Bu70 = Bunch et al. (1970), LLP87 = Luzius-Lange and Palme (1987), O94 = Olsen et al. (1994), R99 = Ruzicka et al. (1999), RH10 = Ruzicka and Hutson (2010).
[b] 6 meteorites include Campo del Cielo, Copiapo, Linwood, Odessa, Toluca, Udei Station.
[c] 5 meteorites include Caddo County, Campo del Cielo, Copiapo, Leuders, Udei Station.

equilibria (Olsen et al., 1994; Benedix et al., 2005), and Sc partitioning between clinopyroxene and olivine (Luzius-Lange and Palme, 1987).

Closure temperatures for silicates suggest a combination of igneous and metamorphic conditions in the IAB, IIE unfractionated, and IIE fractionated groups. The unfractionated IIEs give closure temperatures (T_c) that one might expect based on their textures (Section 3.2), with Netschaëvo equilibrating under metamorphic conditions ($T_c \sim 870$–900 °C), and Watson under igneous conditions ($T_c \sim 1100$ °C) (Table 7).

The fractionated IIE irons present a more complicated story. Pyroxene grains in Kodaikanal, Weekeroo Station, and Miles show evidence for formation at high (melt) temperatures but also appear to be recording subsolidus cooling in some circumstances. Weekeroo Station contains augite, orthopyroxene, and uninverted pigeonite that show this effect (Ruzicka et al., 1999). Pyroxenes in Weekeroo Station that equilibrated under igneous conditions include pigeonite, some augite grains, and the core of an unusually large, apparently brecciated, and possibly xenocrystic orthopyroxene grain. These have $T_c \sim 1080$–1250 °C (Table 7). In contrast, the rim of the coarse pyroxene formed under distinctly metamorphic conditions ($T_c \sim 800$ °C), as did other orthopyroxene grains ($T_c \sim 725$–925 °C) and some augite grains. The lower-temperature pyroxenes show evidence for FeO-reduction during subsolidus cooling (Ruzicka et al., 1999). Subsolidus FeO reduction (~650–1000 °C) has also been inferred for IABs (Seckendorff et al., 1992). Orthopyroxene closure temperatures are lower than for coexisting high-Ca pyroxene in both Wekeroo Station and Miles, suggesting higher diffusivities in the former phase.

Temperatures of the IABs cover a similar range as in the fractionated IIEs (Table 7). One of the best-determined high temperatures is for diopside in Udei Station basalt (Ruzicka and Hutson, 2010), which has $T_c \sim 1168 \pm 31$ °C, suggesting equilibration under igneous conditions. Most other temperatures in IABs range down to ~590 °C. Exceptions are anomalously high and probably wrong temperatures (1154–1335 °C) obtained with an older formulation of the olivine–chromite geothermometer, which disagrees with more modern determinations (590–700 °C). Benedix et al. (2005) noted that apparent two-pyroxene and olivine–chromite temperatures in five IABs were highly variable in different samples, and even within thin sections. They explained this as the result of impact-mixing following catastrophic destruction and reassembly of the parent body. If this is correct, the data imply (1) relatively quick cooling during break-up and the early stages of re-accretion, to avoid re-setting closure temperatures in a given meteorite, and (2) intimate mixing of components that had cooled under various conditions. Ruzicka et al. (1999) also commented on the variability of geothermometry values obtained for Weekeroo Station and suggested that silicates were cooled quickly from high temperatures.

7.2. Cooling rates

Cooling rate data in Table 8, including much obtained by metallographic techniques, are arranged by meteorite group and (to the extent possible) by progressively lower temperature entries within each group. Metallographic techniques include: (1) “kamacite bandwidth”, which involves measuring the width and FeNi zoning patterns across kamacite lamellae in the Widmanstätten pattern; the method as typically applied is simplified to obtain a rapid determination of cooling rate by measuring only lamellae widths and bulk Ni content (Goldstein and Short, 1967); (2) “central-Ni/taenite-width”, which involves measuring the widths and central Ni content of zoned taenite lamellae in the Widmanstätten pattern; a variant of this technique can also be applied to isolated, zoned taenite grains (Herpfer et al., 1994); and (3) “kamacite growth method”, a variant of the kamacite bandwidth method, which models the thickness and growth of kamacite ribbons or spindles in Ni-rich metal (Miyake and Goldstein, 1974). More complex variations of these methods have been presented, such as that of Yang et al. (2008), which is essentially a central-Ni/central-Ni method but one that also involves profile matching across kamacite and taenite lamellae. The metallographic data in Table 8 are of various quality. Older determinations are suspect in part because of outdated diffusion rate data (Rasmussen, 1989; Herpfer et al., 1994); Dean and Goldstein (1986) presented new determinations of Fe–Ni interdiffusion at low temperatures

Table 8
Cooling rates estimated for silicate-bearing iron meteorites.[a]

Group	Meteorite	Cooling rate (°C/Ma)	T (°C)	Method	Reference
IAB	Campo del Cielo	≥100	1500–1200	Xe release, px & feld	MB95
IAB	14 meteorites	(1–3)		Kam bandwidth	GS67
IAB	8 meteorites[b]	63–650	780–580	Kam bandwidth	Ras89
IAB	Toluca, Odessa	0.5–3.7	630–430	Central Ni/tae width	Ras89
IAB	6 meteorites[c]	30–70		Central Ni/tae width	Herp94
IAB	Caddo County	2–20	400–200	Ar release pattern	T00
IAB	Landes, Copiapo, Toluca	~1–8	350–30	Fission track annealing	Benk79/84
IIICD	Carlton	170	780–580	Kam bandwidth	Ras89
IIICD	11 other meteorites[b]	96–480	780–580	Kam bandwidth	Ras89
IIICD	Carlton	2.9	630–430	Central Ni/tae width	Ras89
IIE unfr	Netschaëvo	(1.4)		Kam bandwidth	SW76
IIE unfr	Netschaëvo	~3		Central Ni/tae width	Rb90
IIE unfr	Techado	50–100		Central Ni/tae width	Cas95
IIE fr	Weekeroo Station	≥2.5 °C/h	1000–850	Glass presence	R99
IIE fr	Weekeroo Station	(1.1)		Kam bandwidth	SW76
IIE fr	Kodaikanal	(100–1000)	600–400	Kam bandwidth	BB69
IIE fr	Kodaikanal	(400)		Kam bandwidth	SW76
IVA	Steinbach	>100 °C/h	~1200	Clinobronzite microstructure	Ha96
IVA	Steinbach	976	984 ± 17	Oxygen isotope closure	W04
IVA	Steinbach	150		Central Ni/tae width	Y08
IVA	Steinbach	19	<805	Central Ni/tae width	Ras95
IVA	Steinbach	(5–20)	700–500	Kam bandwidth	Re74
IVA	Steinbach	2200–40,300	470–430	Cation ordering, opx	GaS00
IVA	São João Nepomeceno	1945	1022 ± 62	Oxygen isotope closure	W04
IVA	São João Nepomeceno	23	811 ± 30	Oxygen isotope closure	W04
IVA	São João Nepomeceno	890	<737	Central Ni/tae width	Ras95
IVA	São João Nepomeceno	200–560	400	Cation ordering, opx	GaS00
IVA	20 meteorites	(7–90)		Kam bandwidth	GS67
IVA	8 meteorites	3–65		Central Ni/tae width	MoG78
IVA	6 meteorites	13–25		Central Ni/tae width	WW78
IVA	8 meteorites	2–96	630–430	Central Ni/tae width	Ras82
IVA	14 meteorites, not Stb/SjN	28–3400	<742	Central Ni/tae width	Ras95
IVA	13 meteorites, not Stb	100–6600		Central Ni/tae width	Y08
Ungr	Tucson	1000	650–500	Kam growth	MiG74

[a] Abbreviations as in Table 7 and also: T = temperature, kam = kamacite, tae = taenite, feld = feldspar, Stb = Steinbach, SjN = São João Nepomeceno. Values in parentheses probably less accurate owing to the use of older, less reliable diffusion coefficients.

[b] Excludes Persimmon Creek from IAB as it has an outlier cooling rate and is grouped with IIICD (Wasson and Kallemeyn, 2002). Hassi-Jekna is removed from IIICD and added to IAB based on metal composition (Wasson and Kallemeyn, 2002).

[c] Excludes San Cristobal (poorly determined). References: Benk79/84 = Benkheiri et al. (1979) and Benkheiri (1984), corrected with updated etching efficiencies (Herpfer et al., 1994; Bogard et al., 2000); Cas85 = Casanova et al. (1995), both taenite lamellae and grains; GS67 = Goldstein and Short (1967); GaS00 = Ganguly and Stimpfl (2000); Ha96 = Haack et al. (1996); Herp94 = Herpfer et al. (1994), both taenite lamellae and grains; MB = Mathew and Begemann (1995); MiG74 = Miyake and Goldstein (1974); MoG78 = Moren and Goldstein (1978); Ras82 = Rasmussen (1982); Ras89 = Rasmussen; Ras95 = Rasmussen et al. (1995); Re74 = Reid et al. (1974); Rb90 = Rubin (1990); R99 = Ruzicka et al. (1999); SW76 = Scott and Wasson (1976); T00 = Takeda et al. (2000); WW78 = Willis & Wasson (1978); W04 = Wang et al. (2004); Y08 = Yang et al. (2008).

relevant for iron meteorites. Suspect values are shown in Table 8 with parentheses and tend to give lower cooling rates than more recent determinations. Saikumar and Goldstein (1988) and Herpfer et al. (1994) suggested that the kamacite bandwidth method (or at least simplified versions of it that do not include profile matching), are flawed, because it does not properly account for impingement effects.

IABs cooled very slowly at low temperatures, ~0.5–70 °C/Ma based on the central-Ni/taenite-width method (Table 8). Taenite lamellae in metal-rich areas and grains within silicate-rich areas give the same results, strongly suggesting that much of the IAB body cooled very slowly at low temperatures (Herpfer et al., 1994). This method is mainly sensitive to temperatures of ~430–630 °C (Rasmussen, 1989). Somewhat faster rates were determined with the kamacite bandwidth method, ~63–650 °C/Ma. The difference between the bandwidth and taenite width methods was attributed to a real change in cooling rate at different temperatures by Rasmussen (1989), who noted that the bandwidth method is sensitive to slightly higher temperatures (~580–780 °C). Apparently, the cooling rate of the IAB parent body slowed as temperature decreased because it was continuing to accrete insulating materials as it cooled (Rasmussen, 1989). This idea is supported by even slower cooling rates (~1–20 °C/Ma) at the lowest temperatures (~30–400 °C), as inferred from fission track and Ar release studies (Table 8).

At the opposite extreme, there is some indication of faster cooling (≥100 °C/Ma) at the highest temperatures experienced by Campo del Cielo, based on Xe release studies. Mathew and Begemann (1995) found evidence for differential release of ^{129}I-decay-correlated ^{129}Xe from feldspar, pyroxene, and olivine separates in high-temperature (1200–1500 °C) extractions and suggested that this was related to a difference in closure temperature between feldspar and the ferromagnesian minerals. Assuming a 300 °C lower closure temperature for ^{129}Xe in feldspar compared to pyroxene, Mathew and Begemann (1995) suggested that a cooling rate of ≥100 °C/Ma between 1500–1200 °C could account for the data. However, it is unlikely that the rock reached a temperature as high as 1500 °C, as this would have resulted in significant silicate melting. A maximum temperature of ~1200 °C is possible in light of results for Udei Station and Caddo County, which contain basaltic materials that could have formed at close to this temperature (Ruzicka and Hutson, 2010). Thus, it is not clear that the 100 °C/Ma cooling rate at high temperature (>1200 °C) inferred by Mathew and Begemann (1995) is valid.

For the IIICDs, cooling rates appear to be generally similar to those of the IABs, ranging from 96 to 480 °C/Ma, based on bandwidth method of Rasmussen (1989), which is similar to the range of 63-650 °C/Ma obtained for the IABs (Table 8). Rasmussen (1989) suggested a lower average cooling rate for IIICDs than IABs, but the data overlap greatly, and the exact average depends on

uncertain group assignments and cooling rate outliers. Thus, there is no convincing evidence for a difference in cooling rates for these two groups.

Herpfer et al. (1994) suggested that cooling rates in the IABs are correlated with Ni content of the host metal. Thus, Landes and Copiapo have ~7 wt% Ni with a cooling rate of ~30 °C/Ma; Four Corners and Woodbine have ~9 and 10 wt% Ni with cooling rates of ~40 and ~50 °C/Ma, respectively, and Pitts and Persimmon Creek (IIIC) with ~13 and ~14% Ni, have cooling rates of ~60 and ~70 °C/Ma respectively (Ni contents from Wasson and Kallemeyn, 2002). This correlation, if real, implies that progressively deeper portions of the IAB body concentrated a solid metal fraction (Herpfer et al., 1994).

Metallographic cooling rates for the IIEs are ~1 °C/Ma for Netschaëvo and Weekeroo Station based on kamacite bandwidth, and ~3–100 °C/Ma for Netschaëvo and Techado based on the central Ni/taenite width method. Kodaikanal has a distinctly higher cooling rate (~100–1000 °C/Ma). These high rates for Kodaikanal are for areas of the meteorite that are less shock-deformed and that appear to preserve some of the original Widmanstätten texture (Bence and Burnett, 1969).

The most striking feature of the cooling history of the fractionated IIE group is the seemingly contradictory evidence for rapid cooling in the silicates at moderately high temperatures (close to the silicate solidus) and for slow cooling in the metal at lower temperatures. In some areas the silicates have spherulitic and cryptocrystalline textures (Section 3.2), which almost certainly indicate rapid solidification from just above the silicate solidus. To preserve variable pyroxene closure temperatures in adjacent inclusions from Weekeroo Station, cooling must have been relatively rapid, so as to prevent the resetting of the closure temperatures to a lower, common value (Section 7.1). Moreover, the very existence of partly molten silicate within partly molten metal, as inferred for the fractionated IIEs (Section 3.2), indicates that cooling must have been rapid after metal–silicate mixing, to prevent the gravitational separation of these materials (Section 8).

The only published quantitative cooling rate estimate for the silicates in fractionated IIEs is based on the presence of glass, which has a composition similar to that of tektites. Annealing experiments show that dry glass of this composition is susceptible to devitrification between ~850 and 1000 °C, but does not devitrify below ~850 °C (Ruzicka et al., 1999). Given that glass is not devitrified in some inclusions, this suggests a cooling rate of ≥2.5 °C/h to preserve glass in the 850–1000 °C/h temperature interval (Table 8). As similar glass is present in all fractionated IIEs, this cooling rate is valid for all. Such a cooling rate is a factor of 10^8–10^{10} faster than implied by the metallographic cooling rates for IIEs.

Although glass is the main evidence for rapid cooling of the silicate, small patches of a striated low-Ca pyroxene typical for an intergrowth between orthopyroxene and clinobronzite were recently discovered in Miles (Fig. 3g). This has irregular edges and occurs mainly in the core of clear pyroxene, as often found in the IVA stony irons (Fig. 4c, d). If this clinobronzite formed similarly to that in Steinbach, it would imply a cooling rate of >100 °C/h from above the solidus (see below), which is consistent with the evidence from glass preservation.

Evidently there was a major change in cooling environment for the fractionated IIEs. The silicates cooled rapidly from above the silicate solidus down to at least ~850 °C, which created quenched glass and prevented complete metal–silicate separation. However, cooling was not too rapid to prevent partial resetting of pyroxene closure temperatures, and not too rapid to prevent subsolidus FeO reduction reactions to proceed (Section 7.1). For temperatures much below ~850–700 °C, cooling rates slowed dramatically.

It is important to note that although cooling for the IIEs was rapid just below the silicate solidus, there is no evidence that it was rapid at higher temperatures. The silicates contain coarse phenocrysts that apparently formed in a slow-cooling environment (see also Section 8). Quenching occurred from moderately high temperatures just above the silicate solidus. Metal was probably partly molten during the quenching process (Section 8).

The only way to account for the cooling rate data is for the IIEs to have been close to a cooling surface at moderately high temperatures, but far from one at lower temperatures. Progressive burial after a rapid cooling event is needed. One possibility is temporary excavation of hot materials by impact and subsequent burial below a deep regolith. Another is the re-accretion of hot materials that were temporarily dispersed into space by impact disruption of an asteroidal parent body (Keil et al., 1994). Haack et al. (1996) presented cooling rate curves for a metallic body at 1000 °C in cold free space at −70 °C or at 565 °C, corresponding to space with sunlight and dust in the asteroid belt, respectively. For a cooling rate of 2.5 °C/h, the cooling curves indicate cooling depths >1 m from a free surface, but probably not more than tens of meters from such a surface. Thus, the fractionated IIEs could have existed at high temperatures (~850–1000 °C) as meteoroids that were ~10 m in diameter. At low temperatures (<700 °C), the small bodies evidently would have had to accrete into a much larger one. Exactly how big depends on the conditions assumed.

The IIE, IAB, and IIICD irons all appear to have similar cooling rates, which is ~1–100 °C/Ma based on the taenite width method (Table 8) (Rasmussen, 1989; Herpfer et al., 1994; Casanova et al., 1995). Thus, the following discussion is valid for all these irons. It is assumed that slow cooling occurred with metal embedded in parent bodies that contained a significant amount of silicate. Miyake and Goldstein (1974) found that the center of a silicate-rich body with radius 15 km containing metal would cool at ~1000 °C/Ma, suggesting a much larger cooling body for the sources of the iron meteorites, as their cooling rates are much lower. On the other hand, a silicate-rich body with radius 200 km would be nearly isothermal at depths $r/a < 0.7$ (where "r" = distance from center and "a" = radius) and would cool at ~1–2 °C/Ma, whereas closer to the surface ($r/a = 0.9$) it would cool at ~10 °C/Ma (Goldstein and Short, 1967). As these values of cooling rate are on the low end of what is inferred for the irons, one can surmise that their parent bodies could have been smaller than 200 km in radius if the irons did not form very close to the surface of a much larger body.

For the fractionated IIEs, then, the data are consistent with accretion of metal with silicate into one or more secondary bodies that were ≫15 km and <200 km in radius. The iron meteorite source regions are envisioned as metal-rich pods that were embedded in silicate-dominated materials.

The IVAs also show evidence for a drastic change in cooling environment, but they appear to have formed under conditions that were different (namely hotter) than for the fractionated IIEs. Once again silicate shows evidence for having cooled at a much faster rate than the metal. At moderately high temperatures (~1200 °C), rapid cooling (>100 °C/h) appears to be required to preserve clinobronzite in Steinbach (Haack et al., 1996). São João Nepomeceno contains similar clinobronzite and likely cooled just as fast. Ruzicka and Hutson (2006) noted that rapid cooling could have been initiated from above 1200 °C and even down to ~1000 °C. In any case, at somewhat lower temperatures (~980–1020 °C), cooling rates appear to have slowed to ~1000–2000 °C/Ma in both of the stony irons, as inferred from studies of oxygen isotope closure (Table 8). At still lower temperatures, when the Widmanstätten pattern was forming, the data suggest somewhat different cooling rates for the two stony irons. In Steinbach, overall metallographic cooling rates are ~19 °C/Ma (Rasmussen et al., 1995) or ~150 °C/Ma (Yang et al., 2008). In São João Nepomeceno, these rates are faster, ~890 °C/Ma (Rasmussen et al., 1995). Cation ordering data for orthopyroxene are consistent with a further drop in cooling rate at lower temperatures for São João Nepomeceno (~200–560 °C/Ma) (Table 8).

However, the cation ordering data for Steinbach imply anomalously high cooling rates of 2200–40,300 °C/Ma for three orthopyroxene crystals (Ganguly and Stimpfl, 2000). These rates, although low compared to the rapid cooling inferred for the silicate, are a factor of ~15–2100 higher than for the metallographic rates that have been determined. The reason for this is not known.

Considering only the moderately high temperature silicate and low-temperature metal data for IVA stony irons, cooling rates are a factor of 10^8–10^{10} higher for the silicate, the same as for the silicate-bearing IIEs. Thus, the same conclusions apply: the IVA stony irons were partly exhumed from a temperature slightly above the silicate solidus temperature, and then either deeply buried below impact ejecta, or the parent body was disrupted and reaccreted.

A large spread in metallographic cooling rates has been inferred for the IVA irons and stony irons (Table 8). Models suggest that low-Ni irons cooled an order of magnitude faster than high-Ni irons (Goldstein and Short, 1967; Moren and Goldstein, 1978; Rasmussen, 1982; Rasmussen et al., 1995; Yang et al., 2008). These variations, and the correlation between cooling rate and metal composition, were disputed by Willis and Wasson (1978), Wasson and Richardson (2001), and Wasson et al. (2006). Part of the difficulty was that there did not seem to be good way to establish the Ni – cooling rate correlation (e.g., Willis and Wasson, 1978; Rasmussen, 1982; Wasson, 1985). Crystallizing the metal in a core could explain the compositional variations, but not the differential cooling; crystallizing the metal in distributed pods might allow cooling rate variations but probably would not explain the compositional variations. There is little dispute that Ni contents were established by fractional crystallization of metal in a core, but a deeply buried core would be nearly isothermal and have the same cooling rate for all irons.

An asteroidal break-up event was envisioned for the IVA body, which could take previously crystallized core metal and reassemble it into a secondary body (Rasmussen et al., 1995; Haack et al., 1996; Scott et al., 1996). However, this model suffers from having to place Ni-rich and Ni-poor metal produced in the first body into the correct locations inside the second body to allow the cooling rate – Ni correlation to be established. This model was considered implausible (Wasson et al., 2006).

Ruzicka and Hutson (2006) and Yang et al. (2007, 2008) proposed to create a secondary IVA body in a largely liquid state with no overlying silicate mantle, which can account for cooling rate and petrology constraints. Thus, the core could crystallize from liquid cooling at different rates depending on distance from the surface. The cooling rate – Ni correlation would be established if Ni-poor metal began to crystallize at the top of a liquid body, as one might expect based on the Fe–Ni binary system and having a cold space environment. A similar model of metal cooling in an exposed core was earlier suggested for IIIABs by Yang and Goldstein (2006).

8. Metal–silicate mixing

All silicate-bearing irons contain silicates that appear to have been incorporated into substantially molten metal. Given that silicate will separate from molten metal on a short timescale owing to buoyancy effects (e.g., Bence and Burnett, 1969; Ulff-Møller et al., 1995; Tomkins et al., 2013b), this implies a rapid metal–silicate mixing-cooling process whereby liquefied metal is brought into contact with silicate, which it engulfs, followed by more-or-less rapid cooling to prevent metal–silicate separation. There is widespread agreement that metal–silicate mixing occurred as a result of an impact-induced process (Scott and Wasson, 1976; Nehru et al., 1982; Osadchii et al., 1981; Malvin et al., 1985; Wasson and Wang, 1986; Rubin et al., 1986; Olsen et al., 1994; Casanova et al., 1995; Ikeda and Prinz, 1996; Ruzicka et al., 1999; Bogard et al., 2000; Wasson and Kallemeyn, 2002; Takeda et al., 2003a; Ruzicka and Hutson, 2010; Tomkins et al., 2013a). The evidence is strong that dynamical forces associated with an impact process drove liquefied metal into silicate materials, or vice versa.

Metal–silicate mixing appears to have occurred in different ways in the different iron meteorite groups. In the IIE irons and IVA stony irons, there is good evidence for rapid cooling immediately after metal–silicate mixing, before a return to slow cooling conditions at lower temperatures (Sec. 7). In the IABs, there is little evidence that metal–silicate mixing was followed by rapid cooling, but there is more evidence that it was accompanied by deformation and silicate–silicate mixing. Common in the IABs are breccia textures for silicate clasts, which implies cooler clasts ripped up and embedded in hot metal. Metal–silicate lineation or foliation textures, such as in Campo del Cielo (Fig. 2d) or in Tucson and Bocaiuva, could be the result of flow alignment during metal–silicate mixing (Miyake and Goldstein, 1974; Nehru et al., 1982; Malvin et al., 1985) or a more ductile response to deformation of warm materials. Evidence that impact involved mixing of silicate materials in the IAB parent body is provided by the juxtaposition of different silicate lithologies in adjacent inclusions (Benedix et al., 2000; Ruzicka and Hutson, 2010), discordant closure temperatures in silicates (Benedix et al., 2005), and by variations in Ar–Ar dates for plagioclase in different subsamples of IABs (Vogel and Renne, 2008).

Chronology studies suggest that impact-induced resetting of chronometers occurred in the IAB and IIE parent bodies, although much of the resetting may have occurred in impact events long after metal–silicate mixing (e.g., McCoy, 1995).

9. Igneous lithologies and implications for parent asteroids: case studies

Igneous lithologies of silicates in the silicate-bearing irons provide information on the melting and crystallization processes that affected their asteroidal parent bodies. These processes took place either prior to the impact events that mobilized metal and resulted in metal–silicate mixing, or in response to these events. Igneous petrogenesis models for a well-studied IAB iron (Udei Station), fractionated IIE iron (Miles), and IVA stony iron (Steinbach) are used to infer the thermal and physical state of their parent asteroids during igneous activity (Ruzicka and Hutson, 2006, 2010). These models and their implications are discussed in Appendix-S4.

10. Putting it all together

Most formation models for silicate-bearing irons can be grouped into three classes: (1) exogenic-only models, (2) endogenic-only models, and (3) hybrid models that involve endogenic heating together with a collision. Here these models are discussed in terms of their ability to address fundamental questions regarding silicate-bearing irons, such as: How was metal concentrated? What is the nature of the silicates and how were they formed? What was the thermal history of the rocks and how does this bear on the metal + silicate association?

10.1. Exogenic-only models

Exogenic-only models involve impact mixing and variable degrees of impact heating (partial to complete melting) as the main formation process. This has been suggested for IAB/IIICD irons (Wasson et al., 1980a,b; Rasmussen, 1989; Choi et al., 1995; Wasson and Kallemeyn, 2002), IIE irons (Scott and Wasson, 1976; Burnett and Wasserburg, 1967a; Bence and Burnett, 1969; Osadchii et al., 1981; Wasson and Wang, 1986; Olsen et al., 1994; Ikeda and Prinz, 1996; Ikeda et al., 1997), IVA stony irons (Wasson et al., 2006), the

ungrouped Guin iron (Rubin et al., 1986), the ungrouped NWA 468 iron (Rubin et al., 2002), and the ungrouped Tucson iron (Nehru et al., 1982). For IABs, repeated impact melting episodes are envisioned (Wasson et al., 1980a,b; Choi et al., 1995; Wasson and Kallemeyn, 2002).

For IAB and IIE irons, metallic melt pools are thought to have formed within impact craters at the base of a thick megaregolith on chondritic parent bodies (Wasson et al., 1980a,b; Wasson and Wang, 1986; Choi et al., 1995; Wasson and Kallemeyn, 2002). Presumably, gravity could concentrate metal at the bottom of a chondrite-composition melt pool, but these authors suggest that metal is the main constituent in the overall melt pool, either because it has a lower melting temperature than silicate or because it forms more readily by shock processes. For the IVAs, a very large metal impact melt pool is supposed to have formed at the base of the regolith, which then sank to the center of the asteroid to form a core (Wasson et al., 2006). Concentration of metal into thick veins by shock is supported by observations of ordinary chondrites such as the H-chondrite breccia Portales Valley (e.g., Rubin et al., 2001; Ruzicka et al., 2005; Tomkins et al., 2013a) and the metal-veined H chondrite Kernouvé (Friedrich et al., 2013). Thus, impact melting does provide a potential concentration mechanism for metal.

For the IABs, it is not clear why silicates tend to be chondritic and barely melted when the metal hosts were supposedly repeatedly impact melted (Wasson et al., 1980a,b; Choi et al., 1995; Wasson and Kallemeyn, 2002). To avoid significant melting of silicate, but allow melting of metal, heating would need to occur in a narrow temperature range between the metal-sulfide eutectic and the silicate solidus (e.g., ~920–1080 °C, according to Wasson et al., 1980a,b). But why would impacts deliver just the right amount of heat? If impact-melting is the correct explanation for producing IABs, more examples of at least partly molten and/or glassy silicates would be expected, especially if repeated impacts – and thus many instances of melting – were occurring at the asteroid surface.

For the fractionated IIEs, impact melting is especially problematic for explaining the character of the silicates. It is not clear why fractionated IIE impact melt pools would contain fractionated silicates only, and never chondritic material, when the target asteroids were presumably chondritic in composition. Nor is it obvious that fractionated compositions can be created by impact melting. Rubin et al. (1986) suggested that preferential melting of feldspar during shock could explain the compositions of the silicates in Guin and the fractionated IIEs. They noted that melt pockets of unequivocal shock origin in ordinary chondrites can be feldspar-enriched. However, the melt pockets are significantly less feldspathic on average and only slightly overlap the compositions of inclusions, and the pockets are 3–8 orders of magnitude smaller than the inclusions (Ruzicka et al., 1999). If the inclusions in fractionated IIEs did form by shock melting analogous to melt pockets, one would expect an array of compositions extending from a chondrite composition, but this is not observed (Ruzicka et al., 1999). Instead, the compositions of silicates plot along cotectics and reaction points. Ikeda and Prinz (1996) and Ikeda et al. (1997) suggested that inclusions in Miles formed as shock melts that were generated at the peritectic. However, it seems unlikely that in a rapid shock event, rocks would follow equilibria so closely. It is much more likely that disequilibrium would prevail.

To form silicates in the fractionated IIEs, Osadchii et al. (1981) and Ikeda and Prinz (1996) argued for two shock events, the first resulting in gabbroic silicates and the second resulting in glass and cryptocrystalline silicates. Why two impacts always would be needed to create the silicates in fractionated IIEs is not explained. Also problematic is why the first impact resulted in inclusions with coarse phases, and the second in glass or fine-grained phases. Shock-induced remelting of fractionated IIE silicates to create glass or cryptocrystalline areas was also advocated by Ruzicka et al. (1999) and Bogard et al. (2000), but they argued for two different processes with impact responsible only for the second melting event.

In contrast to the fractionated IIEs, the Watson IIE iron contains silicate that is unfractionated and has an H chrondrite-like composition, although it clearly melted (Olsen et al., 1994). The only significant fractionation observed is a depletion in metal and sulfide, which would have to have been removed from the silicate. Given evidence for metal–silicate separation during shock melting in chondrites (e.g., Tomkins et al., 2013a), it is not a stretch to assume that metal would have been removed from the inclusion and added to the host. The Watson silicate is what one would expect for an impact melting process.

The same cannot be said for the highly fractionated stony iron IVA assemblage, which consists of coarse-grained Si-rich orthopyroxenite that has a cotectic composition. To form this assemblage by impact melting (Wasson et al., 2006) is highly implausible.

For all impact melt models, temperatures are brought up suddenly and then decreased more-or-less rapidly, with cooling occurring close to the surface of an asteroid. Rapid cooling is expected (Choi et al., 1995), unless the impact melts were buried in a warm megaregolith that could have been heated by impacts (Wasson et al., 1980a,b), or that could have been multiple kilometers deep (Wasson and Wang, 1986). Rapid cooling at temperatures above the solidus would be assured if melt pools were small (meter-scale) and entrained many unmelted silicate clasts, as may have occurred in IABs. Rapid cooling has the advantage of preventing metal–silicate separation while metal is molten (Choi et al., 1995; Wasson and Kallemeyn, 2002).

On the other hand, metallographic textures for irons imply that they cooled slowly under subsolidus conditions, and this is a problem for melt pools of any size directly at the surface. This led Wasson et al. (1980a,b) to propose burial of melt pools within a warm megaregolith. A similar concern led Bence and Burnett (1969) to suggest that Kodaikanal (IIE fractionated) was formed by shock melting at depth within the parent body. Haack et al. (1990) showed that cooling rates would be only a few °C/Ma below a 300 m thick regolith layer on a 100 km diameter body. This suggests that provided melt pools are covered with deep regolith, they could cool at the rates inferred by metallographic techniques.

The IABs show evidence that they contain components formed under different thermal conditions. Local variations in geothermometry values, variations in clast types (Benedix et al., 2000), and Ar–Ar closure temperatures all potentially can be explained by cooling in different settings in a multi-km-thick regolith that was being gardened. However, these data indicate big changes that seem more consistent with large-scale turnover in the IAB asteroid than with localized effects within a thick regolith. Nonetheless, the thermal histories of IABs are not in obvious conflict with what one would expect for impact melt pools, provided that the impact melts are buried in deep regolith.

For fractionated IIEs, implied thermal histories are not very consistent with exogenic-only models. They contain components that formed under different cooling conditions, namely coarse grains that formed under slow-cooling conditions, and fine-grained, apparently quench-textured portions and glass (Ruzicka et al., 1999; Takeda et al., 2003a; Ruzicka and Hutson, 2010). Moreover, quenching from above the solidus during glass formation was followed by very slow cooling. This slow-fast-slow cooling pattern is difficult to reconcile with an impact melt origin for the silicates. Fast followed by slow cooling could be explained by ballistic transport of impact melt above an asteroid followed by burial in deep regolith. But slow cooling under igneous conditions followed by fast cooling, is not consistent with impact melting on the surface of an asteroid. The data instead suggest impact-exhumation of partly molten materials that formed within the interior of an asteroid. The

cooling history for fractionated IIEs is precisely the signature that is expected for asteroidal disruption and re-accretion of an internally warmed and partly molten asteroid (Keil et al., 1994).

For the IVA stony irons and irons, impact-only models also fall short in accounting for the thermal histories. The chief problem is that very fast cooling was followed by slow and apparently variable cooling, which is best explained by models of impact disruption and reaccretion of an essentially bare metallic core.

10.2. Endogenic-only models

These models involve interior heating of asteroids together with incomplete separation of metal and sulfide from silicate (partial differentiation) as the main formation process, as suggested for IAB/IIICDs (Wlotzka and Jarosewich, 1977; Kracher, 1983, 1985; McCoy et al., 1993), IIEs (Wasserburg et al., 1968; Prinz et al., 1982; McCoy, 1995), and the IVA stony irons (Ulff-Møller et al., 1995; Scott et al., 1996).

Metal and sulfide are concentrated downwards in a body that is experiencing partial melting of metal and sulfide, so this in principle can explain the metal-rich composition of silicate-bearing irons if they formed deep within the interiors of their asteroids. However, for this mechanism to work requires the right amount of heating, sufficient to enable some metal-sulfide segregation, but not too much heating to allow the process to go to completion. This would require temperatures in excess of the metal-sulfide eutectic at ~940 °C (Fe–Ni–S system, Usselman, 1975), but not so high that most of the silicate was melted. Available data for the IAB body suggest that temperatures exceeded the metal–troilite eutectic and reached as high as ~1150 °C, with only a small amount of silicate melt present, so the measured temperatures are in the correct range. Whether metal-sulfide liquid would sink too fast or too slow is a matter of debate, as it depends on surface tension effects, as well as initial porosity in the asteroid and the amount of gas that is generated during melting (Wilson and Keil, 2012). Given the uncertainties, metal concentration in the IABs as a result of partial differentiation in a weakly melted asteroid is a viable explanation.

This is less true for the fractionated IIEs and especially the IVAs, which would have been heated more strongly and would be expected to have experienced more effective metal–silicate separation. The extent of partial melting was so high in the IVA asteroid that all of the metal and sulfide should have separated to form a core. For the IIEs, it is possible that not all of the metal and sulfide would have separated, but if some did separate, it probably would have been S-rich metallic liquid. IIEs are thought to have relatively low S contents (Wasson and Wang, 1986; Ikeda and Prinz, 1996), which do not resemble the S-rich liquid that could have separated. Even if a S-rich core had not formed in the IIE body, high concentrations of metal in the fractionated IIE silicate source regions would not be expected. To get high concentrations of metal in IIEs would seem to require a mechanism other than gravity, perhaps impact-induced mobilization of metallic liquids as discussed above for IABs, or surface tension effects similar to those discussed by Tomkins et al. (2013b).

The character of the silicate expected to be present in an endogenic-only model for the silicate-bearing irons could vary, depending on the amount of heating and the circumstances of origin. The silicates would be mainly chondritic if they were not significantly melted. This is in fact what is observed in the IAB, supporting an endogenic origin for such irons. However, a pure endogenic origin for IABs does not adequately explain the breccia textures that are often observed, implying deformation, nor the juxtaposition of igneous and chondritic lithologies, implying large-scale metal–silicate mixing. Thus, for IABs an endogenic origin is partly supported but does not seem to be a complete explanation for metal–silicate textures.

For IIEs, which contain chondritic and fractionated silicate varieties, the data are conditionally consistent with an endogenic-only model but reveal some potential difficulties. The unfractionated IIEs could have been derived from a less-melted portion, and the fractionated IIEs from a more-melted portion that had lost olivine. This more-melted portion, if it existed, would probably correspond to an upper mantle zone, distinct from a lower portion of the mantle that would have been rich in olivine and orthopyroxene. This puts the sources of the silicates (upper mantle) and the metal (potentially closer to the core) in the IIE asteroid at different locations. Either the metal did not separate far, or it was mixed with the silicate later. Wasson and Wang (1986) suggested that in the IIEs, metallic melt could have separated from silicate melt only slightly, producing meteoroid-sized accumulations of metal. This might be true, but to account for the olivine-poor nature and geochemistry of the silicate in fractionated IIEs, it would seem that the metallic and silicate melts would have separated from an olivine + orthopyroxene residuum.

The IVA stony irons contain Si-oversaturated silicates, from which olivine was completely removed. This makes the association of such silicates with an apparent, deep-seated metallic core striking, as olivine should predominate at the base of the mantle. The characteristics of IVA silicates suggest a plutonic origin, consistent with an endogenic origin, but one that requires a complicated evolution difficult to achieve in a chondritic body. Thus, an endogenic-only origin for these silicates is problematic.

The thermal histories inferred for silicates are either consistent or inconsistent with an endogenic-only origin, depending on the particular meteorite group and meteorite. In IABs and the unfractionated IIEs Netschaëvo and Techado, silicates appear to have been heated more intensely than in typical chondrites, but can be described as having experienced high-grade metamorphism. Heating was not so intense to significantly melt silicate, and under these conditions it seems unlikely that much metal would have separated. Thus, an endogenic-only origin is consistent with these rocks from the standpoint of thermal histories, character of silicate, and metal concentration.

The inferred thermal histories of the unfractionated IIE Watson, the fractionated IIEs, and the IVAs are inconsistent with an endogenic-only origin. In Watson, silicate was completely melted, implying a temperature high enough to melt all metal too. Under these conditions, metal should have completely separated from silicate, making the occurrence of the large silicate inclusion in this meteorite difficult to understand. An impact melt origin is much more likely for Watson. In the fractionated IIEs, the presence of glass and abundance of metal together are inconsistent with an endogenic-only origin. The glass requires rapid cooling from above the silicate solidus, and could have only formed close to a cooling surface, such as close to the surface of the parent asteroid, or the surface of a fragment from the parent ejected into space. Neither of these processes is likely for an endogenic process such as volcanic eruption, because such an eruption probably would not be able to transport copious dense metal to the surface or into space. Thus, an endogenic-only origin is clearly at odds with the thermal histories of fractionated IIEs and the IVA stony irons.

10.3. Hybrid models

What can be described as hybrid models that involve combinations of endogenic and exogenic processes were formulated for IABs (Benedix et al., 2000; Vogel and Renne, 2008; Ruzicka and Hutson, 2010), IIEs (Bunch et al., 1970; Armstrong et al., 1990; Casanova et al., 1995; Ruzicka et al., 1999; Bogard et al., 2000; Hsu, 2003; Takeda et al., 2003a; Ruzicka and Hutson, 2010); IVAs (Rasmussen et al., 1995; Haack et al., 1996; Scott et al., 1996; Ruzicka and Hutson, 2006), the ungrouped Tucson (Miyake and

Goldstein, 1974), and the ungrouped Sombrerete (Ruzicka et al., 2006). These have variations, but they can be grouped into three categories: (1) "cold crust" models that involve impact-induced mixing of (presumably) cold crustal materials with metallic melt, at the surface of an asteroid; (2) "hot mixing" models that involve impact-induced injection of liquid metal into hot silicate from within an endogenically heated asteroid; (3) "collisional disruption and re-accretion" models that involve the temporary break-up of an internally heated asteroid (e.g., Taylor et al., 1987).

In the "cold crust" models applied to IABs and IIEs, crustal materials of different types (undifferentiated or differentiated) are mixed with molten metal of possible exogenous origin to create metal–silicate breccias. If the crust of the target body was differentiated, fractionated IIEs could result (Bunch et al., 1970; Armstrong et al., 1990; Ruzicka et al., 1999; Hsu, 2003); if the surface was chondritic, IABs and unfractionated IIEs could result (Bunch et al., 1970). For fractionated IIEs, Armstrong et al. (1990), Ruzicka et al. (1999) and Hsu (2003) suggested that silicate glass was created by impact remelting. Ruzicka et al. (1999) specified that the coarser phases pre-dated impact and were created by endogenic processes in the parent body, and that a second target body would be necessary for the unfractionated IIEs.

The "cold crust" models all can explain high metal abundances, if the metal was supplied by an impactor. However, this raises the questions of why there are so many metal impactors – at least three that affected three different target asteroids (IAB, IIE fractionated, IIE unfractionated), and why the metal impactors for the unfractionated and fractionated IIE target bodies have such similar compositions. The characteristics of the silicates are consistent with this model, as more or less differentiated targets could have formed by different degrees of internal heating. The thermal histories that one might expect with such models would be similar to the impact pool models discussed above, as mixing and melting in both occurred at the surfaces of the asteroids. The cold-crust models have two advantages over the exogenic-only models: They explain why silicates in a given meteorite were all either mainly undifferentiated, or mainly differentiated, as the silicates would reflect what was on the target body, and they explain why coarse grains were present in addition to cryptocrystalline or glassy portions in fractionated IIEs, as the coarse grains were formed by a different process (differentiation) in the crust of the target body.

The "hot mixing" models have been applied to the IIEs and the ungrouped Tucson iron. Miyake and Goldstein (1974) suggested that a collision on the Tucson parent body occurred while it was hot (>1000 °C), which forced deep-seated hot metal into a cavity within the silicate host, forming a ring-shaped metal mass along the cavity edge that ultimately became the iron meteoroid. Bogard et al. (2000) suggested an endogenic origin for "old silicate" IIEs, followed by impact-mixing while hot. Takeda et al. (2003a) suggested that for Colomera, impact-disruption of a crystal mush resulted in a combination of coarse crystals and cryptocrystalline and glassy silicates that solidified in a shallow region of the parent body. Casanova et al. (1995) suggested formation of undifferentiated (e.g., Techado) and differentiated (e.g., Colomera) IIEs in the same, "partially melted H-chondrite asteroid". Metallic liquids were mixed with partially melted silicates and ultimately buried in a deep megaregolith, during "collisional mixing and accretion", resulting in a slow-fast-slow cooling history, although an explanation of how the fast cooling would have occurred was not provided.

With the "hot mixing" models it is not clear whether high metal amounts can be explained. It might require impact-induced mobilization, possibly involving cavities that were receptacles for injected metal (Miyake and Goldstein, 1974). The character of the silicates can possibly be explained by having different kinds of differentiated or undifferentiated materials present in the parent body in different locations. The thermal histories one might predict from these models all can explain slow cooling before and after impact, if the materials resided at depth, but might not account for rapid cooling from above the solidus if the source areas stayed deep during the impact disturbance. Glass is present in the fractionated IIE and Tucson irons that imply a rapid cooling stage.

The "collisional disruption and re-accretion" models have been applied to the IVA, IIE, IAB, and Sombrerete parent asteroids. In each, the parent asteroid is considered to be slightly or extensively molten at the time of collisional disruption, followed by reassembly into one or more secondary asteroids. For the IVA disruption, early models called for disaggregation and re-accretion of a nearly solidified differentiated asteroid, with metal core fragments re-accreting (Rasmussen et al., 1995; Haack et al., 1996; Scott et al., 1996). The IVA stony irons were formed during the break-up event at the core–mantle boundary where liquid metal was present (Scott et al., 1996), although the petrogenesis was not explained. Ruzicka and Hutson (2006) envisioned the disruption event as occurring when the asteroid was differentiated but substantially molten. Silicate liquids in the mantle were combined with metallic melts from the core during collisional disruption and accreted into a secondary body that crystallized at various rates depending on depth (Yang et al., 2007, 2008). These models can explain the concentration of metal in the stony irons and irons because they are samples of a core. The character of the silicates was explained by the liquid evolution and crystallization model of Ruzicka and Hutson (2006). The thermal history of the IVA irons and stony irons can be explained, because rapid cooling occurs during the disruption phase and slow cooling after the body is re-accreted.

A similar model was suggested for the Sombrerete ungrouped iron, except that in this case the parent asteroid was much less melted, and a small secondary body was created that cooled rapidly (Ruzicka et al., 2006). This body was composed of silicate and metallic melt produced by partial melting in the original body. The character of the silicates and evidence for rapid cooling were the result of the partial melt origin and the exposure of the liquids to a space environment. Yb and Sm anomalies were produced, possibly indicating generation of gas during the exposure of liquids to a near-vacuum. The high metal content presents some difficulty, because low-density silicate liquids and high-density metallic liquids have to end up in the same secondary body; Ruzicka et al. (2006) suggested this was a result of separation of liquids and solids during the break-up process.

Collisonal disruption and re-accretion of a weakly melted IAB + winonaite asteroid was proposed by Benedix et al. (2000) and Ruzicka and Hutson (2010), and for a somewhat more melted IIE asteroid by Ruzicka and Hutson (2010). Destruction of the IIE body was more complete but the IAB body was left partially intact, losing only its outer chondritic layers. These models are promising.

For the IABs, the high metal contents can be explained if these are samples of an incipient core; otherwise impact mobilization of ductile metal could be invoked. The character of silicates can be explained if the asteroid was only weakly melted and impact disruption fragmented and displaced interior materials. The thermal history can be explained, because the parent asteroid remains mainly intact, but loses upper insulating materials that allow it to cool more rapidly.

For the IIEs, it is not obvious that high metal contents can be explained, but some combination of impact mobilization of metal, or incomplete separation of metal from silicate as discussed for endogenic-only models, may be coming into play. The character of the silicates can be explained, depending on where they originate in the parent asteroid, and so can the thermal histories, because slow cooling in the interior is followed by rapid cooling during the disruption phase, followed by slow cooling after reaccretion and deep burial. As with Sombrerete, disruption of the parent body may have entailed vaporization while hot interior portions of the

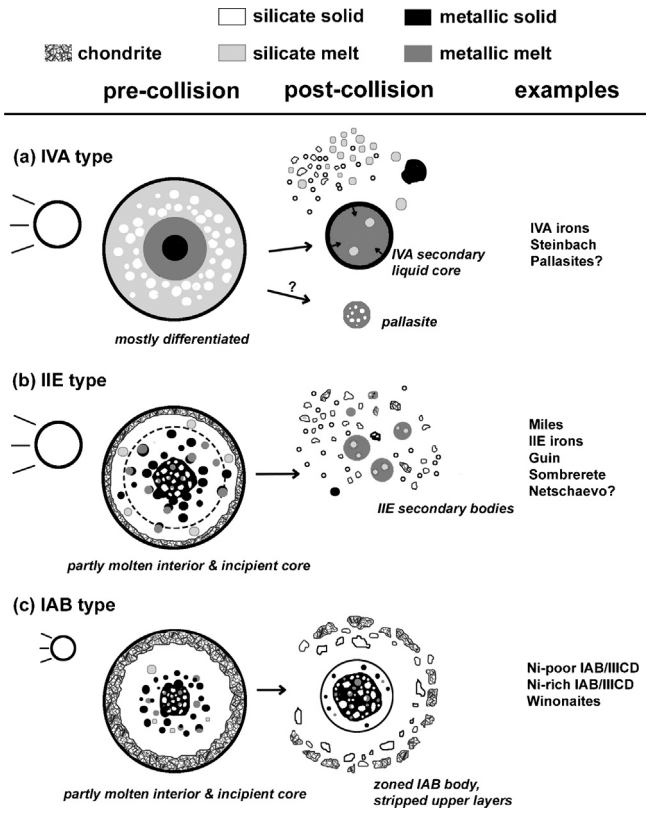

Fig. 16. Cartoon showing the possible evolution of (a) IVA-type asteroids, (b) IIE-type asteroids, and (c) IAB-type asteroids involving collisions affecting completely to partially molten asteroids.

parent body were exposed to the space environment, resulting in Yb anomalies.

10.4. A unified model for the evolution of many melted asteroids

Fig. 16 shows a unified model for the formation of silicate-bearing irons that involves collisional disruption and reassembly of internally heated and strongly melted (IVA-type), moderately melted (IIE-type), and weakly melted (IAB-type) asteroids. Collisional disruption and reassembly can explain not only all the silicate-bearing irons, but also some magmatic irons, pallasites, and mesosiderites.

In collisions of the IVA-type, substantially molten bodies separated into core and mantle portions (Fig. 16a). The mantle was composed of roughly equal portions of olivine and silicate melt, and the core was mostly molten. Removal of the mantle, either by a glancing "hit and run" impact (Asphaug et al., 2006; Asphaug, 2010), or by a more direct collision, would have exposed the core, and allowed it to solidify from the outside in as a largely metallic body. This would have produced the IVA irons. IVA stony irons probably formed by the entrainment of liquid silicate derived from the mantle into the core. Fig. 16a shows a solid inner core to reflect the possibility that the IVA core may have begun to crystallize at the time of impact disruption, which has not been sampled as IVA irons. This is suggested by trace element data that indicate a dearth of low-Ni, high-Ir members in the IVA group such as might form a solid core (Wasson and Richardson, 2001). During impact disruption, hot metallic core materials would have been temporarily exposed to a vacuum, which could have led to vaporization and loss of volatile elements such as P, Ga, Ge, and S as in the IVAs. Pallasites could form in a IVA-type collision by incorporation of olivine from the mantle into partially molten cores. A similar model for Main Group pallasites was proposed by Yang et al. (2010) based on cooling rate data. Finally, IIIAB and IVB irons could have formed in IVA-type collisions that stripped mantles, judging from their variable cooling rates (Scott et al., 2010; Yang et al., 2011).

In collisions of the IIE-type (Fig. 16b), the original asteroid partially differentiated with metallic solid and melt concentrated toward the core, and a mantle that was zoned from an upper mantle richer in feldspathic pyroxenite to a lower mantle richer in harzburgite. A chondritic crust was present in the thermal lid of the body. Collisional disruption, either by a direct or glancing impact, then mixed liquefied metal with the upper mantle and chondritic lid to create fractionated IIE and unfractionated IIE irons, respectively. Ejecta could have sampled different zones of the progenitor body, which re-accreted to form one or more heterogeneous second-generation asteroids. Temporary exposure of hot metallic melts to a space environment could have led to vaporization and loss of volatile elements, although probably not as intensely as for the IVAs if the progenitor asteroid was less hot. Gas–solid reactions could have led to Yb anomalies in the silicates, which were preserved owing to rapid post-collision cooling. Other asteroids experiencing a similar history could have included the parent bodies of the ungrouped irons Guin and Sombrerete. Mesosiderites could have originated from an IIE-type scenario in which the core was largely molten and the mantle was more distinctly differentiated (Scott et al., 2001).

Collisions of the IAB-type (Fig. 16c) involved an original asteroid that experienced less peak heating but which generated small amounts of silicate and metallic melt. The body partly differentiated with a concentration of metal toward the core, a concentration of primitive achondrite materials (winonaite) away from the core, and a thick chondritic surface zone. A collisional event disrupted the interior but left it largely intact, although possibly unroofing the chondrite zone. Shock mobilization during the collision may have helped form a more metal-rich core than would otherwise have been the case. IAB and IIICD irons were derived from this core-like region. The metal-rich core could have been zoned with a Ni-poor center and a Ni-rich exterior, consistent with cooling rate data (Herpfer et al., 1994) and relative I–Xe ages (Niemeyer, 1979a,b). As the collision did not expose core materials as thoroughly or that were as hot as in other collisions, the IAB asteroid could have cooled relatively slowly and retained a greater proportion of volatiles.

Acknowledgments

The author thanks Alan Rubin and Ed Scott for reviews of a very large manuscript on a short time frame, Melinda Hutson for proofreading and work on tables and references, and Marvin Killgore for making samples available for study and photography. I thank Associate Editor Klaus Keil for soliciting and reviewing/handling this Invited Review and for his patience. NASA grant support to the author is gratefully acknowledged (grants NAG5-13044, NAG5-12856, NNG06GE17G, NNX10AH33G, and NNX13AH13G).

Appendix A. Supplementary data

Supplementary material related to this article, including Appendix-S1 (Udei-3B inclusion), Appendix-S2 (Silicates in Miles and Weekeroo Station), Appendix-S3 (Yb and Sm anomalies) and Appendix-S4 (Petrogenesis case studies), can be found, in the online version, at http://dx.doi.org/10.1016/j.chemer.2013.10.001.

References cited in Appendix-S4

Ballhaus and Ellis (1996), Groebner and Kohlstedt (2006), Hustoft and Kohlstedt (2006), McCoy et al. (2011), Morse (1980),

Rushmer et al. (2000, 2005), Rushmer and Petford (2011), Stevenson (1990), Taylor (1992a,b), Yoshino et al. (2004).

References

Anders, E., Grevesse, N., 1989. Abundances of the elements: meteoritic and solar system. Geochim. Cosmochim. Acta 53, 197–214.

Armstrong, J.T., Kennedy, A.K., Carpenter, P.K., Albee, A.L., 1990. Petrography and trace element chemistry of Colomera (IIE) silicate inclusions: rhyolitic plums in the pudding. In: Lunar and Planetary Science XXI, pp. 22–23.

Asphaug, E., 2010. Similar-sized collisions and the diversity of planets. Chem. Erde 70, 199–219.

Asphaug, E., Agnor, C.B., Williams, Q., 2006. Hit-and-run planetary collisions. Nature 439, 155–160.

Ballhaus, C., Ellis, D.J., 1996. Mobility of core melts during Earth's accretion. Earth Plan. Sci. Lett. 143, 137–145.

Bence, A.E., Burnett, D.S., 1969. Chemistry and mineralogy of the silicates and metal of the Kodaikanal meteorite. Geochim. Cosmochim. Acta 33, 387–407.

Benedix, G.K., McCoy, T.J., Keil, K., Bogard, D.D., Garrison, D.H., 1998. A petrologic and isotopic study of winonaites: evidence for early partial melting, brecciation, and metamorphism. Geochim. Cosmochim. Acta 62, 2535–2553.

Benedix, G.K., McCoy, T.J., Keil, K., Love, S.G., 2000. A petrologic study of the IAB iron meteorites: constraints on the formation of the IAB-Winonaite parent body. Meteorit. Planet. Sci. 35, 1127–1141.

Benedix, G.K., Lauretta, D.S., McCoy, T.J., 2005. Thermodynamic constraints on the formation conditions of winonaites and silicate-bearing IAB irons. Geochim. Cosmochim. Acta 69, 5123–5131.

Benkheiri, Y., Pellas, P., Störzer, D., 1979. The cooling histories of Copiapo and Landes (IA) irons. Icarus 40, 497–501.

Benkheiri, Y., 1984. Pu fission track and metallographic cooling rates of Toluca and Copiapo (IA) meteorites. Meteorit. Planet. Sci. 19, 188.

Bild, R.W., 1977. Silicate inclusions in group IAB irons and a relation to the anomalous stones Winona and Mt Morris (Wis). Geochim. Cosmochim. Acta 41, 1439–1456.

Bild, R.W., Wasson, J.T., 1977. Netschaëvo: a new class of chondritic meteorite. Science 197, 58–62.

Birck, J.L., Allègre, C.J., 1998. Rhenium-187–Osmium-187 in iron meteorites and the strange origin of the Kodaikanal meteorite. Meteorit. Planet. Sci. 33, 647–653.

Blichert-Toft, J., Moynier, F., Lee, C.-T.A., Telouk, P., Albarede, F., 2010. The early formation of the IVA iron body. Earth Planet. Sci. Lett. 296, 469–480.

Boesenberg, J.S., Davis, A.M., Prinz, M., Weisberg, M.K., Clayton, R.N., Mayeda, T.K., 2000. The pyroxene pallasites, Vermillion and Yamato 8451: not quite a couple. Meteorit. Planet. Sci. 35, 757–769.

Bogard, D., Burnett, D., Eberhardt, P., Wasserburg, G.J., 1967. ^{40}Ar–40K ages of silicate inclusions in iron meteorites. Earth Planet. Sci. Lett. 3, 275–283.

Bogard, D.D., Burnett, D.S., Wasserburg, G.J., 1969. Cosmogenic rare gases and the ^{40}K–^{40}Ar age of the Kodaikanal iron meteorite. Earth Planet. Sci. Lett. 5, 273–281.

Bogard, D.D., Garrison, D.H., McCoy, T.J., 2000. Chronology and petrology of silicates from IIE iron meteorites: evidence of a complex parent body evolution. Geochim. Cosmochim. Acta 64, 2133–2154.

Bogard, D.D., Garrison, D.H., Takeda, H., 2005. Ar–Ar and I–Xe ages and the thermal history of IAB meteorites. Meteorit. Planet. Sci. 40, 207–224.

Boynton, W.V., 1989. Cosmochemistry of the rare earth elements: condensation and evaporation processes. In: Lipin, B.R., McKay, G.A. (Eds.), Geochemistry and Mineralogy of Rare Earth Elements, vol. 21. Reviews in Mineralogy and Geochemistry, pp. 1–24.

Brearley, A.J., Jones, R.H., 1998. Chondritic meteorites. In: Papike, J.J. (Ed.), Planetary Materials, vol. 36. Reviews in Mineralogy and Geochemistry, pp. 3.1–3.398.

Buchwald, V.F., 1975. Handbook of Iron Meteorites. University of California Press, Los Angeles, CA, pp. 1418.

Bunch, T.E., Keil, K., Olsen, E., 1970. Mineralogy and petrology of silicate inclusions in iron meteorites. Contrib. Mineral. Petrol. 25, 297–340.

Bunch, T.E., Keil, K., Huss, G., 1972. The Landes meteorite. Meteoritics 7, 1–38.

Burnett, D.S., Wasserburg, G.J., 1967a. Evidence for the formation of an iron meteorite at 3.8×10^9 years. Earth Planet. Sci. Lett. 2, 137–147.

Burnett, D.S., Wasserburg, G.J., 1967b. ^{87}Rb–^{87}Sr ages of silicate inclusions in iron meteorites. Earth. Planet. Sci. Lett. 2, 397–408.

Carlson, R.W., Hauri, E.H., 2001. Extending the ^{107}Pd–^{107}Ag chronometer to low Pd/Ag meteorites with multicollector plasma-ionization mass spectrometry. Geochim. Cosmochim. Acta 65, 1839–1848.

Casanova, I., Graf, T., Marti, K., 1995. Discovery of an unmelted H-Chondrite inclusion in an iron meteorite. Science 268, 540–542.

Chabot, N.L., Haack, H., 2006. Evolution of asteroidal cores. In: Lauretta, D.S., McSween Jr., H.Y. (Eds.), Meteorites and the Early Solar System II. University of Arizona Press, Tucson, pp. 747–771.

Chen, J.H., Wasserburg, J.G., 1996. Live ^{107}Pd in the early solar system and implications for planetary evolution. In: Hart, S., Basu, A. (Eds.), Earth Processes: Reading the Isotopic Code, vol. 95. Geophysical Monograph, pp. 1–20.

Chen, J.H., Papanastassiou, D.A., Wasserburg, G.J., 2002. Re–Os and Pd–Ag systematics in Group IIIAB irons and in pallasites. Geochim. Cosmochim. Acta 66, 3793–3810.

Choi, B.-Y., Ouyang, X., Wasson, J.T., 1995. Classification and origin of IAB and IIICD iron meteorites. Geochim. Cosmochim. Acta 59, 593–612.

Chou, C.-L., Cohen, A.J., 1973. Gallium and germanium in the metal and silicates of L and LL chondrites. Geochim. Cosmochim. Acta 37, 315–327.

Chou, C.-L., Baedecker, A.A., Wasson, J.T., 1973. Distribution of Ni, Ga, Ge, and Ir between metal and silicate portions of H group chondrites. Geochim. Cosmochim. Acta 37, 2159–2171.

Clayton, R.N., Mayeda, T.K., 1978. Genetic relations between iron and stony meteorites. Earth Planet. Sci. Lett. 40, 168–174.

Clayton, R.N., Mayeda, T.K., 1996. Oxygen isotope studies of achondrites. Geochim. Cosmochim. Acta 60, 1999–2018.

Clayton, R.N., Mayeda, T.K., Goswami, J.N., Olsen, E.J., 1991. Oxygen isotope studies of ordinary chondrites. Geochim. Cosmochim. Acta 55, 2317–2337.

Clayton, R.N., Mayeda, T.K., Olsen, E.J., Prinz, M., 1983. Oxygen isotope relationships in iron meteorites. Earth Planet. Sci. Lett. 65, 229–232.

Dean, D.C., Goldstein, J.I., 1986. Determination of the interdiffusion coefficients in the Fe–Ni and Fe–Ni–P systems below 900 °C. Metall. Trans. A 17, 1131–1138.

Desnoyers, C., Michel-Levy, M.C., Azevedo, I.S., Scorzelli, R.B., Danon, J., Galvão Silva, E., 1985. Mineralogy of the Bocaiuva iron meteorite: a preliminary study. Meteoritics 20, 113–124.

Ebihara, M., Ikeda, Y., Prinz, M., 1997. Petrology and chemistry of the Miles IIE iron II: chemical characteristics of the Miles silicate inclusions. Antarc. Meteorite Res. 10, 373–388.

Evensen, N.M., Hamilton, P.J., Harlow, G.E., Klimentidis, R., O'Nions, R.K., Prinz, M., 1979. Silicate inclusions in Weekeroo Station: planetary differentiates. In: Lunar and Planetary Science X, pp. 376–378.

Franchi, I.A., 2008. Oxygen isotopes in asteroidal materials. In: MacPherson, G.J., Mittlefehldt, D.W., Jones, J.H., Simon, S.B., Papike, J.J., Mackwell, S. (Eds.), Oxygen in the Solar System, vol. 68. Reviews in Mineralogy and Geochemistry, pp. 345–397.

Friedrich, J.M., Ruzicka, A., Rivers, M.L., Ebel, D.S., Thostenson, J.O., Rudolph, R.A., 2013. Metal veins in the Kernouvé (H6 S1) chondrite: evidence for pre-or syn-metamorphic shear deformation. Geochim. Cosmochim. Acta 116, 71–83.

Frondel, C., Klein, C., 1965. Ureyite, $NaCrSi_2O_6$: a new meteoritic pyroxene. Science 149, 742–744.

Fuchs, L.H., Olsen, E., Henderson, E.P., 1967. On the occurrence of brianiate and panethite, two new phosphate minerals from the Dayton meteorite. Geochim. Cosmochim. Acta 31, 1711–1719.

Fukuoka, T., Schmitt, R.A., 1978. Chemical compositions of silicate inclusions in IAB iron meteorites. In: Lunar and Planetary Science IX, pp. 359–361.

Ganguly, J., Stimpfl, M., 2000. Cation ordering in orthopyroxenes from two stony-iron meteorites: implications for cooling rates and metal–silicate mixing. Geochim. Cosmochim. Acta 64, 1291–1297.

Gilmour, J.D., Pravdivtseva, O.V., Busfield, A., Hohenberg, C.M., 2006. The I–Xe chronometer and the early solar system. Meteorit. Planet. Sci. 41, 19–31.

Goldstein, J.I., Short, J.M., 1967. The iron meteorites, their thermal history and parent bodies. Geochim. Cosmochim. Acta 31, 1733–1770.

Goldstein, J.I., Scott, E.R.D., Chabot, N.L., 2009. Iron meteorites: crystallization, thermal history, parent bodies, and origin. Chem. Erde 69, 293–325.

Göpel, C., Mahnès, G., Allègre, C.J., 1985. Concordant 3676 Myr U–Pb formation age for the Kodaikanal iron meteorite. Nature 317, 341–344.

Gray, C., Papanastassiou, D., Wasserburg, G.J., 1973. The identification of early condensates from the solar nebula. Icarus 20, 213–239.

Greenwood, R.C., Franchi, I.A., Gibson, J.M., Benedix, G.K., 2012. Oxygen isotope variation in primitive achondrites: the influence of primordial, asteroidal, mand terrestrial processes. Geochim. Cosmochim. Acta 94, 146–163.

Groebner, N., Kohlstedt, D.L., 2006. Deformation-induced metal melt networks in silicates: implications for core–mantle interactions in planetary bodies. Earth Plan. Sci. Lett. 245, 571–580.

Haack, H., Rasmussen, K.L., Warren, P.H., 1990. Effects of regolith megaregolith insulation on the cooling histories of differentiated asteroids. J. Geophys. Res. 95, 5111–5124.

Haack, H., McCoy, T.J., 2005. Iron and stony-iron meteorites. In: Davis, a.M. (Ed.), Meteorites, Comets and Planets, vol. 1. In: Holland, H.D., Turekian, K.K. (Eds.), Treatise on Geochemistry, Elsevier, Oxford, pp. 325–345.

Haack, H., Scott, E.R.D., Love, S.G., Brearley, A.J., McCoy, T.J., 1996. Thermal histories of IVA stony-iron and iron meteorites: evidence for asteroid fragmentation and reaccretion. Geochim. Cosmochim. Acta 60, 3103–3113.

Herpfer, M.A., Larimer, J.W., Goldstein, J.I., 1994. A comparison of metallographic cooling rate methods used in meteorites. Geochim. Cosmochim. Acta 58, 1353–1365.

Horan, M.F., Smoliar, M.I., Walker, R.J., 1998. ^{182}W and ^{187}Re–^{187}Os systematics of iron meteorites: chronology for melting, differentiation, and crystallization in asteroids. Geochim. Cosmochim. Acta 62, 545–554.

Horan, M.F., Carlson, R.W., Blichert-Toft, J., 2012. Pd–Ag chronology of volatile depletion, crystallization and shock in the Muonionalusta IVA iron meteorite and implications for its parent body. Earth Plan. Sci. Lett. 351, 215–222.

Hsu, W., 2003. Rare earth element geochemistry and petrogenesis of Miles (IIE) silicate inclusions. Geochim. Cosmochim. Acta 67, 4807–4821.

Hsu, W., Takeda, H., Huss, G.R., Wasserburg, G.J., 1997. Mineralogy and chemical compositions of Colomera (IIE) silicate inclusions. Meteorit. Planet. Sci. 32, A61–A62.

Hustoft, J.W., Kohlstedt, D.L., 2006. Metal–silicate segregation in deforming dunitic rocks. Geochem. Geophys. Geosyst. 7, http://dx.doi.org/10.1029/2005 GC001048.

Ikeda, Y., Prinz, M., 1996. Petrology of silicate inclusions in the Miles IIE iron. Antarct. Meteorite Res. 9, 143–173.

Ikeda, Y., Ebihara, M., Prinz, M., 1997. Petrology and chemistry of the Miles IIE iron, I: description and petrology of twenty new silicate inclusions. Antarct. Meteorite Res. 10, 355–372.

Jarosewich, E., 1990. Chemical analyses of meteorites: a compilation of stony and iron meteorite analyses. Meteoritics 25, 323–337.

Kallemeyn, G., Wasson, J.T., 1985. The compositional classification of chondrites: IV. Ungrouped chondritic meteorites and clasts. Geochim. Cosmochim. Acta 49, 261–270.

Keil, K., Haack, H., Scott, E.R.D., 1994. Catastrophic fragmentation of asteroids: evidence from meteorites. Planet. Space Sci. 42, 1109–1122.

Keil, K., Stöffler, D., Love, S.G., Scott, E.R.D., 1997. Constraints on the role of impact heating and melting in asteroids. Meteorit. Planet. Sci. 32, 349–363.

Kelly, W.R., Larimer, J.W., 1977. Iron meteorites and the cosmochemical history of the metal phase – chemical fractionations in meteorites-VIII. Geochim. Cosmochim. Acta 41, 93–111.

Kleine, T., Mezger, K., Palme, H., Scherer, E., Münker, C., 2005. Early core formation in asteroids and late accretion of chondrite parent bodies: evidence from ^{182}Hf–^{182}W in CAIs, metal-rich chondrites, and iron meteorites. Geochim. Cosmochim. Acta 69, 5805–5818.

Kleine, K., Touboul, M., Bourdon, B., Nimmo, F., Mezger, K., Palme, H., Jacobsen, S.B., Yin, Q.-Z., Halliday, A.N., 2009. Hf–W chronology of the accretion and early evolution of asteroids and terrestrial planets. Geochim. Cosmochim. Acta 73, 5150–5188.

Kong, P., Ebihara, M., 1996. Metal phases of L chondrites: their formation and evolution in the nebula and in the parent body. Geochim. Cosmochim. Acta 60, 2667–2680.

Kong, P., Ebihara, M., Nakahara, H., Endo, K., 1995. Chemical characteristics of metal phases of the Richardton H5 chondrite. Earth Planet. Sci. Lett. 136, 407–419.

Kracher, A., 1974. Untersuchungen am Landes-Meteorit. In: Kiesl, W., Malissa Jr., H. (Eds.), Analyse Extraterrestrischen Materials. Springer, Vienna, pp. 315–326.

Kracher, A., 1982. Crystallization of a S-saturated Fe, Ni-melt, and the origin of the iron meteorite groups IAB and IIICD. Geophys. Res. Lett. 9, 412–415.

Kracher, A., 1983. Formation of IAB and IIICD iron meteorites and the origin of their silicate inclusions. In: Lunar and Planetary Science XXIV, pp. 403–404.

Kracher, A., 1985. The evolution of partially differentiated planetesimals: evidence from iron meteorite groups IAB and IIICD. In: Proceedings of 15th Lunar and Planetary Science Conference JGR 90 Suppl, pp. C689–C698.

Kracher, A., 2000. Metal–silicate relationship in Enon. In: 63rd Annual Meteoritical Society Meeting, (Abstract #5135).

Kracher, A., Kurat, G., 1977. Silicates from the Carleton (IIIC) iron meteorite and possible relations to Group IAB. Meteoritics 12, 282–283.

Kruijer, T.S., Fischer-Gödde, M., Kleine, T., Sprung, P., Leya, I., Wieler, R., 2013. Neutron capture on Pt isotopes in iron meteorites and the Hf–W chronology of core formation in planetesimals. Earth Planet. Sci. Lett. 361, 162–172.

Kurat, G., Zinner, E., Varela, M.E., 2007. Trace element studies of silicate-rich inclusions in the Guin (UNGR) and Kodaikanal (IIE) iron meteorites. Meteorit. Planet. Sci. 42, 1441–1463.

Liu, M., Scott, E.R.D., Keil, K., Wasson, J.T., Clayton, R.N., Mayeda, T., Eugster, O., Crozaz, G., Floss, C., 2001. Northwest Africa 176 a unique iron meteorite with silicate inclusions related to Bocaiuva. In: Lunar and Planetary Science XXII, (Abstract # 2152).

Liu, Y.Z., Nyquist, L.E., Wiesmann, H., Reese, Y., Shih, C.-Y., Takeda, H., 2002. Rb and Sr and Sm–Nd ages of plagioclase-diopside-rich material in Caddo County IAB iron meteorite. In: Lunar and Planetary Science XXXIII, (Abstract #1389).

Liu, Y., Nyquist, L., Wiesmann, H., Shih, H.C., Schwandt, C., Takeda, H., 2003. Internal Rb–Sr age and initial 87Sr/86Sr of a silicate inclusion from the Camp del Cielo iron meteorite. In: Lunar and Planetary Science XXXIV, (Abstract #1983).

Lodders, K., Fegley Jr., B., 1993. Lanthanide and actinide chemistry at high C/O ratios in the solar nebula. Earth Planet. Sci. Lett. 117, 125–145.

Lodders, K., Fegley Jr., B., 1998. The Planetary Scientist's Companion. Oxford University Press, New York, pp. 371.

Luzius-Lange, D., Palme, H., 1987. Trace elements in single mineral grains from silicate inclusions in the Landes Meteorite. In: Lunar and Planetary Science XXVIII, pp. 586–587.

Malvin, D.J., Wasson, J.T., Clayton, R.N., Mayeda, T.K., da Silva Curvelo, W., 1985. Bocaiuva – a silicate-inclusion bearing iron meteorite related to the Eagle Station pallasites. Meteoritics 20, 259–273.

Markowski, A., Quitté, G., Halliday, A.N., Kleine, T., 2006. Tungsten isotopic compositions of iron meteorites: chronological constraints vs. cosmogenic effects. Earth Planet. Sci. Lett. 242, 1–15.

Mason, B., 1967. The Woodbine meteorite, with notes on silicates in iron meteorites. Miner. Mag. 36, 120–126.

Mathew, K.J., Begemann, F., 1995. Isotopic composition of xenon and krypton in silicate-graphite inclusions of the El Taco, Campo del Cielo, IAB iron meteorite. Geochim. Cosmochim. Acta 59, 4729–4746.

MBD, 2013. Meteoritical Bulletin Database, Meteoritical Bulletin 100. http://www.lpi.usra.edu/meteor/metbull.php

McCoy, T.J., 1995. Silicate-bearing IIE irons: early mixing and differentiation in a core–mantle environment and shock resetting of ages. Meteoritics 30, 542–543.

McCoy, T.J., Scott, E.R.D., Haack, H., 1993. Genesis of the IIICD iron meteorites: evidence from silicate-bearing inclusions. Meteoritics 28, 552–560.

McCoy, T.J., Ehlmann, A.J., Benedix, G.K., Keil, K., Wasson, J.T., 1996. The Lueders, Texas, IAB iron meteorite with silicate inclusions. Meteorit. Planet. Sci. 31, 419–422.

McCoy, T.J., Walker, R.J., Goldstein, J.I., Yang, J., McDonough, W.F., Rumble, D., Kotula, P.G., 2011. Group IVA irons: new constraints on the crystallization and cooling history of an asteroidal core with a complex history. Geochim. Cosmochim. Acta 75, 6821–6843.

McDermott, K., Greenwood, R.C., Franchi, I.A., Anand, M., Scott, E.R.D., 2011. Oxygen isotopic and petrological constraints on the origin and relationship of IIE iron meteorites and H chondrites. In: 42nd Lunar and Planetary Science Conference, (Abstract #2673).

McSween Jr., H.Y., Huss, G.R., 2010. Cosmochemistry. Cambridge University Press, Cambridge, pp. 549.

Miyake, G.T., Goldstein, J.I., 1974. The Tucson meteorite. Geochim. Cosmochim. Acta 38, 1201–1212.

Mittlefehldt, D.W., Lindstrom, M.M., 2001. Petrology and geochemistry of Patuxent Range 91501, a clast-poor impact melt from the L-chondrite parent body and Lewis Cliff 88663, an L7 chondrite. Meteorit. Planet. Sci. 36, 439–457.

Mittlefehldt, D.W., McCoy, T.J., Goodrich, C.A., Kracher, A., 1998. Non-chondritic meteorites from asteroidal bodies. In: Papike, J.J. (Ed.), Planetary Materials, vol. 36. Reviews in Mineralogy and Geochemistry, pp. 4.1–4.195.

Moren, A.E., Goldstein, J.I., 1978. Cooling rate variations of Group IVA iron meteorites. Earth Planet. Sci. Lett. 40, 151–161.

Morse, S.A., 1980. Basalts and Phase Diagrams. Springer-Verlag, New York, pp. 493.

Nehru, C.E., Prinz, M., Delaney, J.S., 1982. The Tucson iron and its relationship to enstatite meteorites. In: Proceedings of 13th Lunar and Planetary Science Conference, JGR 87 Suppl, pp. A365–A373.

Niemeyer, S., 1979a. I–Xe dating of silicate and troilite from IAB iron meteorites. Geochim. Cosmochim. Acta 43, 843–860.

Niemeyer, S., 1979b. ^{40}Ar–^{39}Ar dating of inclusions from IAB iron meteorites. Geochim. Cosmochim. Acta 43, 1829–1840.

Niemeyer, S., 1980. I–Xe and ^{40}Ar–^{39}Ar dating of silicate from Weekeroo Station and Netschaëvo IIE iron meteorites. Geochim. Cosmochim. Acta 44, 33–44.

Niemeyer, S., 1983. I–Xe and ^{40}Ar–^{39}Ar analyses of silicate from the Eagle Station pallasite and the anomalous iron meteorite Enon. Geochim. Cosmochim. Acta 47, 1007–1012.

Olsen, E., Jarosewich, E., 1970. The chemical composition of silicate inclusions in the Weekeroo Station iron meteorite. Earth Planet. Sci. Lett. 8, 261–266.

Olsen, E., Jarosewich, E., 1971. Chondrules: first occurrence in an iron meteorite. Science 174, 583–585.

Olsen, E.J., Schwade, J., 1998. The silicate inclusions of the Ocotillo IAB iron meteorite. Meteorit. Planet. Sci. 33, 153–155.

Olsen, E., Davis, A.M., Moore, C.B., Clayton, R.N., Mayeda, T.K., Steele, I.M., 1992. Puente del Zacate: first occurrence of a silicate inclusion in a type III iron (but what is it?). In: Lunar and Planetary Science XXIII, pp. 1019–1020.

Olsen, E., Davis, A., Clarke Jr., R.J., Schultz, L., Weber, H.W., Clayton, R., Takeda, H., Jarosewich, E., Sylvester, P., Grossman, L., Wang, M.-S., Lipschutz, M.E., Steele, I.M., Schwade, J., 1994. Watson: a new link in the IIE iron chain. Meteoritics 29, 200–213.

Olsen, E.J., Clayton, R.N., Mayeda, T.K., Davis, A.M., Clarke Jr., R.J., Wasson, J.T., 1996a. Mbosi: an anomalous iron with unique silicate inclusions. Meteorit. Planet. Sci. 31, 633–639.

Olsen, E.J., Davis, A.M., Clayton, R.N., Mayeda, T.K., Moore, C.B., Steele, I.M., 1996b. A silicate inclusion in Puente del Zacate, a IIIA iron meteorite. Science 273, 1365–1367.

Osadchii, E.G., Novikov, G.V., Baryshnikova, G.V., 1981. The Elga meteorite-Silicate inclusions and shock metamorphism. In: Proceedings of 12th Lunar and Planetary Science Conference, pp. 1049–1068.

Papanastassiou, D.A., Wasserburg, G.J., 1969. Initial strontium isotopic abundances and the resolution of small time differences in the formation of planetary objects. Earth Planet. Sci. Lett. 5, 361–376.

Park, F.R., Bunch, T.E., Massalski, T.B., 1966. A study of the silicate inclusions and other phases in the Campo del Cielo meteorite. Geochim. Cosmochim. Acta 30, 399–414.

Podosek, F.A., 1970. Dating of meteorites by the high-temperature release of iodine correlated Xe^{129}. Geochim. Cosmochim. Acta 34, 341–365.

Powell, B.N., 1969. Petrology and chemistry of mesosiderites. I: Textures and composition of nickel–iron. Geochim. Cosmochim. Acta 33, 789–810.

Prinz, M., Nehru, C.E., Delaney, J.S., 1982. Sombrerete: an iron with highly fractionated amphibole-bearing Na–P silicate inclusions. In: Lunar and Planetary Science XIII, pp. 634–635.

Prinz, M., Nehru, C.E., Delaney, J.S., Weisberg, M., 1983a. Silicates in IAB and IIICD Irons, winonaites, lodranites and brachina: a primitive and modified-primitive group. In: Lunar and Planetary Science XXIV, pp. 616–617.

Prinz, M., Nehru, C.E., Delaney, J.S., Weisberg, M., Olsen, E., 1983b. Globular silicate inclusions in IIE irons and Sombrerete: highly fractionated minimum melts. In: Lunar and Planetary Science XIV, pp. 618–619.

Qin, L., Dauphas, N., Wadhwa, M., Masarik, J., Janney, P.E., 2008. Rapid accretion and differentiation of iron meteorite parent bodies inferred from ^{182}Hf–^{182}W chronometry and thermal modeling. Earth Planet. Sci. Lett. 273, 94–104.

Rambaldi, E., 1976. Trace element content of metals from L-group chondrites. Earth Planet. Sci. Lett. 31, 224–238.

Rambaldi, E.R., 1977. Trace element content of metals from H and LL group chondrites. Earth Planet. Sci. Lett. 36, 347–358.

Ramdohr, P., Prinz, M., El Goresy, A., 1975. Silicate inclusions in the Mundrabilla meteorite. Meteoritics 10, 477.

Rasmussen, K.L., 1982. Determination of the cooling rates and nucleation histories of eight group IVA iron meteorites using local bulk Ni and P variation. Icarus 52, 444–453.

Rasmussen, K.L., 1989. Cooling rates and parent bodies of iron meteorites from group IIICD, IAB, and IVB. Phys. Scriptu 39, 410–416.

Rasmussen, K.L., Ulff-Møller, F., Haack, H., 1995. The thermal evolution of the IVA iron meteorites: evidence from metallographic cooling rates. Geochim. Cosmochim. Acta 59, 3049–3059.
Reid, A.M., Williams, R.J., Takeda, H., 1974. Coexisting bronzite and clinobronzite and the thermal evolution of the Steinbach meteorite. Earth Planet. Sci. Lett. 22, 67–74.
Regelous, M., Elliott, T., Coath, C.D., 2008. Nickel isotope heterogeneity in the early Solar System. Earth Planet. Sci. Lett. 272, 330–338.
Rubin, A.E., 1990. Kamacite and olivine in ordinary chondrites: intergroup and intragroup relationships. Geochim. Cosmochim. Acta 54, 1217–1232.
Rubin, A.E., Jerde, E.A., Zong, P., Wasson, J.T., Westcott, J.W., Mayeda, T.K., Clayton, R.N., 1986. Properties of the Guin ungrouped iron meteorite: the origin of Guin and of group-IIE irons. Earth Planet. Sci. Lett. 76, 209–226.
Rubin, A.E., Ulff-Møller, F., Wasson, J.T., Carlson, W.D., 2001. The Portales Valley meteorite breccia: evidence for impact-induced melting and metamorphism of an ordinary chondrite. Geochim. Cosmochim. Acta 65, 323–342.
Rubin, A.E., Kallemeyn, G.W., Wasson, J.T., 2002. A IAB-complex iron meteorite containing low-Ca clinopyroxene: Northwest Africa 468 and its relationship to lodranites and formation by impact melting. Geochim. Cosmochim. Acta 66, 3657–3671.
Rushmer, T., Minarik, W.G., Taylor, G.J., 2000. Physical processes of core formation. In: Canup, R.M., Righter, K. (Eds.), Origin of the Earth and Moon. University of Arizona Press, Tucson, pp. 227–243.
Rushmer, T., Petford, N., Humayun, M., Campbell, A.J., 2005. Fe-liquid segregation in deforming planetesimals: coupling core-forming compositions with transport phenomena. Earth Plan. Sci. Lett. 239, 185–202.
Rushmer, T., Petford, N., 2011. Microsegregation rates of liquid Fe–Ni–S metal in natural silicate–metal systems: a combined experimental and numerical study. Geochem. Geophys. Geosyst. 12, http://dx.doi.org/10.1029/2010GC003413.
Ruzicka, A., Hutson, M., 2006. Differentiation and evolution of the IVA meteorite parent body: clues from pyroxene geochemistry in the Steinbach stony-iron meteorite. Meteorit. Planet. Sci. 41, 1959–1987.
Ruzicka, A., Hutson, M., 2010. Comparative petrology of silicates in the Udei Station (IAB) and Miles (IIE) iron meteorites: implications for the origin of silicate-bearing irons. Geochim. Cosmochim. Acta 74, 394–433.
Ruzicka, A., Fowler, G.W., Snyder, G.A., Prinz, M., Papike, J.J., Taylor, L.A., 1999. Petrogenesis of silicate inclusions in the Weekeroo Station IIE iron meteorite: differentiation, remelting, and dynamic mixing. Geochim. Cosmochim. Acta 63, 2123–2143.
Ruzicka, A., Killgore, M., Mittlefehldt, D.W., Fries, M.D., 2005. Portales Valley: petrology of a metallic-melt meteorite breccia. Meteorit. Planet. Sci. 40, 261–296.
Ruzicka, A., Hutson, M., Floss, C., 2006. Petrology of silicate inclusions in the Sombrerete ungrouped iron meteorite: implications for the origins of IIE-type silicate-bearing irons. Meteorit. Planet. Sci. 41, 1797–1831.
Ruzicka, A., Grossman, J.N., Garvie, L., 2014. The Meteoritical Bulletin, No. 100, 2013 November. Meteorit. Planet. Sci. (in press).
Saikumar, V., Goldstein, J.I., 1988. An evaluation of the methods to determine the cooling rates of iron meteorites. Geochim. Cosmochim. Acta 52, 715–726.
Sanz, H.G., Burnett, D.S., Wasserburg, G.J., 1970. A precise 87 Rb/87 Sr age and initial 87 Sr/86 Sr for the Colomera iron meteorite. Geochim. Cosmochim. Acta 34, 1227–1228.
Scherstén, A., Elliott, T., Hawkesworth, C., Russell, S., Masarik, J., 2006. Hf–W evidence for rapid differentiation of iron meteorite parent bodies. Earth Planet. Sci. Lett. 241, 530–542.
Schulz, T., Münker, C., Palme, H., Mezger, K., 2009. Hf–W chronometry of the IAB iron meteorite parent body. Earth Planet. Sci. Lett. 280, 185–193.
Schulz, T., Münker, C., Mezger, K., Palme, H., 2010. Hf–W chronometry of primitive achondrites. Geochim. Cosmochim. Acta 74, 1706–1718.
Schulz, T., Upadhyay, D., Münker, C., Mezger, K., 2012. Formation and exposure history of non-magmatic iron meteorites and winonaites: clues from Sm and W isotopes. Geochim. Cosmochim. Acta 85, 200–212.
Scott, E.R.D., 1982. Origin of rapidly solidified metal–troilite grains in chondrites and iron meteorites. Geochim. Cosmochim. Acta 46, 813–823.
Scott, E.R.D., Bild, R.W., 1974. Structure and formation of the San Cristobal meteorite, other IB irons and group IIICD. Geochim. Cosmochim. Acta 38, 1379–1391.
Scott, E.R.D., Wasson, J.T., 1975. Classification and properties of iron meteorites. Rev. Geophys. Space Phys. 13, 527–546.
Scott, E.R.D., Wasson, J.T., 1976. Chemical classification of iron meteorites – VIII. Groups IC, IIE, IIIF and 97 other irons. Geochim. Cosmochim. Acta 40, 103–115.
Scott, E.R.D., Haack, H., McCoy, T.J., 1996. Core crystallization and silicate–metal mixing in the parent body of the IVA iron and stony-iron meteorites. Geochim. Cosmochim. Acta 60, 1615–1631.
Scott, E.R.D., Haack, H., Love, S.G., 2001. Formation of mesosiderites by fragmentation and reaccretion of a large differentiated asteroid. Meteorit. Planet. Sci. 36, 869–881.
Scott, E.R.D., Goldstein, J.I., Yang, J., Asphaug, E., Bottke, W.F., 2010. Iron and stony-iron meteorites and the missing mantle meteorites and asteroids. Meteorit. Planet. Sci. Suppl. 73, 5015.
Seckendorff, V.V., O'Neill, H., St, C., Zipfel, J., Palme, H., 1992. Evidence for a late reducing event in IAB-silicate inclusions. Meteoritics 27, 288.
Shen, J.J., Papanastassiou, D.A., Wasserburg, G.J., 1996. Precise Re–Os determinations and systematics of iron meteorites. Geochim. Cosmochim. Acta 60, 2887–2900.
Shirey, S.B., Walker, R.J., 1998. The Re–Os isotope system in cosmochemistry and high-temperature geochemistry. Annu. Rev. Earth Planet. Sci. 26, 423–500.
Smoliar, M.I., Walker, R.J., Morgan, J.W., 1996. Re–Os ages of group IIA, IIIA, IVA, and IVB iron meteorites. Science 271, 1099–1102.
Snyder, G.A., Lee, D.-C., Ruzicka, A.M., Prinz, M., Taylor, L.A., Halliday, A.N., 2001. Hf–W, Sm–Nd, and Rb–Sr isotopic evidence of late impact fractionation and mixing of silicates on iron meteorite parent bodies. Earth Planet. Sci. Lett. 186, 311–324.
Stevenson, D.J., 1990. Fluid dynamics of core formation. Origin Earth 1, 231–249.
Stewart, B., Papanastassiou, D.A., Wasserburg, G.J., 1996. Sm–Nd systematics of a silicate inclusion in the Caddo iron meteorite. Earth Plan. Sci. Lett. 143, 1–12.
Takeda, H., Bogard, D.D., Mittlefehldt, D.W., Garrison, D.H., 2000. Mineralogy, petrology, chemistry, and ^{39}Ar–^{40}Ar and exposure ages of the Caddo County IAB iron: evidence for early partial melt segregation of a gabbro area rich in plagioclase-diopside. Geochim. Cosmochim. Acta 64 (131), 1–1327.
Takeda, H., Hsu, W., Huss, G.R., 2003a. Mineralogy of silicate inclusions of the Colomera IIE iron and crystallization of Cr-diopside and alkali feldspar from a partial melt. Geochim. Cosmochim. Acta 67, 2269–2287.
Takeda, H., Bogard, D.D., Otsuki, M., Ishii, T., 2003b. Mineralogy and Ar–Ar age of the Tarahumara IIE iron, with reference to the origin of alkali-rich materials. In: NIPR Annual Meeting, Tokyo, September 2003.
Taylor, G.J., 1992a. Differentiation without core formation: S-asteroids and stony iron meteorites. In: Lunar and Planetary Science XXII, pp. 1385–1386.
Taylor, G.J., 1992b. Core formation in asteroids. J. Geophys. Res. 97, 14717–14726.
Taylor, G.J., Maggiore, P., Scott, E.R., Rubin, A.E., Keil, K., 1987. Original structures, and fragmentation and reassembly histories of asteroids: evidence from meteorites. Icarus 69, 1–13.
Teshima, J., Larimer, J.W., 1983. The IVB iron meteorite parent body: inferences based on inclusion mineralogy and composition. Meteoritics 18, 406–407.
Tomkins, A.G., Weinberg, R.F., Schaefer, B.F., Langendam, A., 2013a. Disequilibrium melting and melt migration driven by impacts: implications for rapid planetesimal core formation. Geochim. Cosmochim. Acta 100, 41–59.
Tomkins, A.G., Mare, E.R., Raveggi, M., 2013b. Fe-carbide and Fe-sulfide liquid immiscibility in IAB meteorite, Campo del Cielo: implications for iron meteorite chemistry and planetesimal core compositions. Geochim. Cosmochim. Acta 117, 80–98.
Trinquier, A., Birck, J.L., Allègre, C.J., 2007. Widespread ^{54}Cr heterogeneity in the inner solar system. Astrophys. J. 655, 1179–1185.
Ulff-Møller, F., Rasmussen, K.L., Prinz, M., Palme, H., Spettel, B., Kallemeyn, G.W., 1995. Magmatic activity on the IVA parent body: evidence from silicate-bearing iron meteorites. Geochim. Cosmochim. Acta 59, 4713–4728.
Usselman, T.M., 1975. Experimental approach to the state of the core. Part I: The liquidus relations of the Fe–Ni–S system from 30 to 100 kb. Am. J. Sci. 275, 278–290.
Vogel, N., Renne, P.R., 2008. ^{40}Ar–^{39}Ar dating of plagioclase grain size separates from silicate inclusions in IAB iron meteorites and implications for the thermochronological evolution of the IAB parent body. Geochim. Cosmochim. Acta 72, 1231–1255.
Wadhwa, M., Srinivasan, G., Carlson, R.W., 2006. Timescales of planetesimal differentiation in the early solar system. In: Lauretta, D.S., McSween Jr., H.Y. (Eds.), Meteorites and the Early Solar System II. University of Arizona Press, Tucson, pp. 715–731.
Wang, P.-L., Rumble, D., McCoy, T.J., 2004. Oxygen isotopic compositions of IVA iron meteorites: implications for the thermal evolution derived from in situ ultraviolet laser microprobe analyses. Geochim. Cosmochim. Acta 68, 1159–1171.
Warren, P.H., 2011. Stable-isotopic anomalies and the accretionary assemblage of the Earth and Mars: a subordinate role for carbonaceous chondrites. Earth Planet. Science Lett. 311, 93–100.
Wasserburg, G.J., Sanz, H.G., Bence, A.E., 1968. Potassium-feldspar phenocrysts in the surface of Colomera, an iron meteorite. Science 161, 684–687.
Wasson, J.T., 1985. Meteorites – Their Record of Early Solar System History. W.H. Freeman and Co, New York, pp. 267.
Wasson, J.T., Wang, J., 1986. A non-magmatic origin of group-IIE iron meteorites. Geochim. Cosmochim. Acta 50, 725–732.
Wasson, J.T., Kallemeyn, G.W., 2002. The IAB iron-meteorite complex: a group, five subgroups, numerous grouplets, closely related, mainly formed by crystal segregation in rapidly cooling melts. Geochim. Cosmochim. Acta 66, 2445–2473.
Wasson, J.T., Richardson, J.W., 2001. Fractionation trends among IVA iron meteorites: contrasts with IIIAB trends. Geochim. Cosmochim. Acta 65, 951–970.
Wasson, J.T., Willis, J., Wai, C.M., Kracher, A., 1980a. Origin of iron meteorite groups IAB and IIICD. In: Lunar and Planetary Science XI, pp. 25–26.
Wasson, J.T., Willis, J., Wai, C.M., Kracher, A., 1980b. Origin of iron meteorite groups IAB and IIICD. Z. Naturforsch. 35a, 781–795.
Wasson, J.T., Matsunami, Y., Rubin, A.E., 2006. Silica and pyroxene in IVA irons; possible formation of the IVA magma by impact melting and reduction of L-LL-chondrite materials followed by crystallization and cooling. Geochim. Cosmochim. Acta 70, 3149–3172.
Weisberg, M., Smith, C., Benedix, G., Herd, C.D.K., Righter, K., Haack, H., Yamaguchi, A., Chennaoui Aoudjehane, H., Grossman, J.N., 2009. The Meteoritical Bulletin, No. 96, September 2009. Meteorit. Planet. Sci. 44, 1355–1397.
Willis, J., Wasson, J.T., 1978. Cooling rates of Group IVA iron meteorites. Earth Planet. Sci. Lett. 40, 141–150.
Wilson, L., Keil, K., 2012. Volcanic activity on differentiated asteroids: a review and analysis. Chem. Erde 72, 289–321.
Wlotzka, F., Jarosewich, E., 1977. Mineralogical and chemical compositions of silicate inclusions in the El Taco, Camp del Cielo, iron meteorite. Smithsonian Contrib. Earth Sci. 19, 104–125.
Yang, J., Goldstein, J.I., 2006. Metallographic cooling rates of the IIIAB iron meteorites. Geochim. Cosmochim. Acta 70, 3197–3215.

Yang, J., Goldstein, J.I., Scott, E.R., 2007. Iron meteorite evidence for early formation and catastrophic disruption of protoplanets. Nature 446, 888–891.
Yang, J., Goldstein, J.I., Scott, E.R.D., 2008. Metallographic cooling rates and origin of IVA iron meteorites. Geochim. Cosmochim. Acta 72, 3043–3061.
Yang, J., Goldstein, J.I., Scott, E.R.D., 2010. Main-group pallasites: thermal history, relationship to IIIAB irons, and origin. Geochim. Cosmochim. Acta 74, 4471–4492.
Yang, J., Goldstein, J.I., Scott, E.R.D., Michael, J.R., Kotula, P.G., Pham, T., McCoy, T.J., 2011. Thermal and impact histories of reheated group IVA, IVB, and ungrouped iron meteorites and their parent asteroids. Meteorit. Planet. Sci. 46, 1227–1252.
Yoshino, T., Walter, M.J., Katsura, T., 2004. Connectivity of molten Fe alloy in peridotite based on in situ electrical conductivity measurements: implications for core formation in terrestrial planets. Earth Planet. Sci. Lett. 222, 625–643.